Mechanisms of Extreme Dynamics in Femtosecond Laser Interaction With Materials; Ultrafast Mass Transport, Desorption, Formation of Periodic Structures, and Oxidation

by

Alex Sarracino

A dissertation submitted in partial fulfillment
of the requirements for the degree of
Doctor of Philosophy
(Applied Physics)
in The University of Michigan
2021

Doctoral Committee:

Professor Steven M. Yalisove, Chair
Research Scientist Ben Torralva, Co-Chair
Professor Roy Clarke
Assistant Professor John Heron
Professor Herbert Winful

Alex Sarracino

alexsar@umich.edu

ORCID iD: 0000-0002-7407-3304

Para mis padres, Pedro y Dora, quien siempre creyeron en mi hasta cuando yo no pude.

ACKNOWLEDGEMENTS

I would like to thank Rico Cahyadi and Keegan Schrider, who helped me get my bearings as a new graduate student. Without their instruction I would not have been able to be where I am. To my advisor Steven Yalisove, who taught me what it means to be a scientist, and who had the patience to help me turn into one. To Ben Torralva, who taught me more about physics than anyone else. Some of my best ideas were conceived thanks to one of our numerous (and lengthy!) discussions. I specifically would like to thank my colleague, and more importantly friend, Abdul Ansari. He was always there for me when I needed him the most (unless he was working out). I would also like to thank Luis Garbinski and Dylan Smith, whose friendship helped me stay sane throughout my graduate career. I would like to thank my partner Anna Pohlod, without her support I would not have made it this far. Last but not least, I would like to thank my family back home, who supported my dream to not have to get a real job until my late 20s.

TABLE OF CONTENTS

DEDICATION ii

ACKNOWLEDGEMENTS iii

LIST OF FIGURES vii

LIST OF TABLES ix

LIST OF APPENDICES x

ABSTRACT xi

CHAPTER

I. Introduction 1

II. Background 5

2.1 Timescale of Interactions 5
2.2 Ultrafast Mechanisms 8
2.3 Laser Induced Periodic Surface Structures 11
2.3.1 LSFL 11
2.3.2 HSFL 12
2.4 Surface Plasmon Polaritons 14
2.4.1 Surface Plasmon Polaritons at a Single Interface . . 14
2.4.2 Surface Plasmon Polariton Propagating in Multiple Interfaces 18
2.5 Desorption 21
2.6 Semiconductor Oxidation 23
2.6.1 Thermal Oxidation of Silicon 23
2.6.2 Light Enhanced Oxidation of Silicon and GaAs . . . 25
2.7 Diffusion in Semiconductors 27
2.7.1 Fick's laws and Brownian Motion 27
2.7.2 Diffusion Processes 29

2.7.3 Photostimulated Diffusion 30

III. Experimental Procedures 34

3.1 Laser 34
3.2 Sample Preparation 35
3.3 Optical Alignment 35
3.4 Measuring and Aligning Laser 36
3.5 Second Harmonic Generation 37
3.6 Alignment of Pump Probe Experiments 39

IV. Desorption as a Mechanism for the Formation of Periodic Structures 42

4.1 Formation of HSFL with 390 nm Light 43
4.1.1 Determining the Dielectric Function During Excitation 51
4.1.2 Existing HSFL Period Models 53
4.2 Desorption with 780 nm Light 55

V. Excited State Enhanced Diffusion 61

5.1 Growth Rate of HSFL Formation with 780 nm Light 61
5.2 Laser Enhanced Mass Transport 68
5.2.1 Ultrafast Point Defect Formation 68
5.2.2 Excited State Mediated Diffusion 70
5.3 Removal Rate of GaAs in Vacuum 75

VI. Anomalous Oxidation of Silicon 83

6.1 Enhanced Oxide Growth in Si 83
6.2 Diffusion Rate Calculations 91
6.3 Possible Enhancements to the Diffusion Coefficient 93

VII. Summary 99

VIII. Future Work 104

8.1 Silicon and Beyond 104
8.2 Directly Measuring Transport Rates 107
8.2.1 Electron Scattering 109
8.2.2 X-Ray Scattering 111
8.2.3 Extreme Ultraviolet Laser 112
8.3 Better Understanding of Material Response 112
8.3.1 Wavelength and Activation Energy 112

8.3.2 Dielectric Function Measurements 113

APPENDICES 115
A.1 Establishing the role of desorption on the formation of periodic structures 116
A.2 Demonstrating that an enhanced mass transport mechanism occurs upon irradiation with ultrafast laser pulses in GaAs . . 118
A.3 Presenting a model for the growth of anomalous SiO_2 119
A.4 Demonstrating that an excited state mediated diffusion mechanism is an universal mechanism that occurs upon ultrafast irradiation of semiconductors 120
B.1 Seed Laser 121
B.2 CPA Regen Alignment 123
B.3 Flash Lamp Replacement 123
C.1 Preparing the Vacuum Chamber 127
C.2 Microchannel Plate Setup and Operation 128
C.3 Third Harmonic Crystal Alignment 129
C.4 Photocathode Preparation 129

BIBLIOGRAPHY 151

LIST OF FIGURES

Figure

2.1	Timescales of Laser Interactions	6
2.2	Schematic of bandgap collapse	9
2.3	Schematic of Grating Coupled Surface Plasmon Excitation	17
2.4	Schematic for Two Interface SPP Model	18
2.5	Configuration-coordinate diagrams of recombination reactions	32
3.1	Optical Setup Schematic	35
3.2	Optical Setup Schematic with Second Harmonic Generation	38
3.3	Pump Probe Optical Schematic	39
4.1	Comparison between HSFL formation in air and in vacuum	45
4.2	Cross Section SEM of HSFL Formed with 390 nm light	46
4.3	Evolution of HSFL formation with 390 nm light	48
4.4	AFM of crater formed after 500 irradiations with 390 nm light	49
4.5	Schematic Of Desorption Process	49
4.6	TEM and NBED of 65 nm HSFL	50
4.7	Calculated dielectric function of GaAs during excitation	53
4.8	HSFL Formation after 1000 irradiations with 780 nm light in vacuum	56
4.9	HSFL Formation after 2000 irradiations with 780 nm light in vacuum	57
4.10	HSFL Formation after 10,000 irradiations with 780 nm light in vacuum	58
5.1	Reflectivity of HSFL formation with 780 nm light	64
5.2	Cross Section TEM of GaAs Irradiated with 780 nm light in air	65
5.3	Diffusion Coefficients for Ga diffusion in GaAs	69
5.4	Schematic of Point Defect Formation Mechanism	70
5.5	Schematics of Enhanced Diffusion Mechanisms	72
5.6	Timescale of Excitation Regimes Upon Ultrafast Irradiation	74
5.7	AFM of HSFL formation upon 1000 irradiations with 390 nm light in vacuum	76
5.8	Desorption rate as a function of fluence for irradiation with 390 nm light	76
5.9	Desorption rate as a function of fluence for irradiation with 390 nm and 780 nm light	77
5.10	Schematic of Solid-on-Solid algorithm	79
5.11	Simulation for Point Defect Enhanced Desorption	82

6.1 Overview of SiO_2 growth upon irradiation with 390 nm light 84
6.2 SEM of silicon oxide after 500 exposures with 390 nm light 86
6.3 Cross section of silicon oxide upon 100,000 irradiations with 390 nm light 87
6.4 Schematic of the oxide growth mechanism 89
6.5 Cross section of silicon oxide upon 1,000,000 irradiations with 390 nm light 90
6.6 Growth rate of silicon oxide as a function of fluence 96
8.1 Schematic of proposed process for selective doping of silicon 108
8.2 Oxide growth in GaAs 109
8.3 Schematic of Electron Gun 111
B.1 Perfect Mode-Locking Signal 122
B.2 Regen Troubleshooting Picture 124
B.3 Regen Pulse Train 126

LIST OF TABLES

Table

5.1 Diffusion Coefficients for Ga diffusion in GaAs 68
6.1 Summary of oxide growth rates and thickness 92

LIST OF APPENDICES

Appendix

A. Goals 116

B. Laser Troubleshooting 121

C. Electron Gun Setup 127

D. Excited State Dielectric Function Code 131

E. Thin Film Plasmonic Model Code 140

F. Solid on Solid Model Code 145

ABSTRACT

This thesis focused the understanding of the mechanisms responsible for different morphologies that emerge upon ultrafast irradiation. These morphological changes include the formation laser-induced periodic surface structures (LIPSS) on gallium arsenide (GaAs) in both air and vacuum as well as laser-induced oxidation of silicon (Si). Experiments were performed by varying irradiation conditions such as wavelength, pressure, and fluence to form the structures. The structures were then characterized by using a combination of optical, scanning electron (SEM), tunneling electron, and atomic force microscopies.

The first section developed an understanding of the formation of High Spatial Frequency LIPSS (HSFL) at different wavelengths and pressures. It demonstrated that, when the substrate was irradiated with 390 nm light and 780 nm light while in a vacuum environment, the formation of HSFL was caused by material removal and not material reorganization which occurs in ambient atmospheric environments. The mechanism that drove this process was suggested to be the formation and subsequent diffusion of point defects to the substrate surface where they were more easily desorbed. The excited state dielectric function was modeled and was used in a thin film plasmonic SPP model to predict the HSFL wavelength that was experimentally observed after irradiation with 390 nm light in vacuum.

The second section reanalyzed the point defect formation mechanism that has been shown to generate HSFL. Specifically, it roughly quantified the diffusion rates of point defects that eventually form the surface structures. The diffusion coefficient for interstitials upon ultrafast irradiation with 780 nm light was estimated to be

6.5×10^{-8} cm^2/s and compared with experimentally measured diffusion coefficients in the literature. The estimated coefficient was 20 orders of magnitude higher than expected for purely thermal diffusion. A model for an excited state diffusion was then presented which used the point defect formation mechanism as a basis. Lastly, using a discrete Monte Carlo model, it was shown that the excited state mediated diffusion also occurred in the formation of HSFL in GaAs in vacuum with both 390 nm and 780 nm light.

The third section discussed the ultrafast oxidation of silicon. It was shown that the rates for the oxide growth upon ultrafast irradiation was 10 orders of magnitude higher than that for thermal oxidation. Furthermore, cross section SEM showed that the oxide growth occurs at both the oxide-Si interface as well as the oxide-air interface. The silicon atom flux rate from the bulk into the oxide was then calculated to be 1.3×10^8 $\frac{at}{nm^2 \cdot s}$, which is on the same order of magnitude for the excited state mediated diffusion mechanism, suggesting that this mechanism occurs in Si as well as GaAs.

Altogether, this thesis reveals that excited state diffusion is a driving factor behind many of the mechanisms observed at sub-melt fluence threshold irradiation with ultrafast laser. Furthermore, it suggests that this is a universal mechanism of ultrafast excitation of semiconductors due to its presence in both the formation of HSFL in GaAs and the oxidation of Si.

CHAPTER I

Introduction

The advent of ultrafast lasers has allowed the study of materials driven to extreme conditions far from equilibrium. By compressing light pulses to widths of 100s femtoseconds, intensities on the order of 10^{13} W/cm^2 can routinely be achieved, even when the total energy delivered by the laser is below where thermal effects have a significant role. Sub picosecond (ps) pulse duration also mean that the light is fully absorbed before the excited electrons can thermalize, leading to the formation of a non-thermal dense electron hole plasma [1, 2]. Even after the thermalization of electrons, the material response to the irradiation remains non-steady state [3, 4].

In this regime of irradiation, a plethora of effects have been observed that are unique to ultrafast irradiation. The excitation of a high density of electrons forms a dense electron-hole plasma that can significantly weaken the interatomic potential [1]. This weakening of the interatomic potential causes a large amount of disorder in the lattice, which leads to a closure of the bandgap, or a complete collapse at high enough intensity [3]. This disorder has also been shown to increase the density of point defects in the material, since the rapid relaxation of the electrons can lead to recombination when the atom is in an interstitial site. At higher fluences, where irradiation causes rapid melting and solidification, ablation can result in the removal of atoms.

This thesis will be focusing on the regime in which a single irradiation does not lead to a permanent morphological change in the irradiated material. In this regime, multiple excitations have been shown to largely increase the density of point defects without melting the material [5], form nano islands on the surface [6], and form periodic structures [5, 7, 8]. These periodic structures are generally referred to as "Laser Induced periodic Surface Structures" (LIPSS). LIPSS can generally be further categorized into LSFL, which is characterized by having a period greater than half the wavelength of light, and HSFL, which is characterized by having a period less than half the wavelength of light. While the mechanisms for the formation of LSFL have been mostly understood and detailed, the mechanisms for formation of HSFL is still under active investigation [9]. One aspect of the formation of HSFL that has largely remained unexplored is the role that the incident wavelength has on the formation of HSFL. Naively, one would think that after thermalization of the excited electrons, there would be no difference in the material response. This thesis will show that the wavelength used for irradiation has a noticeable effect on the formation of the HSFL. Furthermore, this thesis will also show that the excitation environment plays an important role for the development of the HSFL. Specifically, it will be shown that a material removal mechanism can be activated at low pressures, which lead to HSFL with different properties than when formed in air.

This thesis will also re-examine the HSFL formation mechanism in GaAs in air[5] in the context of calculating the diffusion rates observed during irradiation. It will be shown that the diffusion rates observed during the formation of HSFL with 780 nm light in air are orders of magnitude higher than observed in thermal diffusion. It is proposed that this enhanced diffusion occurs while the interatomic potential is weakened, as the barrier for an atom to hop to another site is decreased during this time. Other possible sources of this enhancement will also be proposed, including recombination stimulated diffusion [10] and sub ps diffusion due to a non-fermi dis-

tribution of electrons [11]. It will also be shown that this diffusion mechanism also occurs upon irradiation with 390 nm light, and it is the cause for the desorption rates observed. Understanding this point defect formation and diffusion mechanism would allow for precise control of point defects in semiconductors.

Lastly, this thesis will also examine the results of irradiation of silicon with UV light. It will be shown that this irradiation leads to an enhancement of the growth of oxide that cannot be explained thermally. Furthermore, the oxide that grows does not necessarily form in the SiO_2/Si interface, as would be expected, but also grows in the air/SiO_2 interface. Growth at the latter interface has not previously been observed in thermal, nanosecond [12], or Continuous Wave (CW) [13] oxidation of Silicon. It will also be shown that to explain the flux of Si atoms that make up the oxide that forms at the SiO_2/Si interface, the ultrafast enhanced diffusion mechanism must be invoked once again. This latter point is evidence that the point defect formation and diffusion mechanism is universal for semiconductors.

Thus, the goals for this thesis can summarized as:

1. To establish the role of desorption on the formation of periodic structures

2. To demonstrate that enhanced mass transport occurs upon irradiation with ultrafast laser pulses in GaAs.

3. To present a model for the growth of thick SiO_2 oxides at rates orders of magnitude higher than previously observed upon ultrafast irradiation.

4. To demonstrate that the enhanced mass transport mechanism is universal mechanism that occurs upon ultrafast irradiation of semiconductors.

The most important aspect of this thesis is that an excited state enhanced point defect formation and diffusion mechanism is behind a large portion of the morphological effects that are observed upon irradiation. This point defect mechanism appears to be independent of the irradiation material, having been observed both in GaAs and in Silicon. It also appears to occur no matter what the irradiation wavelength or environment is. This universal mechanism should then be considered as a critical aspect of the phenomena that occur upon ultrafast irradiation.

CHAPTER II

Background

2.1 Timescale of Interactions

When light is incident on a material, the energy is initially absorbed by the carriers. With continuous wave and nanosecond lasers, this excitation occurs alongside thermal effects. With ultrafast lasers, which have a temporal bandwidth of less than a picosecond, the energy is completely absorbed before any thermal equilibrium between carriers or with the carriers and the lattice can occur. This means that after excitation, the material undergoes various thermalization mechanisms free from active influence of the laser. A schematic of these mechanisms is shown in figure 2.1.

In materials with a direct band gap with energy lower than the photon energy, an individual photon can excite an electron into the conduction band. When the material has an indirect bandgap, a phonon must also be absorbed in order for excitation to occur. For materials with a band gap greater than the photon energy, Multi-photon absorption or tunneling ionization must occur [14]. Multiphoton absorption occurs when two or more photons are simultaneously absorbed with a total energy larger than the band gap. High electric fields are generally needed to achieve reliable multiphoton absorption, since the probability depends on the number of photons available for absorption. After the laser pulse is completely absorbed, the total energy of the excited carries does not increase. Initially, the excited electrons are coherent with the

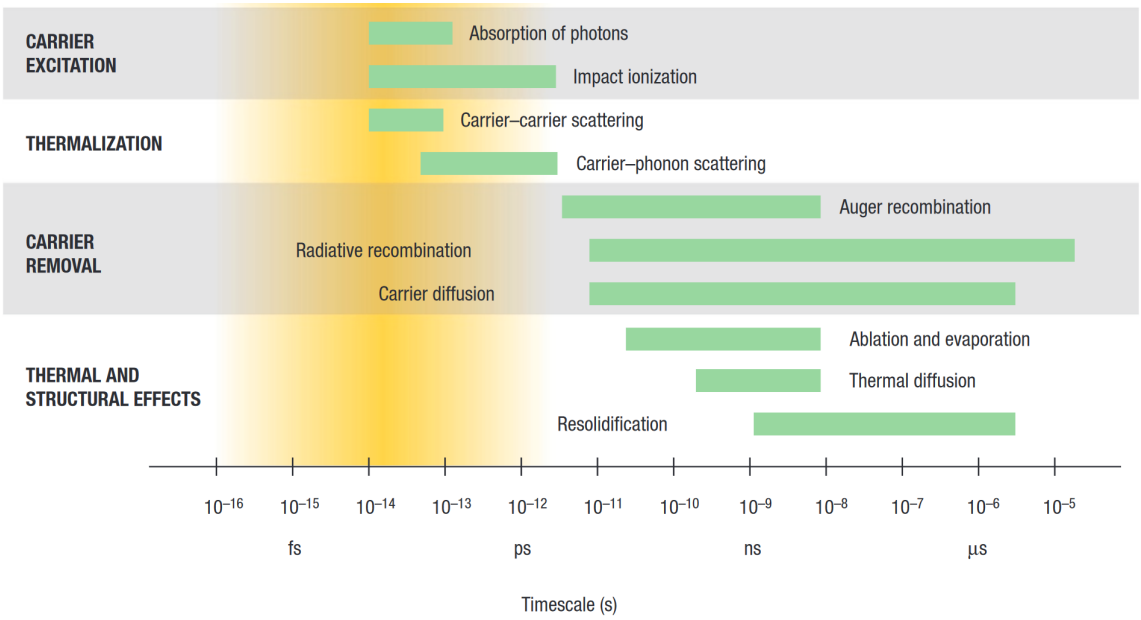

Figure 2.1: Timescales of electronic and lattice processes after ultrafast laser excitation in solids. The green bars represent an approximate range over which each process occurs. Adapted from S. K. Sundaram and E. Mazur, Inducing and probing non-thermal transitions in semiconductors using femtosecond laser pulses, Nature Materials, 1(4):217-224 (2002)

incident electric field, but after a few fs the carrier-carrier scattering causes dephasing [15]. Excited electrons with excess energy can collide with valance electrons to excite them in a process called impact ionization, although this does not increase the total energy of the excited electrons.

The electrons eventually thermalize to a Fermi-Dirac distribution after a few 100s of femtoseconds through carrier-carrier interactions [4, 16]. At this point in the process, the electrons are at an elevated temperature while the ions are still at room temperature. This is properly described by using the two-temperature model [4]. Since the electrons have much smaller mass than the ions, carrier-phonon interactions transfer a small amount of energy thus it takes a few ps before the carriers and lattice are in a thermal equilibrium [17].

Due to the band gap acting as an energy barrier, electrons do not immediately recombine. The electrons then stay in a Fermi-Dirac distribution in the conduction band until radiative or non-radiative recombination occurs. While this process begins occurring within 10 ps of excitation, it can take 10s of ns for the excited electrons to completely relax to the ground state. In radiative recombination, the excited electron releases a photon with energy equal to the band gap in order to return to the ground state. In non-radiative recombination, the energy released by the electron as it returns to the ground state is transferred to other electrons or to phonon modes. Recombination can occur both spontaneously and through stimulation. Stimulated recombination releases a photon with the same polarization, phase, and direction as the photon used to stimulate it. Spontaneous emission occurs randomly and uniformly in all directions. After a few hundred picoseconds, thermal diffusion starts, and the lattice begins to cool [17]. It is in this timescale, where thermal melting and ablation occur when high enough laser fluences are used.

2.2 Ultrafast Mechanisms

Phase transformation from solid to liquid occurring in sub-picosecond timescales, or ultrafast melting, was first observed in Si by Shank, et al [18]. Further pump probe studies done in Si have shown that while it takes a few hundred fs before the properties of liquid Si are observed, it takes only 150 fs before the crystal loses all cubic order [19]. The phase transformation in both studies was verified by measuring the change of the order-dependent second harmonic signal. Similar experiments done on GaAs have also shown similar results [20–22]. The second harmonic signal of GaAs was shown to vanish after 100 fs, while reflectively characteristic of a metallic molten phase was observed after 500 fs. This effect was attributed to the fact that at high excitation intensities, a dense electron-hole plasma can form which weakens the interatomic potential [1]. While the interatomic potential is weakened, atoms continue moving due to room temperature vibrational energy, causing a liquid-like region to form at timescales shorter than thermal effects can take place. This model for the state of the lattice upon irradiation was confirmed by synchrotron X-Ray diffraction experiments, which revealed that the diffraction intensity decreased by roughly 10% after excitation [23, 24]. The decrease of the intensity was associated with an increase in the root mean displacement of the lattice atoms.

Transient semiconductor to metal transitions, better known as bandgap collapse, has been observed in GaAs and Si after irradiation [1, 3, 25, 26]. This was verified by measuring the change in reflectively of GaAs by two-angle pump probe experiments. The measured reflectivity was then converted to the dielectric constant by inverting the Fresnel formula for reflectivity as a function of the incident angle. The studies indicate that the irradiated area exhibits metal like properties. Initially, this occurs due to screening from a dense electron-hole plasma, but further changes in the dielectric function occur due to lattice deformation from ultrafast melting [1]. When the minimum of the conduction band drops below the valence band, the dielectric

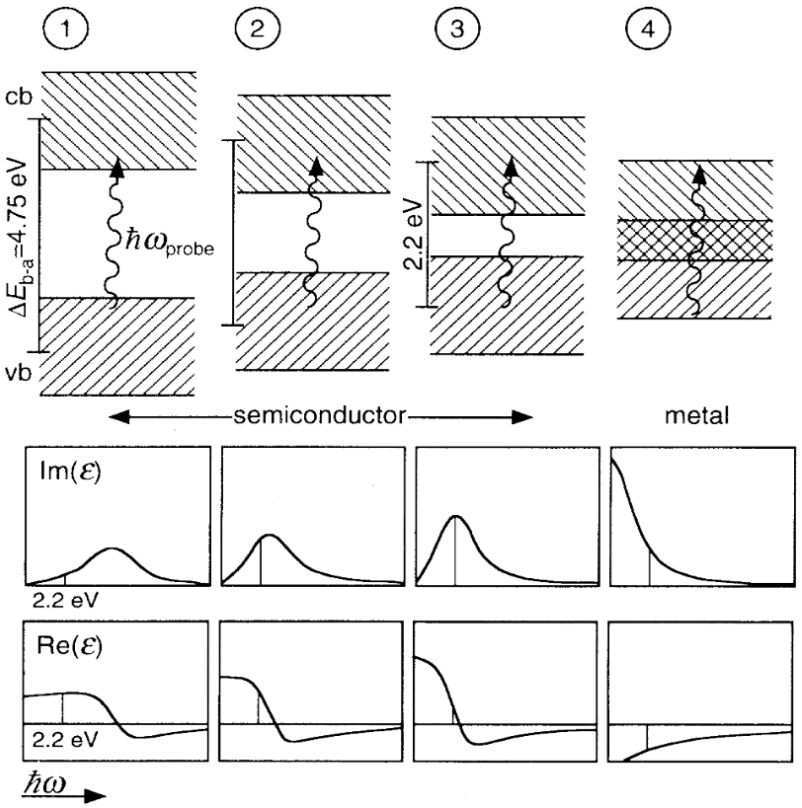

Figure 2.2: Schematic of the band structure and dielectric function during bandgap collapse. The conduction band of the semiconductor lowers, changing the dielectric function. When the conduction band minimum is lower than the valence band maximum, the dielectric function has the qualities of a that of a metal. Adapted from E. N. Glezer, Y. Siegal, L. Huang, and E. Mazur. Laser-induced band-gap collapse in GaAs. *Phys. Rev. B*, 51(11):6959–6970, March 1995

function of the semiconductor looks like that of a metal. A schematic of this process is shown in Figure 2.2. This transition was also observed by measuring the second harmonic signal, which showed that the second order non-linearity of the material disappeared during bandgap collapse [27, 28].

Studies on bandgap collapse done on Si have shown that the excited state dielectric function can be modeled during the excitation regime by combining the effects of (a) state and band filling from the density of excited e-h pairs, (b) band-structure renormalization from a shift in the band structure, and (c) the Drude-like free carrier response during and after excitation [1]. Taking all theses effects into account, the

excited dielectric can be calculated as:

$$\varepsilon_{ex}(\omega) = 1 + \underbrace{[\varepsilon_g(\hbar\omega + \Delta E_{gap}) - 1]\frac{N_0 - N_{e-h}}{N_0}}_{\text{Renormalization and filling effects}} - \underbrace{\left(\frac{\omega_p}{\omega}\right)^2 \frac{1}{1 + i\frac{1}{\omega\tau_D}}}_{\text{Free carrier response}} \tag{2.1}$$

where ε_g is the ground state dielectric function, ΔE_{gap} is the shift in the band structure, N_0 is the unexcited valence-band density, N_{e-h} is the density of the excited electron-hole pairs, ω_p is the excited state plasma frequency, and τ_D is the Drude damping time.

In GaAs, work done to model the dielectric function as a two-oscillator Drude-Lorentz model has shown good agreement with experimental results [3]. In this work, the expression for the excited state dielectric function is:

$$\varepsilon_{ex}(\omega) = 1 + \omega_p^2 \left[\frac{f_1}{(\omega_1^2 - \omega^2 + i\omega\Gamma_1)} + \frac{f_2}{\omega_2^2 - \omega^2 + i\omega\Gamma_2}\right] \tag{2.2}$$

where ω_p is the excited plasma frequency, f_i, ω_i, and Γ_i are the strength, resonant frequency, and spectral width of the ith oscillator. More recently, these two models have been combined in order to calculate the time dependent excited dielectric function of GaAs in a regime where no experimental results were available [8]. The combined expression for the dielectric function is:

$$\begin{aligned}\varepsilon_{ex}(\omega, t) = &\overbrace{1 + \omega_{pg}^2 \left[\frac{f_1}{\omega_1^2(t) - \omega^2 + i\omega\Gamma_1(t)} + \frac{f_2}{\omega_2^2(t) - \omega^2 + i\omega\Gamma_2(t)}\right]}^{\text{Two-Oscillator Lorentz term}} \\ &\underbrace{- \left(\frac{\omega_p(t)}{\omega}\right)^2 \frac{1}{1 + i\frac{1}{\omega\tau_D}}}_{\text{Drude e-h plasma term}}\end{aligned} \tag{2.3}$$

where $\omega_g p$ is the ground state plasma frequency, and the other variables are as defined for equations 2.1 and 2.2.

The effect on the band structure has been shown to be reversible if energies below the melt threshold are used, as the lattice disorder disappears once the inter-atomic potential is restored and point defects annihilate. Above the melt threshold of the material, the large temperature gradient caused by the rapid melting of the irradiated area leads to an amorphous region after resolidifcation. In this case, the changes to the electronic structure of the material are permanent [3].

At sufficiently high incident pulse energy, the rapid melting of the material can cause high pressures as the material heats up before it can expand. This causes a large pressure differential between the irradiated area, and the ambient air and unirradiated area. This launches a compression and tensile wave, which if high enough energy is used, the tensile wave can be strong enough to create a negative pressure region in the melted material [29]. Voids form and coalesce in this region, until enough are formed to separate the melted region from the bulk. When this occurs, the pressure differential between the air and melt cause the top region to spallate, leaving a smooth crater behind [30–32]. The ablation threshold depends on the material, and has been shown to be extremely sharp [33].

2.3 Laser Induced Periodic Surface Structures

Laser Induced Period Surface Structures (LIPSS) generally occur after multiple irradiations of the material below the ablation threshold. LIPSS can be separated between Low-Spatial Frequency LIPSS (LSFL) and High-Spatial Frequency LIPSS (HSFL).

2.3.1 LSFL

LSFL is the better understood of the two types of LIPSS. It is generally characterized by a spatial period greater than half the wavelength of the incident light. It appears perpendicular to the laser polarization in metals and semiconductors when

irradiating with energies above the band gap [34, 35], but parallel to the laser polarization in semiconductors when the photon energy is lower than the band gap and in insulators [36, 37]. It has been observed experimentally upon irradiation with CW [38, 39], ns [40], and fs [41–43] lasers.

In metals, the incident light couples with the surface roughness to excite Surface Plasmon Polaritons (SPPs). The light then interferes with the SPPs, which causes regions of higher and lower intensities [44–48]. The regions with higher intensity are the ablated, thus forming a periodic structure below the original surface [44, 49–51]. In insulators, the cause of the LSFL is due to radiation remnants, which is a non-propagating mode caused by rough surfaces that can deposit energy into the material [52]. The formation of LSFL has been modeled by Sipe et al [44] and has been shown to have good agreement with experimental results [38].

2.3.2 HSFL

HSFL formation is still under much active research. It is characterized by a spatial period of less than half of the laser wavelength. HSFL has been observed in both metals and semiconductors [53], as well as perpendicular and parallel to the laser polarization [54]. Multiple irradiations are necessary for HSFL formation to occur, as HSFL formation is commonly driven by a feedback mechanism [9]. Since the Sipe theory does not include feedback mechanisms, it does not predict HSFL formation [41, 55]. Literature suggests that there are two distinct types of HSFL [9], and the number of different models present in the literature suggest that the mechanism for HSFL formation can differ between materials.

The first type of HSFL most commonly appears in dielectrics and semiconductors, and is characterized by having a large depth to corrugation period aspect ratio [56–58]. There are various models in the literature that are used to explain HSFL formation, such SPP coupling [46, 59], nanoplasma generation [60–62], harmonic generation [41,

55, 63], and asymmetry of the electron kinetic energy after irradiation [64]. The other type of HSFL is observed on metal surfaces and is characterized by having a corrugation depth of only a few tens of nm [65]. As with the previous type of HSFL, different models exist in the literature to explain the formation of HSFL such as oxidation [66] and twinning effects after melting [67].

Studies of HSFL formation in GaAs with 780 nm light shows that point defect diffusion is of importance [5, 8]. To summarize the mechanism pointed out in these studies, the initial pulses create a high concentration of vacancy/interstitial pairs in the bulk of the material. The highly stressed interstitials [68] migrate to the surface and coalesce into randomly aligned islands [6]. Island growth is driven by further diffusion of interstitials. Once the islands are large enough, they can interact with the incident laser in order to excite surface plasmon polaritons [69]. GaAs cannot support SPPs, but as mentioned in preceding chapters, ultrafast excitation can cause sufficient electrons to excite to the conduction band and give GaAs metal-like properties [3]. Interference of the incident laser with the SPPs then create areas with higher and lower intensity. Mass transport occurs preferentially where the laser is most intense, which leads to alignment of the islands. Further mass transport of interstitials to the islands and vacancies to the area between islands leads to formation of a corrugated surface. No changes of the periodicity occur until the trenches deepen and a higher energy mode of the SPP can be excited [70]. For the SPPs whose kx equals half of the grating period, Bragg scattering causes waves that travel in both the forward and backward direction to interfere and form standing waves. This standing wave can either have nodes at the top and bottom of the corrugation, or at the sidewalls [71]. A band gap in the SPP dispersion curve is formed because of the difference in energy of the standing waves with the same wavelength. Proper introduction to SPPs will follow in the next section. The density of states is much higher at the Brillouin zone boundary (355 nm) which leads to LIPSS with a 355 nm period.

Relaxation through bifurcation of the highly stressed corrugations leads to 185 nm HSFL [72, 73]. Interstitials continue diffusing to the crest of the grating where the material is in tensile stress, and vacancies diffuse to the troughs of the grating where the material is being compressed.

2.4 Surface Plasmon Polaritons

2.4.1 Surface Plasmon Polaritons at a Single Interface

A surface plasmon polariton, or SPP, is an electromagnetic excitation that travels along the interface between a metal and a dielectric (Polariton) as well as oscillations in the free electron density near the surface (Plasmon) [74]. The wave decreases in amplitude exponentially into each medium. The SPP dispersion function can be derived starting with the wave solution to Maxwell's equation[69]. Assume there is a transverse magnetic wave traveling along the interface in the x direction:

For the region in the dielectric (z > 0):

$$\vec{E}(\vec{x},t) = -A\frac{c}{i\omega\epsilon_d}(k_z^d, 0, ik)e^{ikx_1 - k_z^d z - i\omega t} \tag{2.4}$$

$$\vec{H}(\vec{x},t) = (0, A, 0)e^{ik_x x - ik_z^m z - i\omega t} \tag{2.5}$$

And for the region in the metal (z < 0):

$$\vec{E}(\vec{x},t) = -B\frac{c}{i\omega\epsilon_m}(-k_z^m, 0, ik)e^{ikx_1 + k_z^m z - i\omega t} \tag{2.6}$$

$$\vec{H}(\vec{x},t) = (0, B, 0)e^{ik_x x + ik_z^m z - i\omega t} \tag{2.7}$$

Applying the boundary condition that the waves must match at the interface

(z=0),

$$\frac{k_z^d}{k_z^m} = -\frac{\epsilon_d}{\epsilon_m} \tag{2.8}$$

For irradiation in air or vacuum, $\epsilon_d = \epsilon_0$. Since a material's dielectric function is frequency dependent, then $\epsilon_m = \epsilon(\omega)$. The above equation can be rewritten for simplicity as:

$$\frac{k_z^m}{k_z^d} = -\frac{\epsilon(\omega)}{\epsilon_0} \tag{2.9}$$

Since k and ϵ_0 are positive, in order for an SPP to be excited the real part of the dielectric function in the material needs to be negative. As was pointed in the preceding section, ultrafast lasers can excite a sufficient number of electrons into the conduction band, temporarily driving the real part of the dielectric function negative [1, 3]. This occurs within the first few fs [8], thus the rest of the pulse can interact with the now metal-like material and excite SPPs.

In order to calculate the dispersion relation, the above equation is combined with the conservation of momentum in each medium:

$$(k_x)^2 + (k_z^d)^2 = \epsilon_0 \left(\frac{\omega}{c}\right)^2 \tag{2.10a}$$

$$(k_x)^2 + (k_z^m)^2 = \epsilon(\omega) \left(\frac{\omega}{c}\right)^2 \tag{2.10b}$$

Then we can get the dispersion relation of an SPP:

$$k_x = \frac{2\pi}{\lambda} \left(\frac{\epsilon_0 \epsilon(\omega)}{\epsilon_0 + \epsilon(\omega)}\right)^{1/2} \tag{2.11}$$

From this, it can be seen that the SPP wavevector will always be larger than the incident light's wave vector, indicating that extra momentum is necessary in order

for the incident light to couple to the SPP modes. To optically excite SPPs, prisms, probes, metamaterials, rough surfaces, and gratings are commonly used [69]. The excitation of SPPs due to surface roughness and gratings is of particular interest in this thesis.

Light that is scattered on rough surfaces can excite SPPs. In the near field, the scattered light contains all possible wave vectors [75], thus the scattered light whose wave vector falls within the SPP dispersion curve can excite SPPs. This excitation leads to low coupling efficiency and is generally non-resonant. On the other hand, grating coupled SPP excitation is more efficient. Components of the diffracted light from a grating whose wavevector is equal to the SPP wavevector will more strongly excite SPPs. Since the grating diffracts the light to only a select number of wavevectors, then the SPP coupling will be more efficient than with a rough surface. The diffracted light on the surface has the following form [74]:

$$\vec{k}_x = \frac{\omega}{c}\ sin(\theta)\ \pm\ l\frac{2\pi}{A} \tag{2.12}$$

where A is the grating constant, θ is the angle of incident, ω is the angular frequency of the incident light, and l is an integer. For a wave in normal incidence to the grating the dispersion relation for grating coupled SPP becomes:

$$\vec{k}_{sp} = \frac{\omega}{c}\sqrt{\frac{\epsilon_0\epsilon(\omega)}{\epsilon_0 + \epsilon(\omega)}} = \pm\ l\frac{2\pi}{A} \tag{2.13}$$

Using this relation, the wavevector of the resulting SPP can be determined as long as the wavelength of the incident light and dielectric function of the material, or the period of the of the grating are known.

The above result only applies to SPP excitation from gratings that are only a small part of the excited area, or the grating features are small enough that the surface roughness can be assigned an effective refractive index [69]. The SPP dispersion

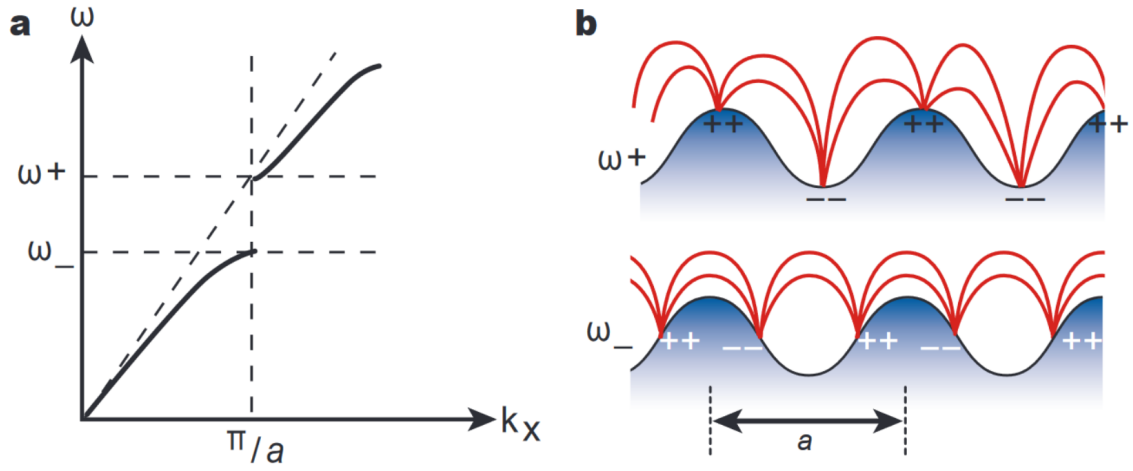

Figure 2.3: (a) Grating coupled Surface Plasmon Polariton (SPP) dispersion relation showing a band gap. (b) Both of the field/charge configurations that can be present when the SPP strongly couples with the grating. The upper frequency solution has higher energy due to larger charge separation and more distorted field. Adapted from William L. Barnes, Alain Dereux, and Thomas W. Ebbesen. Surface plasmon subwavelength optics. *Nature*, 424(6950):824–830, August 2003

changes when the grating is large enough that the SPP can strongly interact with the periodic surface. A special case of this interaction occurs when the period of the corrugation is half of the SPPs wavelength, where forward and backward traveling waves interact to form standing waves [71]. This standing wave can have two different modes; one where the nodes and charges are located at the sidewalls, and another where they are located at the top and bottom of the grating [70]. These two standing wave solutions have the same wavelength, but different energy. The solution with nodes at the top and bottom has higher energy than the other solution due to field distortion and larger charge separation [70]. Waves with energies between the two solutions destructively interfere with each other, thus forming a band gap in the SPP dispersion curve. The formation of a photonic bandgap in the SPPs band structure has been experimentally verified [76]. Figure 2.3 shows a schematic of the two different configurations that can be present in a periodic grating, as well as the SPP dispersion curve of a grating coupled SPP.

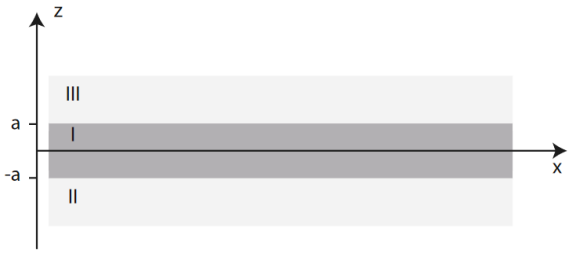

Figure 2.4: A schematic representation of a thin metal slab between two dielectrics. In the systems presented in this thesis, region I is the excited semiconductor, region II is the unexcited semiconductor, and region III is air. Figure adapted from Stefan A. Maier. *Plasmonics: fundamentals and applications.* Springer, New York, 2007

2.4.2 Surface Plasmon Polariton Propagating in Multiple Interfaces

Another system of interest for propagation of SPP is that of multiple layers of alternating metallic and dielectric material. As discussed before, during excitation the formation of an electron-hole plasma gives the excited material metal-like properties. Since the laser only penetrates a certain distance into the material, it results in a volume of highly excited material surrounded by air, and unexcited material. This in turn, can be loosely modeled as a thin slab metal surrounded by dielectric material, where SPPs can propagate at both interfaces. One pitfall of this system is that the during excitation the unexcited/excited interface is not an accurate physical representation, since the level of excitation decreases exponentially. Nonetheless, a system like this has been able to accurately predict the formation of HSFL in various materials and environments [77]. A schematic of this system can be seen in Figure 2.4

Consider TM waves traveling along each interface exponentially decaying in the dielectric layers. Similar to the formalism for a single interface, for z > a, the electric and magnetic field has the form:

$$H_y = Ae^{i\beta x}e^{-k_3 z} \tag{2.14a}$$

$$E_x = iA\frac{1}{\omega\varepsilon_0\varepsilon_3}k_3 e^{i\beta x}e^{-k_3 z} \tag{2.14b}$$

$$E_z = -A\frac{\beta}{\omega\varepsilon_0\varepsilon_3}e^{i\beta x}e^{-k_3 z} \tag{2.14c}$$

and similarly for z < -a

$$H_y = Be^{i\beta x}e^{k_2 z} \tag{2.15a}$$

$$E_x = -iB\frac{1}{\omega\varepsilon_0\varepsilon_2}k_2 e^{i\beta x}e^{k_2 z} \tag{2.15b}$$

$$E_z = -B\frac{\beta}{\omega\varepsilon_0\varepsilon_2}e^{i\beta x}e^{k_2 z} \tag{2.15c}$$

where k_i are the wave vectors perpendicular to the interface, β is the propagation constant, or the wave vector of the SPP in the slab, and the other variables have their usual meaning. Inside the metallic layer, -a < z < a, there are two waves localized at each interface, thus the resulting electric and magnetic field in the slab is given by:

$$H_y = Ce^{i\beta x}e^{k_1 z} + De^{i\beta x}e^{-k_1 z} \tag{2.16a}$$

$$E_x = -iC\frac{1}{\omega\varepsilon_0\varepsilon_1}k_1 e^{i\beta x}e^{k_1 z} + iD\frac{1}{\omega\varepsilon_0\varepsilon_1}k_1 e^{i\beta x}e^{-k_1 z} \tag{2.16b}$$

$$E_z = C\frac{\beta}{\omega\varepsilon_0\varepsilon_1}e^{i\beta x}e^{k_1 z} + D\frac{\beta}{\omega\varepsilon_0\varepsilon_1}e^{i\beta x}e^{-k_1 z} \tag{2.16c}$$

Since continuity is required at each interface for H_y and E_x, at z = a:

$$Ae^{-k_3 a} = Ce^{k_1 a} + De^{-k_1 a} \tag{2.17a}$$

$$A\frac{1}{\varepsilon_3}k_3 e^{-k_3 a} = -C\frac{1}{\varepsilon_1}k_1 e^{k_1 a} + D\frac{1}{\varepsilon_1}k_1 e^{-k_1 a} \tag{2.17b}$$

and for z = -a:

$$Be^{k_2 a} = Ce^{-k_1 a} + De^{k_1 a} \tag{2.18a}$$

$$-B\frac{1}{\varepsilon_2}k_2 e^{-k_2 a} = -C\frac{1}{\varepsilon_1}k_1 e^{-k_1 a} + D\frac{1}{\varepsilon_1}k_1 e^{k_1 a} \tag{2.18b}$$

This system of equations can be solved, which results in the dispersion relation:

$$e^{-4k_1 a} = \frac{\frac{k_1}{e_1} + \frac{k_2}{e_2}}{\frac{k_1}{e_1} - \frac{k_2}{e_2}} \times \frac{\frac{k_1}{e_1} + \frac{k_3}{e_3}}{\frac{k_1}{e_1} - \frac{k_3}{e_3}} \tag{2.19}$$

It should be noted that for a = ∞, Equation 2.19 reduces to the equation for two uncoupled SPPs. One other constraint is that H_y needs to still satisfy the wave equation for TM modes:

$$\frac{\partial^2 H_y}{\partial z^2} + (k_0^2 \varepsilon - \beta^2) H_y = 0 \tag{2.20}$$

thus

$$k_i^2 = \beta^2 - k_0^2 \epsilon_i \tag{2.21}$$

The combination of equation 2.19 and 2.20 form an implicit equation linking β and ω, which can be solved numerically.

2.5 Desorption

Another mechanism that can occur during laser excitation is desorption. Desorption is the removal of individual atoms from the surface of the material. It occurs both thermally [79] and electronically [80]. In thermal desorption, energy from heat is transferred to the atom, which increases its vibrational energy. Once the vibrational energy is high enough to overcome the binding energy, the atom will desorb from the surface.

Electronic desorption, often called Desorption Induced by Electronic Transitions (DIET) or Desorption Induced by Multiple Electronic Transitions (DIMET) in the literature, has been observed in irradiation with electrons and light at fluences below the melt threshold [81]. The exact mechanism for light driven desorption varies depending on the material type, and the type of laser used.

One simple and commonly used model for describing desorption through electronic transitions in metals was discovered by Menzel, Gomer, and Redhead [82, 83]. To summarize the model, if the absorption of the photon results in a Franck-Condon transition, then it leads to a change of the potential energy curve of the atom. Once the atom is in the excited potential energy curve, it is accelerated towards the excited potential curve origin. If the atom is only in the excited state for a short period of time, then when the atom returns to the ground state it does not gain enough vibrational energy to overcome the binding energy. On the other hand, if the excited state lifetime is sufficiently long, then an atom can gain enough energy to be desorbed. When high intensity lasers are used, then the possibility of multiple excitations allows for a higher probability of desorption. In this case, the already excited atom can undergo multiple excitations within the relaxation time in order to further increase the kinetic energy gained [84].

Another mechanism for desorption, called the two-hole localization mechanism, has also been studied [85, 86]. This has been shown to occur when irradiating with

ns and fs lasers [87]. If two holes become localized in the same atom upon excitation, then the binding energy of the atom is low enough that they can be readily desorbed. Two holes can become localized in the same bond due to an Anderson negative-U interaction [88]. In this, two holes attract each other when the energy gain from the lattice relaxation exceeds the Coulombic repulsion of the two holes. Normally, the holes have to be significantly close in order for the holes to feel the attractive potential, and the long range of the Coulombic interaction make this extremely improbable, as two holes usually never get close enough. On the other hand, in a sufficiently dense e-h plasma, the plasma can screen the Coulombic interactions which allow the holes to get close enough to interact attractively [85]. The two holes lead to the rupture of the bond and the atom is ejected as the holes repel each other.

In GaAs and GaP, it has been shown that desorption occurs predominantly through defects on the surface [89–91]. In these experiments with ns lasers, GaAs and GaP were irradiated after bombarded with Ar ions. They noted that two different Ga emission rates appeared, a rapidly decaying one and a slowly decaying one. The rapidly decaying rate appeared again if the same sample was bombarded with Ar ions or Ga was deposited, indicating that the rapidly decaying signal was from adatom type defects. The slowly decaying signal was attributed to kink sites. The mechanism used to explain this desorption is cascade excitation, in which the localization of a electron-hole pair in the defect induces a metastable state, which can then be further re-excited by photons during the same laser pulse and brought to a anti-bonding state [92]. In GaP the desorption yield decreases as the photon energy increases across the band gap energy, while in GaAs the desorption yield increased as the photon energy increased.

2.6 Semiconductor Oxidation

2.6.1 Thermal Oxidation of Silicon

One of the simplest, yet still widely used models for the formation of oxide is the Deal-Grove model [93]. The basis of this model is that the growth of SiO_2 in Silicon occurs at the SiO_2/Si interface, and that all the physics can be contained in two parameters (A, B), which can be experimentally determined. The first step for the formation of the oxide is then adsorption of the oxidant species on the oxide, and it can be determined by the flux equation:

$$F_{ads} = k_c(C_{sol} - C) \tag{2.22}$$

where k_c is the mass transfer coefficient, C_{sol} is the solubility limit of the oxide, and C is the concentration of the oxidant species at a given time. The next step of the oxide formation process is the transport of the oxidant species through the SiO_2, and it can be described using Fick's law:

$$F_{diff} = D\frac{\partial C}{\partial x} \approx D\frac{C - C_{int}}{x_0} \tag{2.23}$$

where D is the diffusion coefficient of the oxidant in the oxide, C_{int} is the concentration of the oxidant in the SiO_2/Si interface, and x_0 is the thickness of the oxide.

The last step is the reaction at the SiO_2/Si interface. The flux of oxidants consumed by these reactions can be expressed as:

$$F_{int} = k_s C_{int} \tag{2.24}$$

where k_s is the surface reaction rate and encompasses all the different processes that can occur at this interface during the formation of the oxide. In the steady state,

these fluxes were made equal to each other, thus the flux can be expressed as:

$$F = \frac{C_{sol}}{1/k_s + 1/k_c + x_0/D} \tag{2.25}$$

The oxide growth rate is then directly proportional to the rate in which oxygen is being consumed at the interface:

$$\frac{\partial x_0}{\partial t} = \frac{F}{M} = \frac{C_{sol}/M}{1/k_s + 1/k_c + x_0/D} \tag{2.26}$$

where M is the number of oxidant molecules that are incorporated per unit per unit volume in the oxide. This equation was simplified by:

$$\frac{\partial x_0}{\partial t} = \frac{B}{A + 2x_0} \tag{2.27}$$

Where

$$A = 2D\left(\frac{1}{k_s} + \frac{1}{k_c}\right) \tag{2.28a}$$

$$B = 2\frac{DC_{sol}}{M} \tag{2.28b}$$

are known as the Deal-Grove parameters. In order calculate how long it will take for a given thickness to grow, Equation 2.28 can be rearranged and integrated from time 0 to time t, and from an initial thickness at time zero x_i to the desired thickness x_0, then solving for t:

$$t = \frac{x_0^2 - x_i^2}{B} + \frac{x_0 - x_i}{B/A} \tag{2.29}$$

Where the first term is called the parabolic rate term and dominates for large thickness. The second term is called the linear rate term and dominates for thin

oxides. It should be noted that for very thin oxides (<30 nm), the Deal-Grove model does not properly predict the time during oxidation [94]. Nonetheless, the Deal-Grove model provides good agreement with experimental observations of thicker oxides.

One rate limiting step that is not explicitly included in the Deal-Grove model but is necessary to point out for better understanding Laser Induced Oxidation is diffusion through a blocking layer that forms near the SiO_2/Si interface [95]. This blocking layer, which is less than 10 nm thick, forms because the SiO_2 is much denser near the interface. This density increase means that the large O and H_2O molecules have a decreasingly lower diffusion rate the closer they are to the interface.

2.6.2 Light Enhanced Oxidation of Silicon and GaAs

Light has been known to enhance the growth rate of oxides on some semiconductors surfaces up to 60% [96]. The incident light enhances the growth both through heating the irradiated area, and through electronic excitation. The mechanism and enhancement of the growth depends on the material. It can also vary depending on the thickness of the oxide layer, as the limiting rate changes over the growth. In silicon, oxide grows at the interface between the silicon substrate and the SiO_2 layer [93]. When the layer is thin, the limiting rate is the interfacial silicon-oxygen reaction. The breaking of the bonds in the $Si - SiO_2$ interface has been suggested as mechanism for the enhancement of oxide growth which can enhance growth in this regime [96].

When the oxide layer is much thicker, oxygen needs to traverse from the atmosphere to the interface, thus the limiting rate is the diffusion of oxygen through the SiO_2 layer, and more specifically, through the blocking layer briefly mentioned before. Studies done with various wavelength of light have provided some indication to how the growth of oxide is optically enhanced. In one investigation, Si was irradiated with various wavelengths of light between 752.9 and 350.7 nm while the sample was heated to a temperature range of 770-900° in both dry and wet conditions [13]. The

enhancement due to light in dry oxygen decreased linearly until UV light was used, where the enhancement increased dramatically. This was attributed to the fact that barrier height to excite electrons from the conduction band of the Si into the conduction band of the SiO_2 is 3.2 eV, and the UV light used was 3.5 eV. The electrons in the SiO_2 can then combine with O or O_2 to form negatively charged species. Charged oxygen species have been suggested to be important in the growth of SiO_2 [95, 97, 98], thus an enhancement in the formation of these species can lead to an enhancement in the growth rate. It has also been suggested that the formation of O and O^- increase the oxidation rate due to the fact that atomistic oxygen takes up less volume than molecular oxygen [1], thus can diffuse more easily through the dense blocking layer near the interface. Another wavelength dependent study used irradiated Si with 193 nm light and 248 nm light with a 17 ns excimer laser at various intensities [12]. They noted an that the growth was enhanced the most when using the 193 nm light. They concluded that this increase in enhancement is due to the photodissociation of oxygen molecules, which occurs at wavelengths shorter than 240 nm. It can then be inferred that no matter what laser wavelength or pulse duration is used, the enhancement of the oxidation rate in Silicon appears to be solely caused by the increased availability of atomic oxygen.

Oxide growth on GaAs initially occurs at the interface of the oxide and the GaAs substrate, thus it is driven by the diffusion of oxygen from the surface to the interface [99], but is then caused by the diffusion of Ga and As atoms through the oxide. Studies have shown that the effect of laser irradiation at low intensities with visible light results in the growth of oxides that cannot be fully explained if only thermal effects were taken into account [100]. The enhanced oxide growth is attributed to the formation of electron hole pairs in the surface, which increase oxygen adsorption through charge transfer. This enhancement saturates after 1 monolayer of oxide has

[1] Molecular oxygen has a volume of 0.45 nm^3, while atomic oxygen has a volume of 0.05 nm^3

grown. On the other hand, a study done with UV light has shown that enhancement occurs even past 1 monolayer of coverage [101]. In this study, the GaAs substrate was irradiated with 23 ns laser pulse with 193, 248, and 351 nm wavelengths. They noted that the growth rate was enhanced when using light with energy higher than 4.1 $\pm$ 0.2 eV. This was attributed to the energy necessary to transfer electrons into the conduction band of the oxide, which is one of the proposed mechanisms for enhancements of SiO_2 growth in Si.

While studies have been done on the growth enhancement of oxides in GaAs and Si with ns and cw lasers, very little work has been done with femtosecond or picosecond lasers.

2.7 Diffusion in Semiconductors

2.7.1 Fick's laws and Brownian Motion

Macroscopic diffusion of interstitials in a semiconductor can be described using Fick's law [102]:

$$J = -D\nabla C \tag{2.30}$$

where J is the flux of atoms, D is the diffusivity, and C is the concentration. Simply put, this equation reveals that diffusion of atoms is dependent on the gradient of the concentration, and the diffusion coefficient. The dependence on the gradient of the concentration mainly indicates the simple concept that atoms diffuse from places of high concentration to low concentration. The diffusion coefficient is a phenomenological value that is generally found experimentally, and depends on the material in which diffusion is occurring, the type of atom that is diffusing, temperature, and pressure. It can be described by an Arrhenius equation:

$$D = D_0 e^{-E_a/k_b T} \tag{2.31}$$

where D_0 is the exponential pre-factor and is experimentally found, E_a is the activation energy for the specific diffusion process being described, k_b is the Boltzmann constant, and T is the temperature.

Another useful equation used for describing diffusion arises as a result of applying conservation of mass to Fick's first law [102]. This equation is called Fick's second law:

$$\frac{\partial C}{\partial t} = D\nabla^2 C \tag{2.32}$$

which simply states that the rate of change of the concentration at a specific time is proportional to the curvature of the concentration profile. This equation is a simplification of the convection-diffusion equation in the limit that no mass transport by convection occurs.

While Fick's law takes a macroscopic look at concentration, it is often useful to look at microscopic diffusion of individual particles, in other words, how fast are the particles moving. This is called Brownian motion, after botanist Robert Brown who first noticed this phenomenon while looking at pollen in water. A full theoretical model of this motion was then worked out by Einstein[103], and later experimentally verified by Perrin [104]. The result from this model most important for this thesis is that the mean squared displacement of a particle is non-vanishing, and can be described by[105]:

$$\bar{x^2} = 2nDt \tag{2.33}$$

where D is once again the diffusion coefficient, t is the time, and n represents the number of dimensions the particle is free to move in. With this equation, given

a diffusivity, one can estimate the time it takes for a particle to move a certain distance, or vise versa. Fick's first law and the mean square displacement equation will be used in Chapter 5 to demonstrate the anomalous diffusion observed upon ultrafast irradiation.

2.7.2 Diffusion Processes

Diffusion in semiconductors can in general be split in two distinct categories: interstitial and vacancy mediated diffusion. Interstitial diffusion is characterized by the motion of atoms from interstitial sites, either to another interstitial site or to a lattice position. While there are various mechanisms for interstitial mediated diffusion, this section will only briefly summarize the two dominant mechanisms, Direct interstitial diffusion and Indirect Interstitial diffusion[2]. In direct interstitial diffusion, an interstitial with enough energy to displace lattice atoms can simply hop from one interstitial site to another. In indirect interstitial diffusion, the interstitial atoms displace a lattice atom and takes its place, which causes the atom that was in the lattice to now be in an interstitial site. Indirect diffusion occurs predominantly in systems where the interstitial atom is large, thus would require a large distortion of the lattice in order to cross to another interstitial position. Vacancy mediated diffusion, as the name suggests, is when the atomic motion is caused by the motion of interstitials. In this mechanism, an atom in a lattice neighboring a vacancy can have enough kinetic energy to exchange with the vacancy.

In GaAs, which is of particular interest for this thesis, self-diffusion is predominantly a vacancy mediated process. Activation energies reported in the literature for self-diffusion in GaAs range from 2 eV to 6 eV [106]. This diffusivity data was found through radioactive isotope traced analysis [107], lattice constant annealing experiments[108], and electrical property measurements after annealing [109]. To

[2]Also called interstitialcy diffusion

better understand this large range in activation energies, a study looking at the energetics of different activation energies for Ga self-diffusion in the literature was done [106]. This study revealed that in the presence of equilibrium vacancy density near dislocations of the surface, diffusion is primarily caused by second nearest neighbor hopping of gallium vacancies. They further determined that this mechanism is consistent with the activation energies in the range of 3-4 eV. On the other hand, they stated that the 6 eV activation energies are consistent with a mechanism that invokes the formation Frenkel-pairs deep in the bulk where vacancies are not as abundant. In order to determine the contribution on the diffusion from self-interstitials, a study which looked at impurity diffusion mechanisms which are self-interstitial mediated was done, which revealed activation energies for Ga self-diffusion of 4.89 eV (As rich crystals) and 3.37 eV (Ga rich crystals) [110]. It needs to be pointed out that this study reported a vacancy diffusion activation energy of 6 eV, thus the self-interstitial data should be compared only with the Frenkel-pair mechanism.

2.7.3 Photostimulated Diffusion

While no studies on whether femtosecond pulses non-thermally affect the diffusion of atoms in materials have been done, research shows that relatively low intensity CW light has an effect on the diffusion of interstitial atoms in n-type doped Silicon [111]. In this study, the concentration profile of ^{30}Si tracer atoms were analyzed after illumination with a 633 nm He-Ne laser at intensities from 0-1.5 W/cm^2. They suggest that because enhancement of the diffusion coefficient is significantly larger for n-type Si, the diffusion is stimulated by the ionization of interstitials by the trapping of electrons. They also state that further increase of the intensity has little effect on the charge state of Si interstitial and the enhancement saturates after 2 W/cm^2.

It has also been suggested that the source of photo-stimulated diffusion arises not from a direct effect of the laser's electric field, but from the recombination of photo-

excited electron-hole pairs at interstitial sites[10, 112, 113]. The cases for recombination enhanced reactions can be categorized as: Charge State Mechanism, Saddle-point mechanism, Energy-release mechanism[3], and Electronic-excitation mechanism. Figure 2.5 are the one-dimensional configuration-coordinate diagrams for each of the mechanisms. While an oversimplification of the problem, it is useful to refer to them when explaining the mechanisms.

The charge state mechanism, shown in Figure 2.5a, is simply that the barrier for an interstitial to hop to another site is dependent on the charge state of the interstitial. That is, the barrier for a negatively charged interstitial with a delocalized hole is smaller than that for other charge states. This is akin to the mechanism that is suggested for the enhancement of Si self-interstitials discussed previously [111]. Charge-state effects have been observed in both Si[114] and GaAs [115]. The saddle-point mechanism, also shown in Figure 2.5a, is very similar to the charge state mechanism, except in the limit where the energy barrier for a negatively charged defect to hop goes to zero. In this limit, the equilibrium position for the defect lies exactly between defect sites, thus during recombination there is equal chance for the defect to end up on either interstitial site. The energy-release mechanism, shown in Figure 2.5b, is when the defect is in a vibrationally excited state. In this mechanism, the capture of a hole leads to a non-radiative recombination from $[D^- + h]$ to $[D^0]$ where the lines intercept, which means that the thermal energy necessary to hop over the energy barrier is greatly reduced. The electronic-excitation mechanism, shown in Figure 2.5c, is analogous to the Energy-release mechanism when the defect is electronically excited. In this mechanism, the electronically excited defect has a lower energy barrier for hopping to another site than for the other states, thus increasing the probability for the hop to occur. Excitation effects have also been observed in doped Si and for electron traps in GaAs[10]. It should be noted that in most cases, it is not possible to

[3]Also called "Phonon-kick" mechanism

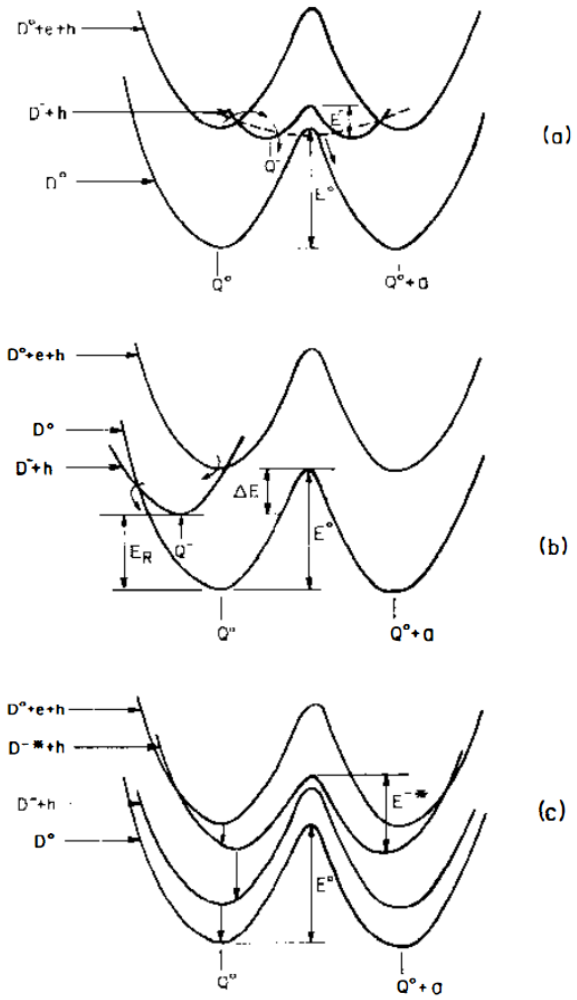

Figure 2.5: Configuration-coordinate diagrams of each of the mechanisms. (a) Charge State Mechanism and Saddle-point mechanism. (b) Energy-release mechanism. (c) Electronic-excitation mechanism. Adapted from D.V. Lang. Recombination-Enhanced Reactions in Semiconductors. Annu. Rev. Mater. Sci., 12 377, 1982

differentiate between each mechanism experimentally[10], thus all these mechanisms need to be considered when discussing electronic enhanced diffusion.

CHAPTER III

Experimental Procedures

3.1 Laser

Pulsed lasers are characterized by the fact that light is not emitted continuously, but as the name suggests, in pulses. The temporal profile of the pulses are most often Gaussian in the form of:

$$\vec{E} = E_0 \; e^{-4 \; ln \; 2 \; (\frac{t}{\tau})^2} \tag{3.1}$$

where E_0 is the amplitude of the pulse and τ is the full width half max (FWHM) of the pulse duration. The width of the pulse is dependent inversely on the bandwidth of the frequency components, thus the broader the bandwidth the shorter the pulse.

In this work, a linearly polarized, 1 kHz repetition rate Ti:Sapphire CLARK-MXR chirped-pulse amplified laser with a central wavelength of 780 nm, and a temporal width of 150 fs was used. Large changes in the power were achieved using ND filters, while fine tuning of the power was done using a combination of a half wave plate and a polarizing beamsplitter cube. The half wave plate was placed in a Newport rotation axis stage. The sample was placed on a Newport three-axis rotation stage.

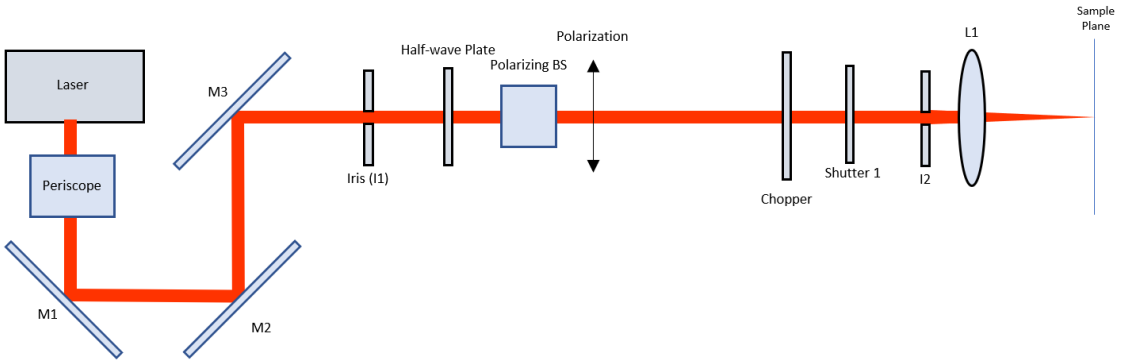

Figure 3.1: A schematic of the optical setup that is used as a basis of most experiments.

3.2 Sample Preparation

The samples were first diced with a diamond scribed to the appropriate dimensions. Samples were all cleaned in a sonic bath of acetone, then methanol, and finally ethanol. The samples were dried with Extra-Dry Nitrogen before the Ethanol could fully evaporate in order to limit the re-deposition of ethanol into the substrate. GaAs were placed in Ammonium Hydroxide (NH_4OH) for 15 minutes before being cleaned by the solvents in order to remove any excess oxide that grew during storage. They are then rinsed with deionized water before being cleaned with solvents.

3.3 Optical Alignment

Before any experiment can be done, alignment of the optical components in the optics table might need to be done. Figure 3.1 shows a schematic of the basic optical setup used for most experiments. First, the laser's current alignment needs to be checked in order to determine whether further alignment is necessary. To do this, use Iris 1 (I1) and Iris 2 (I2) to and see if the beam is centered. If it is, then no further alignment is necessary. If it isn't, then one must use Mirror 2 and Mirror 3 to align the laser to be centered in the iris. Use M2 to make the beam centered in I1, then

use M3 to make the beam centered in I2. Check whether the beam is still centered in I1. If it is, then the laser is aligned. If not, repeat the previous step until the beam is centered on both I1 and I2.

If the lens is being changed or the laser was considerably misaligned at the start, then the lens needs to be aligned. First, some sort of indicator needs to be placed in order to mark where the beam is incident without the lens. Then the lens is placed into the lens holder and moved until the beam is incident on the same marked spot. The lens must then be rotated until the reflected beam is retroreflected. If after the beam is rotated the beam is still incident on the marked spot, then alignment of the lens is done. If not, then repeat the previous steps, each time needing less movement until it is as aligned as it is necessary for your experiment. Note that the location of the lens will change depending on what focal length is being used.

To align the WinCamD camera, attach the objective tube and lens to the WinCamD. Move the stage back as far as it will go, (-49 mm). Then, use a level gauge connected to a post holder and press it to the side of the objective tube. Making sure that the objective will not hit any optics, move the stage forward 98 mm. If the reading in the dial gauge changes, rotate the camera the appropriate direction. Move the stage backwards, and if the reading changes again, then repeat rotate again. Continue until the reading in the dial gauge hardly changes.

3.4 Measuring and Aligning Laser

Since the ablation threshold if silicon is well known and has a sharp threshold, the laser was checked for day-to-day consistency by measuring it. First, the beam profile has to be known. A WincamD beam profiler is used to measure the beam properties at focus. Power was then measured using a thermal power meter then converted to peak fluence using the relation $F = 2\frac{E}{A}$ where E is the energy per pulse and A is the area at focus. The position of focus was found by irradiating a Silicon sample

until the area with the smallest damage diameter was found. Once that was found, two different methods for calculating the silicon threshold were used. For day to day measurements, the power was lowered until there was damage in the sample for only 50% of the irradiation events and a threshold fluence was calculated using said power. After any major alignment or if there was any indication that more thorough study was necessary, then the silicon was irradiated at various fluence above the ablation threshold. An average ablation damage radius per fluence was then obtained. A two-parameter fit [116] was then used to calculate the ablation threshold:

$$r = r_0 \sqrt{\frac{1}{2} ln\left(\frac{F}{F_{th}}\right)} \tag{3.2}$$

where r is the damage radius at a given fluence, r_0 is the radius of the incident beam, F is the fluence, and F_{th} is the threshold fluence. For this method, r_0 is not necessary to be known, although using the beam profiler anyways allows for further verification of the method if the measured and calculated beam radius is equal.

If the vacuum chamber is being used, then the same method as above can be used, with some added caveats. Since the glass in the focused laser's beam path can affect the focus position, then it needs to be accounted for. To do this, the vacuum window needs to be used while irradiating the Si sample to find the focus, then removed before it is brought back to the microscope. Furthermore, the laser power needs to be measured with the vacuum window in front of the power meter.

3.5 Second Harmonic Generation

In order to do the experiments with 390 nm light, the laser was converted to this wavelength through a process called second harmonic generation (SHG). SHG is a two photon process that requires a non-linear optical medium. In our experiments, a beta-barium borate (BBO) crystal was used. In order for SHG to occur, the crystal

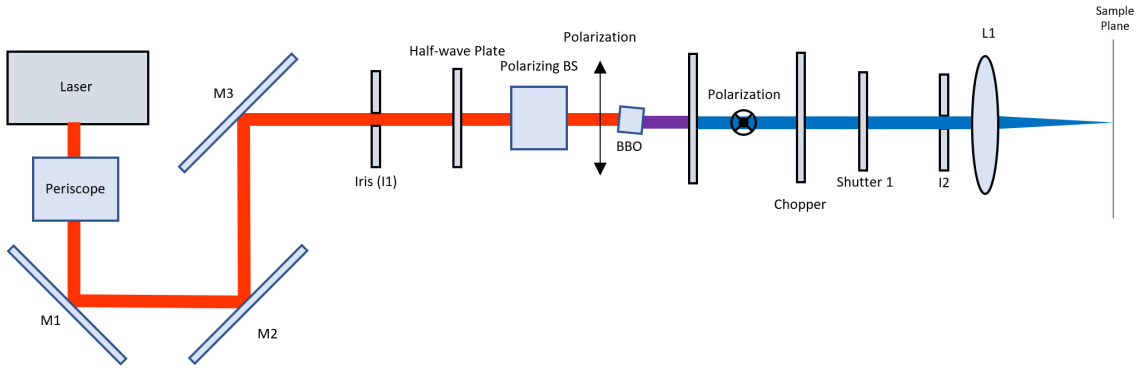

Figure 3.2: A schematic of the optics setup with the additional optics required for second harmonic generation. Note the shift in the beam position after it passes through the beta-barium borate (BBO) crystal.

has to be cut at a specific angle in order for the input and output signal to be in phase. The thickness of the sample also needs to be determined, as too thin it will not generate enough signal and too thick will result in too large of a group velocity mismatch between the input and output signals, lowering the efficiency of the SHG. The correct angle and thickness were calculated using the free SNLO software package. The optimal cut angle for Type I SHG was calculated to be $\theta = 30°$.

The BBO crystal used for the second harmonic experiments is a Type 1 crystal cut at $\theta = 29.2°$. The beam profiler should not be used for 390 nm light due to its low sensitivity, thus the radius of the beam is calculated using the more thorough silicon threshold method. Since there is a small mismatch between the optimal angle and the crystal angle, alignment of the crystal tilt is necessary in order to achieve maximum efficiency. Furthermore, since the normal vector of the crystal surface is not parallel to the incident beam's propagation direction, the lens must be aligned.

To align the rotation of the second harmonic crystal, put the power meter in the beam path after the bandpass filter, as to only measure the second harmonic signal. As a starting point, if the crystal has not been previously aligned, rotate the crystal in the mount until the line depicting the optical axis is completely horizontal. Then

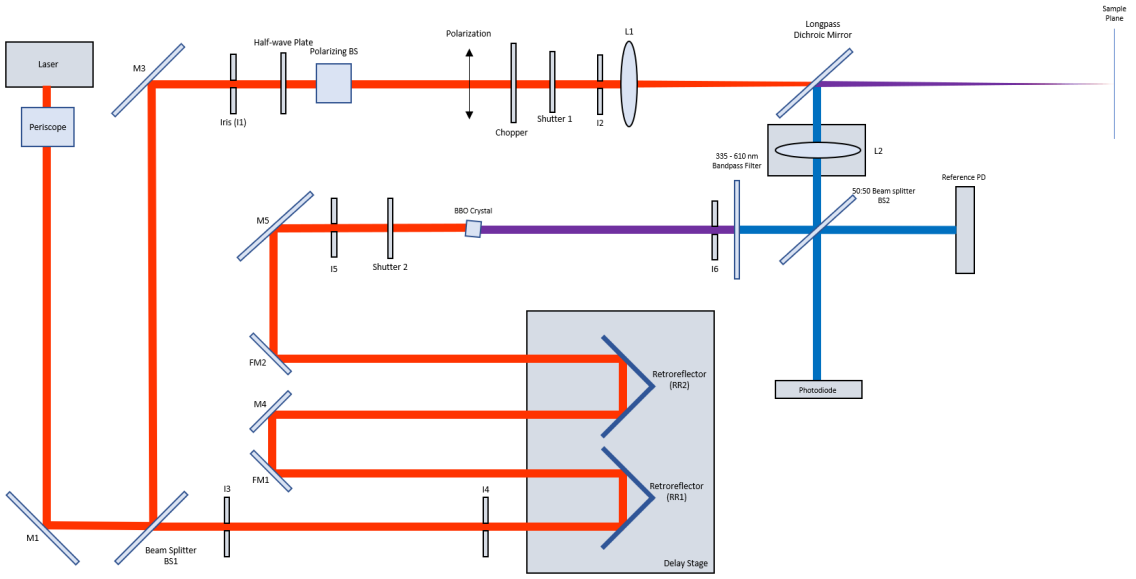

Figure 3.3: A schematic of the optical setup that is used when doing time-resolved experiments

rotate the crystal using the post until the highest power is observed. Then, maximize the power using the x and y adjustment screws on the crystal holder. Then rotate the crystal in the mount 1 degree in the CCW direction. Maximize the power and record it. Then rotate the crystal 2 degrees in the CW direction. Maximize the power again and record it. If the powers after rotating the crystals were both lower, then return the crystal to the original position and maximize the power output. If one power is higher and the other is lower, then keep rotating the crystal 1 degree and maximizing the power after every rotation. When the power drops after rotating, then the previous rotation is the correct rotation for proper phase matching. Figure 3.2 shows a schematic of the optics used as a basis of all second-harmonic experiments.

3.6 Alignment of Pump Probe Experiments

If the pump probe setup is used, then further alignment is necessary. Figure 3.3 shows a schematic of the setup with the delay stage. First, M2 has to be replaced with a a beam splitter (BS1). Then, the laser needs to be aligned with the driving axis of

the stage. The stage is moved to the lowest delay position. Then, a fluorescent paper (or another kind of detector) needs to be placed in front of the first retroreflector, and the position of the beam needs to be marked. The stage is then moved to the other end of the track. If the beam position did not change, then the laser is aligned with the first retroreflector. If the beam position moves, then M1 is used to move the beam towards the original position. The position of the beam is marked on the fluorescent paper once again. Move the stage to the lowest delay position, and if the beam position moves from the marked position, then M1 is used to move the beam away from the marked position. This is repeated until the beam does not drift when moving from one end of the stage to another. For fine tuning, the same process is done with the fluorescent paper after the retroreflector as far away from M1 as possible. This is accomplished by flipping the flip-mirror (FM1) and putting the paper after it. This process needs to be then repeated for the second retroreflector using M4. Once the first alignment was complete, I3 and I4 were placed for easier future alignment. To align for the irises, the same method used in section 3.3 were used with I3 and I4, and with M1 and one of the periscope mirrors. After the stage has been aligned, the beam needs to be aligned with I5 and I6. First, FM2 was used to center the beam on I5. Then, M5 was used to center the beam on I6. This was repeated until the beam was centered on both I5 and I6. The BBO crystal was aligned in the same way as in the previous section.

The pump laser was then aligned. This follows exactly section 3.3 and 3.4, except BS1 is used in lieu of M2. Care was taken so that the power of the beam does not reach the damage threshold of the dichroic mirror. Once the pump line was aligned, the probe needs to be aligned such that the focus position of L2 is the same as L1. To do this, first the horizontal and vertical position must match. Then lenses are removed, and a fluorescent paper is placed in the sample position. Then, the sample is moved as far back as possible. The dichroic mirror is then used to overlap both

beams. Then the sample is moved as close as possible to the mirrors. BS2 is used to overlap the beams. This is repeated until both beams are perfectly overlapped no matter what the sample position is. The location of focal point is then found. First, the focus is found with the pump beam as explained in section 3.3. Then, the focus is found using L2. Instead of moving the sample to change the focus position, the stage that L2 is on is moved back and forth instead.

CHAPTER IV

Desorption as a Mechanism for the Formation of Periodic Structures

The formation of laser induced periodic surface structures (LIPSS) in materials has long been a topic of much interest in optics and material science. Insulators, metals, and semiconductors all have the ability to form LIPSS [9]. There are two distinct types of LIPSS which are categorized as Low Spatial Frequency LIPSS (LSFL) and High Spatial Frequency LIPSS (HSFL). LSFL is characterized as having a period higher than half the wavelength of the incident light. LSFL is caused by selective ablation due to a modulating local intensity from by surface plasmon polariton (SPP) coupling [45] or Fresnel diffraction [117]. LSFL appears perpendicular to the laser polarization in metals and semiconductors when irradiating with energies above the band gap [35], but parallel to the laser polarization in semiconductors when the photon energy is lower than the band gap and in insulators [36]

HSFL is characterized by periods less than half of the wavelength of the incident light. Unlike the much better understood LSFL, the mechanism of HSFL formation is still under active research, and the literature suggests that the mechanism can differ with material and excitation parameters. Many HSFL formation mechanisms have been suggested such as selective ablation through second harmonic generation [41] , high frequency SPPs [59], Mie Scattering [118], and nanoplasma generation [56], and

point defect diffusion followed by relaxation[5, 8]. Previous work on the formation of HSFL in GaAs has been limited to irradiation with 780 nm light in air. This chapter will present a new mechanism where ultrafast point defect diffusion and laser desorption of atomic constituents lead to the formation of periodic structures below the original surface after irradiating in a vacuum environment, with both 780 nm light and 390 nm femtosecond light excitation.

4.1 Formation of HSFL with 390 nm Light

In order to investigate the effect of wavelength on the formation of HSFL in GaAs, 390 nm light was used to irradiate GaAs below the single shot melt threshold. The single shot melt and ablation threshold are dependent on the excitation wavelength [7]. To determine what the single shot ablation and melt thresholds with 390 nm light are, GaAs was irradiated at various powers. The radius of the ablated and melted regions were measured for each power, and a threshold fluence was calculated as outlined in Chapter 3.4. The radius of the ablated region was determined to be the distance between the center of the irradiated area and the wall of the crater. The radius of the melted area was determined to be the distance between the center of the irradiated area and region where the contrast of the GaAs visibly changes. A single shot ablation threshold of 0.1 J/cm^2 and a single shot melt threshold of 0.02 cm^2 was found by fitting Equation 3.2.

GaAs was then irradiated with 390 nm light below the melt threshold. First, irradiation was attempted in air (Figure 4.1a) at a fluence of 0.018 J/cm^2. While it is possible that a very shallow periodic structure appears, a 10-20 nm layer of oxide was also present which made it difficult to interpret the results. To eliminate the role of oxygen and pressure on the formation of HSFL, the experiment was repeated in a vacuum chamber. When GaAs was irradiated with 390 nm light in vacuum, HSFL with an average period of 65 nm and trenches 100 nm deep formed (Figure

4.1b). These features are considerably deeper and more distinct than the features observed when irradiating with 390 nm light in air. These features were found to emerge when the peak irradiation fluence was between 0.02 J/cm^2 and 0.016 J/cm^2, much closer to the single shot melt threshold than when irradiating with 780 nm light in air. Furthermore, while the ratio between the HSFL period observed when irradiating with 780 nm light and the incident wavelength is 4.3, the HSFL period to incident wavelength ratio for 390 nm light irradiation is 6, suggesting differences in the formation mechanisms for the HSFL.

Further evidence that the formation mechanism for HSFL formation with 390 nm light and 780 nm light is not the same became evident when cross section SEM was done (4.2). This revealed that the structures are all below the original surface. As outlined in Chapter 2.3.2, HSFL formation with 780 nm light in air occurs due to mass transport from the trenches to the peaks of the corrugation, with little to no material removal occurring. On the other hand, HSFL formed when irradiating with 390 nm light shows clear signs of material removal. It should also be noted that while deep HSFL is present down to 0.012 J/cm^2 when the peak fluence is between 0.016 J/cm^2 and 0.02 J/cm^2, deep HSFL is not present when the peak fluence is below 0.016 J/cm^2.

The evolution of the structures was investigated, as shown in Figure 4.3. At 500 irradiations, the island like structures are already aligned perpendicular to the polarization of the incident electric field. AFM done on these structures (Figure 4.4) reveals that they are below the original surface, indicating that the roughness necessary to excite SPPs is caused by desorption. The 2D Fast Fourier Transform (2DFFT) of the structures at this number of irradiations reveal that the period of the structures is 60 nm. At 1,000 irradiations the structures are strongly aligned perpendicular to the electric field, with the periodicity not changing significantly. At 10,000 irradiations, the structures are still aliened perpendicular to the incident

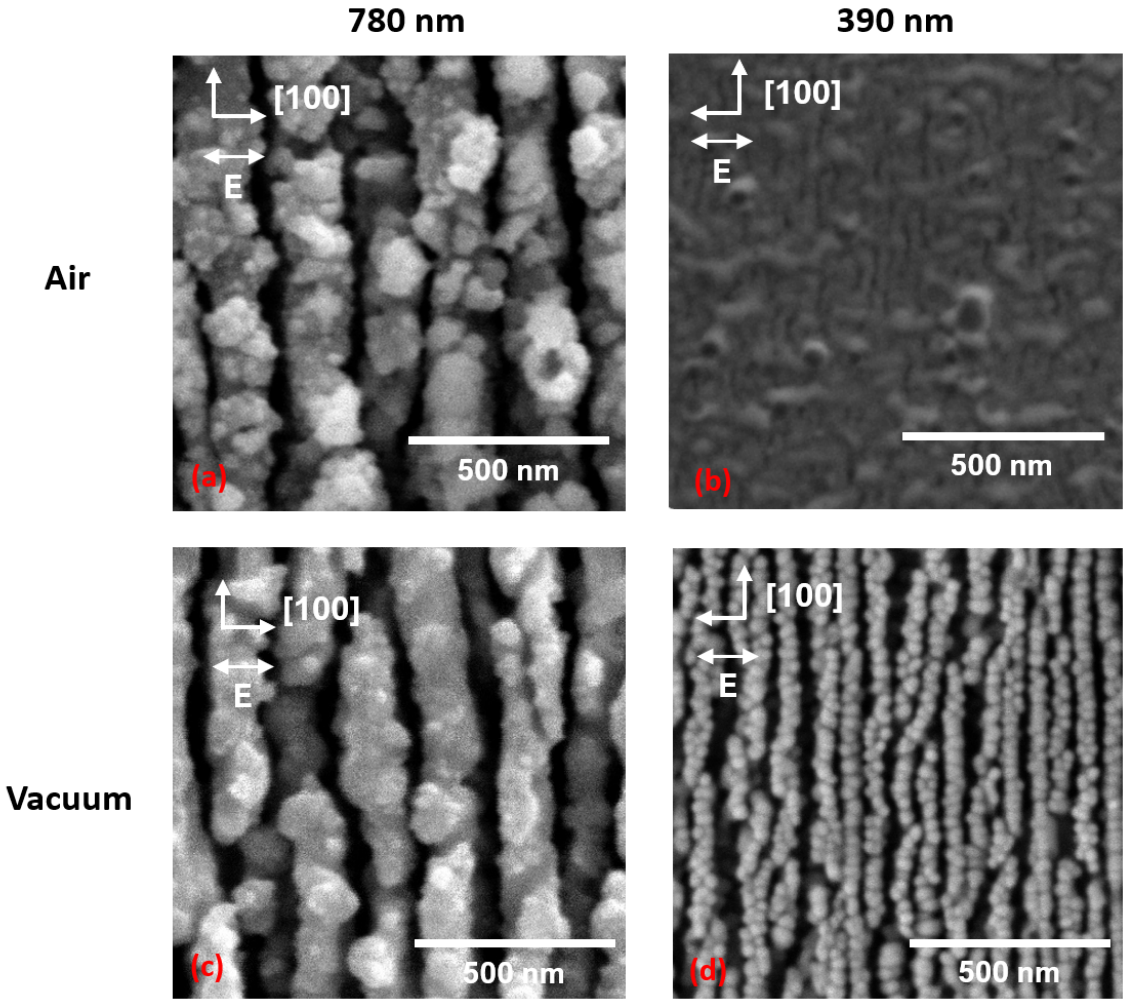

Figure 4.1: Comparison SEM images of GaAs irradiated with 780 nm light and 390 nm light at 10,000 irradiations in both air and vacuum environment. (a) HSFL formed with 780 nm light in vacuum at a fluence of 0.065 J/cm^2. The resulting structure has an average period of 180 nm and is both above and below the surface. (b) Oxide growth above the original surface formed with 390 nm irradiation in air at a fluence of 0.018 J/cm^2. (c) HSFL formed with 780 nm light in vacuum at a fluence of 0.065 J/cm^2. The structure has an average period of 180 nm and is completely below the original surface. (d) HSFL formed with 390 nm light at a fluence of 0.018 J/cm^2. The resulting structure has an average period of 65 nm and is below the original surface.

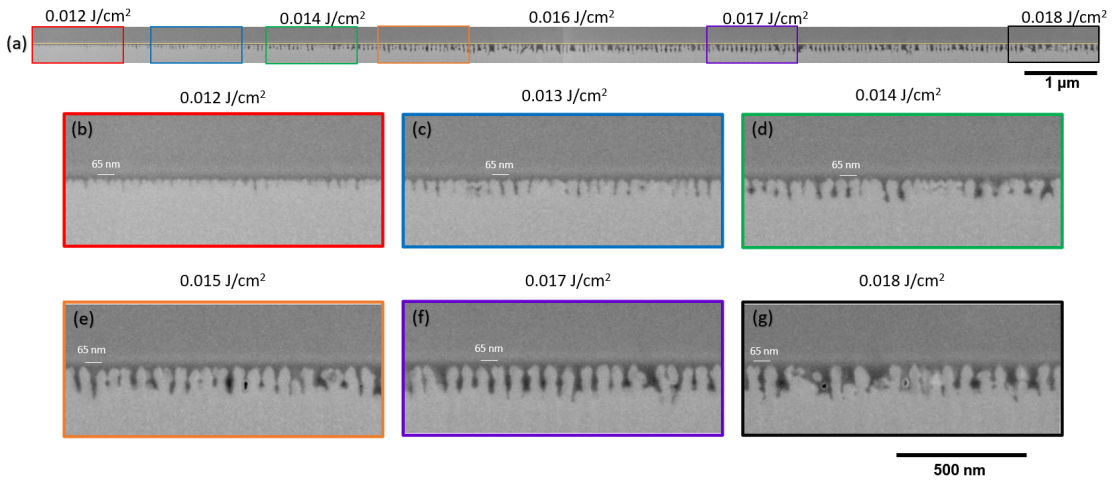

Figure 4.2: Cross Section SEM of GaAs irradiated with 390 nm light in vacuum. (a) is a composite of two different images of the same irradiation spot. (b-g) are enlarged images of the portions marked with colored rectangles at the specified local fluences. The yellow line represents the original surface. None of the corrugation is above the original surface. The average period between peaks is 65 nm. The peak-to-peak distance does not change significantly as a function of fluence, as shown by the 65 nm marker. The depth of the corrugation changes as a function of fluence, reaching a saturation depth of around 100 nm at 0.016 J/cm^2. At the higher fluences there is an increase in missing or misshaped "teeth" in the corrugation, as can be seen when comparing 4e or 4f with 4g.

electric field, but the trenches are much deeper. Further irradiation does not appear to change these structures significantly. One aspect of the evolution of this HSFL that should be noted is that unlike HSFL that forms on GaAs upon irradiation with 780 nm light, which undergoes multiple changes in the periodicity, the periodicity of this HSFL does not change significantly during irradiation. Furthermore, no bifurcation was observed, indicating that the spatial period was determined solely by the SPP-material interaction.

In GaAs, it has been shown that irradiation with light leads to desorption predominantly from surface defects [119, 120], which indicates that a surface point defect mechanism needs to be active during formation. Irradiation with laser pulses has been shown to create point defects in the material that diffuse to the surface [5, 6, 121], thus the initial irradiations serve mostly to create point defects in the surface. Interstitials become adatoms, step adatoms, or kink atoms, which have lower coordination numbers than surface atoms. Unlike in irradiation with 780 nm light in air, a large portion of these surface defects may be desorbed before they can coalesce into islands. Vacancies that diffuse to the surface lower the coordination number of neighboring atoms and coalesce into vacancy islands. These vacancy islands increase the density of step edges, as well as increase the roughness of the surface. A schematic of this mechanism is shown in Figure 4.5. The roughness caused by the formation of vacancy islands can couple with the incident light to excite SPPs. Forward and backwards traveling SPPs lead to the formation of a standing SPP wave, which localize the incident electric field. Desorption is enhanced in areas with higher fluences [122], forming a corrugation perpendicular to the laser polarization. Section 4.1.1 and 4.1.2 will discuss the excitation of the SPP's in more detail, as well as how well existing models predict the HSFL period we have observed.

If the proposed model is correct, where interstitials are being desorbed which leaves only the vacancies behind, then the resulting crystal structures would be expected

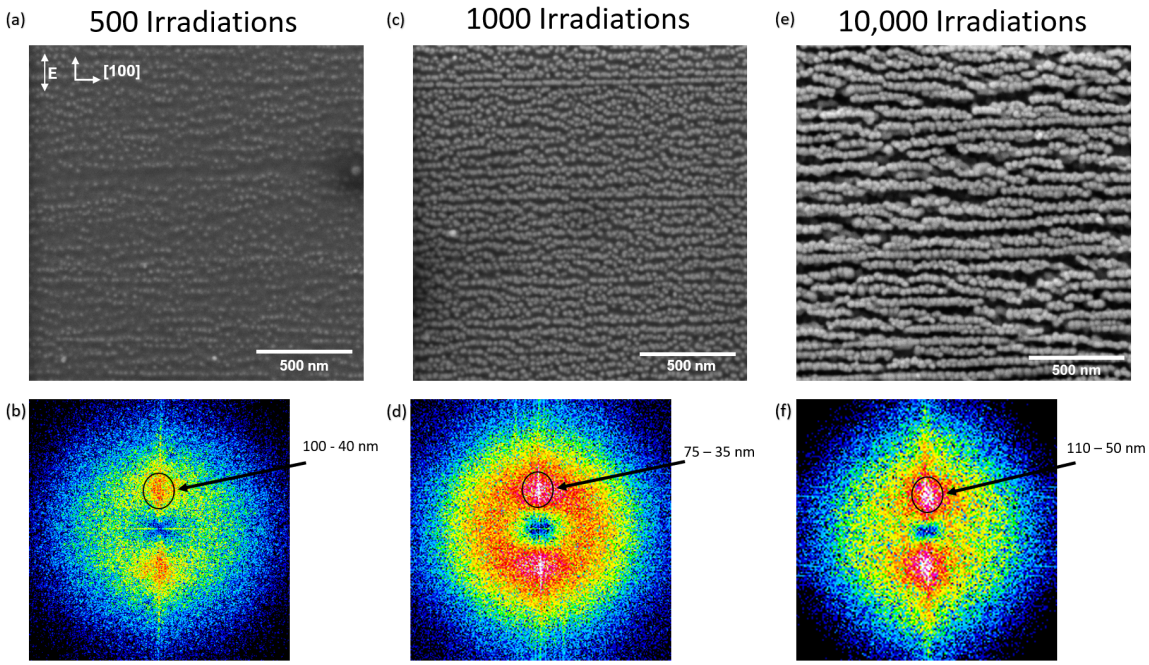

Figure 4.3: HSFL at different numbers of irradiations with 390 nm light in vacuum at a fluence of 0.018 J/cm^2. A 2-Dimensional Fourier transform (2DFT) using ImageJ was also calculated and shown. The individual peaks were determined by measuring the value of each pixel in the 2DFT images (a) At 500 irradiations there are already pit like structures in the surface and there is considerable alignment perpendicular to the polarization of light. (b) The 2DFT shows that there is a broad peak corresponding to 60 nm. (c) At 1000 irradiations the alignment is more evident, and the depth of the corrugations is increasing. (d) The 2DFT shows a broad peak between 35-75 nm with a maximum value at 55 nm. There is a red ring in the 2DFT image which indicates that the HSFL is not completely aligned perpendicular to polarization. (e) At 10,000 irradiations depth of the corrugation has further increased. (f) The 2DFT of the HSFL has a peak between 50-110 nm with a maximum value at 65 nm. The ring is not as prominent, which indicates that the features are highly aligned to be perpendicular to the laser polarization. Further desorption increases the depth of the trenches to about 100 nm. The 2DFT for this has a broader peak due to rows that have been fully desorbed. A low bandpass filter was applied to the images in order to remove noise before the 2DFT was calculated.

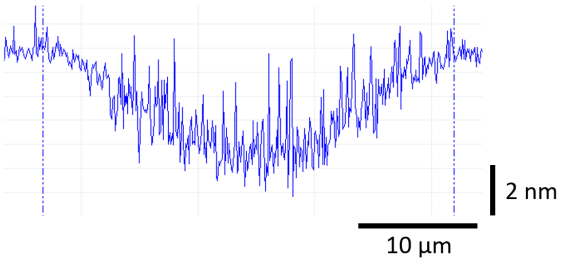

Figure 4.4: Crater that forms after 500 exposures with 390 nm light at a peak fluence of 0.018 J/cm^2. All the roughness is below the original surface.

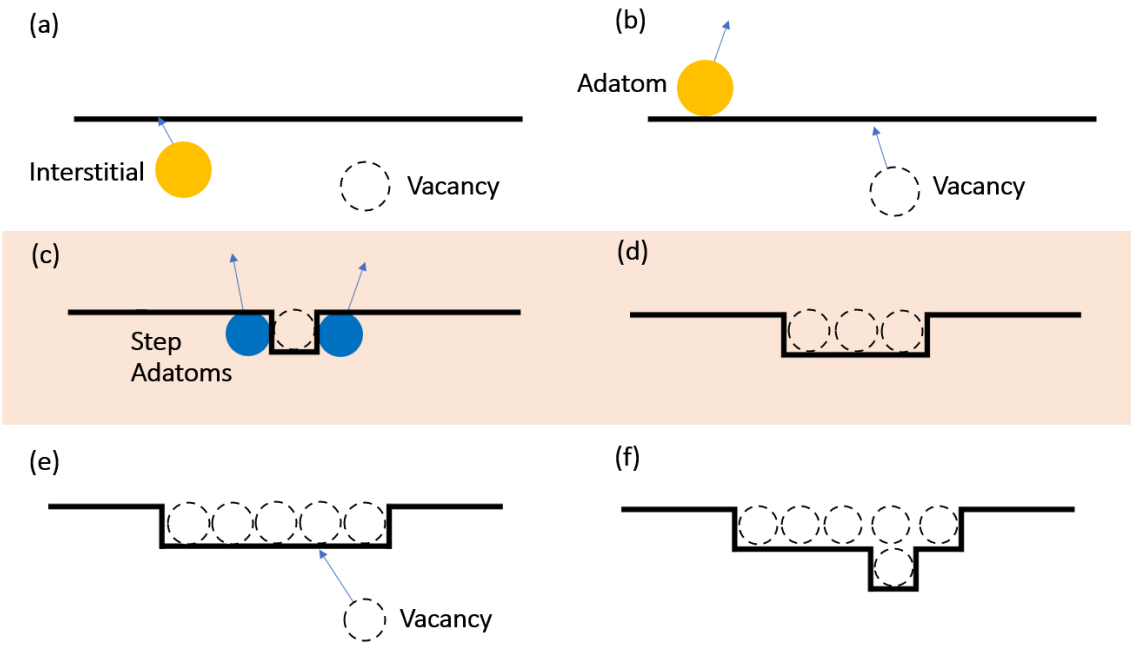

Figure 4.5: Schematic of the proposed desorption process. (a) The laser causes the formation of vacancies and interstitials in the bulk. Interstitials have higher mobility, thus they arrive at the surface before vacancies and become adatoms. (b) Adatoms are much more easily desorbed than surface atoms since they have a lower coordination number. (c) Vacancies diffuse to the surface which create step edges and increase the desorption probability of step adatoms. (d) The removal of step adatoms increases the size of the vacancy island which further increases the number of step adatoms that can be desorbed. (e) Point defect diffusion is still occurring, with adatoms being removed and vacancies diffusing to the surface, further increasing the step edge density (f) Vacancies that arrive at the bottom of the vacancy island increase the depth of the vacancy island. This process continues happening until the vacancy islands become deep enough for the excitation of surface plasmon polaritons.

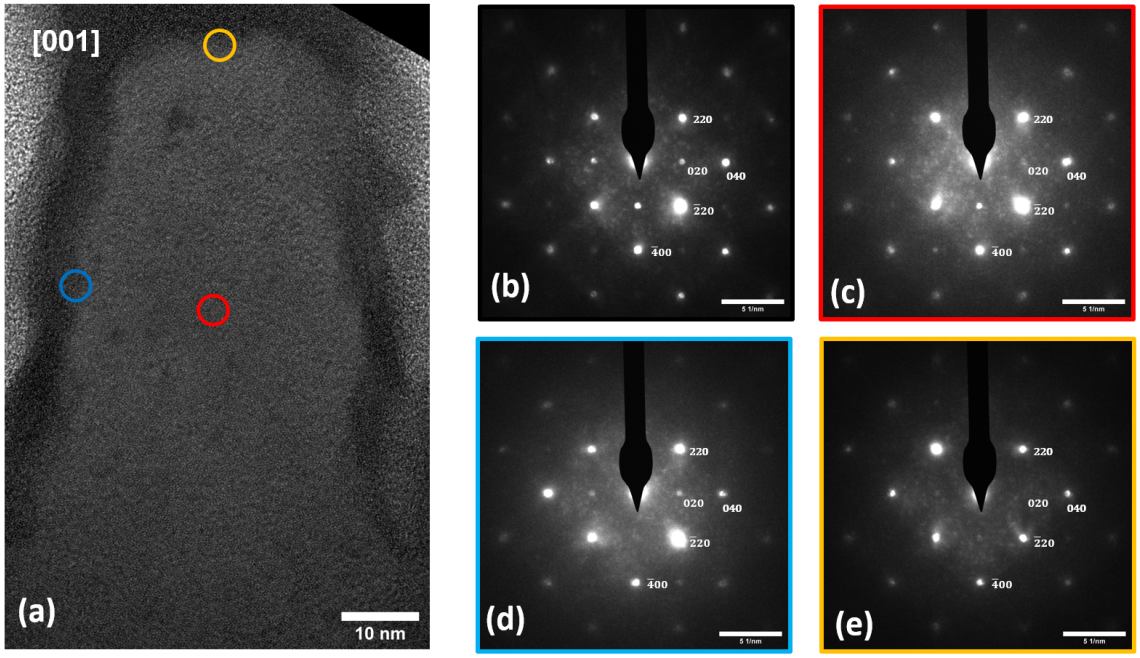

Figure 4.6: (a) Transmission Electron Microscopy of an individual corrugation formed after 10,000 irradiations with 390 nm light at a fluence of 0.018 J/cm^2. (b) Nanobeam Electron Beam Diffraction (NBED) pattern of the GaAs bulk, taken 200 nm below the corrugated structure. it has a clear single crystal diffraction pattern of the [001] zone axis. (c) NBED pattern of the middle of the corrugation. The pattern is still that of a single crystal. The hazy area around the middle is due to surface defects that arise during the thinning process, oxide growth due to exposure of the atmosphere, or carbon growth due to exposure to high energy electrons. (d) NBED diffraction of the sidewall and (e) NBED diffraction of the top still have a single crystal pattern.

to be completely single crystal. To determine this, TEM and Nanobeam Electron Diffraction (NBED) of the corrugations was done, as shown in Figure 4.6. Figure 4.6b shows the NBED pattern for bulk GaAs along the [110] zone axis. Figure 4.6 (c), (d), (e) show the NBED pattern for the corrugated structure in the center, sidewall, top, respectively. As it can be seen, the single crystal diffraction pattern is still present even extremely close to the sidewalls, showing that the structure is completely single crystal, which is evidence in support of our point defect-desorption model.

4.1.1 Determining the Dielectric Function During Excitation

One question that still has not been answered is whether SPPs can be excited on the GaAs surface. As it was discussed in section 2.4, in order for SPPs to be excited on the air/material interface, the real part of the dielectric function needs to be at least -1. Excitation with an ultrafast laser can create a dense electron-hole plasma during irradiation that can cause the material's dielectric function to become more metal-like [1]. This electron hole plasma can be described using the Drude model, resulting in an equation for the excited dielectric function:

$$\varepsilon_{exc} = \varepsilon - \frac{N_e e^2}{\epsilon_0 m_{opt} m_e \omega^2} \frac{1}{1 + i\frac{\Gamma}{\omega}} \tag{4.1}$$

Where ε is the ground state dielectric function, N_e is the excited carrier density, e is the elementary charge, ε_0 is the permittivity of vacuum, m_{opt} is the optical effective mass, m_e is the mass of an electron, and Γ is the collision frequency of electrons in the plasma. In order to calculate the excited dielectric function, first the carrier density needs to be calculated. For semiconductors, excitation by ultrafast pulses is caused by both linear and non-linear absorption. The resulting excited carrier density can then be described by the following differential equation:

$$\frac{\partial N(z,t)}{\partial t} = \left(\alpha_0 + \frac{1}{2}\beta_0 I(z,t)\right) \frac{I(z,t)}{\hbar\omega} \tag{4.2}$$

Where α_0 describes the linear inter-band absorption, and β_0 describes the non-linear inter-band absorption. Assuming a Gaussian temporal profile $I = I_0 e^{-(t/t_0)^2}$, using the relationship between peak intensity and peak fluence, $I_0 = \sqrt{\pi} t_0 F_0$, and considering the reflection of the incident light on the boundary, the above equation can be integrated in time which results in:

$$N_e = \frac{F_0(1-R)}{\hbar\omega} \left(\alpha_0 + \frac{\beta_0}{2\sqrt{2\pi}t_0} F_0(1-R)\right) \tag{4.3}$$

Which is the equation for the excited carrier density at the near surface, where R is the reflectivity of the material for the incident light, t_0 is the temporal duration of the pulse, and F_0 is the peak fluence. For 390 nm light in GaAs, excitation occurs in the E_1 peak of the dielectric function, which corresponds to the L-valley, which is an area in the band structure of GaAs with parallel lines where linear absorption is dominant. β_0 can then be approximated to be nearly zero compared to α_0, which results in a simplified equation:

$$N_e = \frac{F_0(1-R)\alpha_0}{\hbar\omega} \tag{4.4}$$

Using the values for excitation with 390 nm light ($\alpha_0 = 7.2885 \times 10^5\ cm^{-1}$, $R = 0.47$, $\hbar\omega = 3.18\ eV$ at a peak fluence of 0.018 J/cm^2, a value of $1.32 \times 10^{22}\ cm^{-3}$. The calculated carrier density represents roughly 7.5% of total number of valence electrons ($1.77 \times 10^{23}\ cm^{-3}$), which is consistent with ab-initio adiabatic calculations done on GaAs in this excitation regime. The resulting excited dielectric function for GaAs, along with the room temperature unexcited dielectric function, are plotted in Figure 4.7. As it can be observed, the dielectric function for 390 nm light at this level of excitation is sufficiently metal like ($\varepsilon = -8.30 + 23.26i$), which indicates that SPPs can be excited in the air/GaAs interface.

It should be noted that while this calculation results in a reasonable value for the dielectric function, there are a few limitations to this model that need to be considered. First, the effective mass for the L-valley was calculated using the values for electrons in unexcited GaAs. Studies on silicon have shown that during excitation, the optical effective mass does not remain constant [1], which means that the effective mass used might be an underestimation, which would lead to a more negative real part. Second, with excitation at the L-valley, the excited electrons are not in a Fermi-Dirac distribution, which is an assumption of the Drude model. Nonetheless, this model has been used to adequately predict the SPP wavelengths during the formation of HSFL

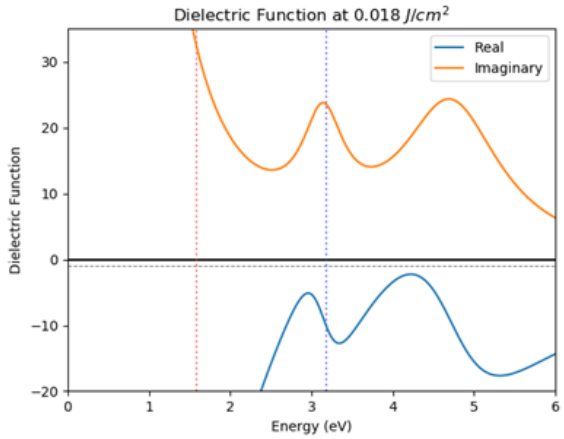

Figure 4.7: The excited dielectric function of GaAs irradiated with a 390 nm, 150 fs pulse at a fluence of 0.018 J/cm^2. The horizontal black dashed line represents the threshold for the excitation of Surface Plasmon Polaritons (SPP). The red and blue dashed line represent the energies corresponding 780 nm light and 390 nm light, respectively. Both the real and imaginary part of the dielectric function resemble that of a metal. The real part of the dielectric function is sufficiently negative at 3.18 eV in order to excite SPPs.

formation with 780 nm light [8], thus here is still significant value in this result.

4.1.2 Existing HSFL Period Models

Now that a value for the excited dielectric function of GaAs has been determined, models found in the literature can be applied to determine whether HSFL with the observed periodicity are predicted. The first and simplest model is that of the periodicity caused by an SPP excited in the air/GaAs interface. The wavelength of this SPP is given by solving for λ_{spp} in equation 2.11:

$$\lambda_{spp} = \lambda \left(\frac{1 + \varepsilon^r_{exc}}{\varepsilon^r_{exc}} \right)^{1/2} \tag{4.5}$$

Where λ is the wavelength of the incident light, and ε^r_{exc} is the real part of the excited dielectric function. This results in an SPP wavelength of 368 nm. Since the energy of a standing SPP is localized at half the period of the SPP wavelength[123], this SPP wavelength would result in corrugation with a period of 182 nm, which was

not observed during irradiation. This indicates that the corrugation formed are not caused by an SPP propagating on a single interface, thus more complex models need to be applied.

Another possible model is one where the SPP is traveling on an oxide and excited GaAs interface. As seen by the TEM (Figure 4.6, a 10 nm oxide grows during irradiation, which is significantly thick enough to perturb the SPP. Using $\varepsilon = 3.85$ for the oxide film [124] in equation 2.11 results in an SPP wavelength of $\lambda_{spp} = 146$, which predicts an HSFL wavelength of 73 nm. While this is very close to the observed wavelength, and thus a good candidate for the model, the oxide layer would be expected to stop desorption from occurring. This implies that the oxide layer was not present during irradiation, and thus grew after the sample was exposed to atmosphere, otherwise removal would not be expected to occur. It is also possible that the growth of this oxide is what would stop further desorption from occurring, but this still indicates that the oxide layer would grow after the corrugation already formed. All this indicates that the oxide layer is most likely not the origin of the observed periodicity.

During excitation, GaAs is only metal-like in a very thin region (¡14 nm) near the surface. As discussed in section 2.5, treating this region as a thin metal slab with SPPs traveling at both the Air/Excited and Excited/Unexcited interface has had reasonable success in describing how SPP propagation lead to corrugated surfaces. Applying the thin film plasmonic model [77] yields an SPP wavelength of $\lambda_{spp} = 130$ nm. Dividing by half to take into account that the localization of the energy for a standing wave is at half the wavelength, this model would predict a corrugated surface with a period of 65 nm, which is consistent with our results. While the result of this model matches the experimental results, there are a few limitations of the model that must be discussed. While with our excitation parameters, the air/excited interface can easily support an SPP, the generalized form of equation 2.9 indicates that

the excited/unexcited interface cannot support a very long lived SPP [77], since the constraint $Re(\varepsilon_{excited}) < -Re(\varepsilon_{GaAs})$ is not met. Furthermore, a dielectric slab is not a very accurate representation of the actual excitation schema since there is no sharp interface between excited and unexcited material. Thus, while this model's solution matches the experimental results, a more thorough analysis of SPP propagation in the volume where the real part is sufficiently negative needs to be done.

4.2 Desorption with 780 nm Light

Since desorption was activated during irradiation with 390 nm light only when the sample was put in vacuum, irradiation with 780 nm light in vacuum needs to be investigated to determine whether desorption is wavelength dependent or pressure dependent. A GaAs wafer was cleaned as outlined in Chapter 2 and put into vacuum prior to irradiation. The sample was then irradiated at a fluence of 0.065 J/cm^2, which is the same fluence in which HSFL has been observed to form in GaAs when irradiated with 780 nm light[5]. The resulting morphology after 1000 irradiations is shown in Figure 4.8. At fluences and number of exposures in which HSFL is expected to fully emerge, HSFL is not present throughout the whole irradiated area. The only signs of morphological changes are a change in the contrast, and scattered regions where HSFL with a period of 350 nm are found. AFM done on these trenches confirms that they are below the original surface, indicating that desorption is the most likely mechanism for their formation. No evidence of the shallow HSFL that is the precursor to the 355 HSF was observed, which could be due to desorption inhibiting the formation of the initial islands coalesce.

After 1000 more irradiations (Figure 4.9), a periodic structure begins to form. While this periodic structure has a period of 350 nm, similar to that which is observed when irradiating in air, it does not appear to have the same morphology. The structures observed after irradiating in air have thin trenches, as well as the surface

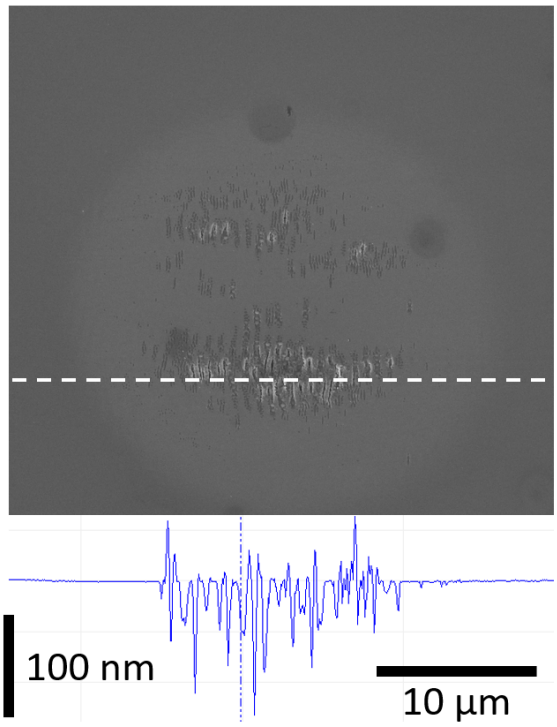

Figure 4.8: SEM and AFM of the GaAs morphology that forms after 1000 irradiations with 780 nm light at a peak fluence 0.065 J/cm^2 in vacuum. The few scattered structures have a periodicity of 350 nm. At this same number of irradiations with the same fluence in air, the HSFL has fully developed. All of the structures are below the original surface.

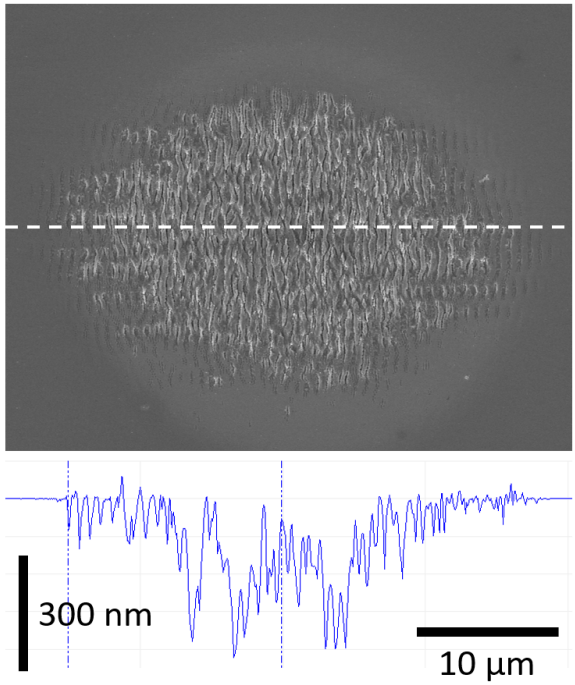

Figure 4.9: SEM and AFM of the GaAs morphology that forms after 2000 irradiations with 780 nm light at a peak fluence 0.065 J/cm^2 in vacuum. The structures have a periodicity of 350 nm. The HSFL present does not have the same morphology as the 355 nm HSFL that is observed when irradiating in air. Most of the structures are below the original surface.

profile above the surface is roughly flat a distance 100 nm from the peak, and the depth decreases sharply from the peak to the bottom of the trenches. On the other hand, the structures observed when irradiating in vacuum do not have flat peaks, and instead the surface profile drops smoothly from the peak to the bottom of the trench. Furthermore, AFM done on these structures reveal that they are all below the original surface.

After 8,000 more irradiations, the periodic surface structure undergoes a change in the periodicity (Figure 4.10). The periodicity changes from 350 to 180 nm, which is consistent with the change in periodicity observed when irradiating in air. The periodic structure observed after 10,000 irradiations in vacuum is nearly indistinguishable to the final stage of the HSFL observed after 1000 irradiations in air. It has both a similar periodicity, as well as similar structure. One crucial difference is

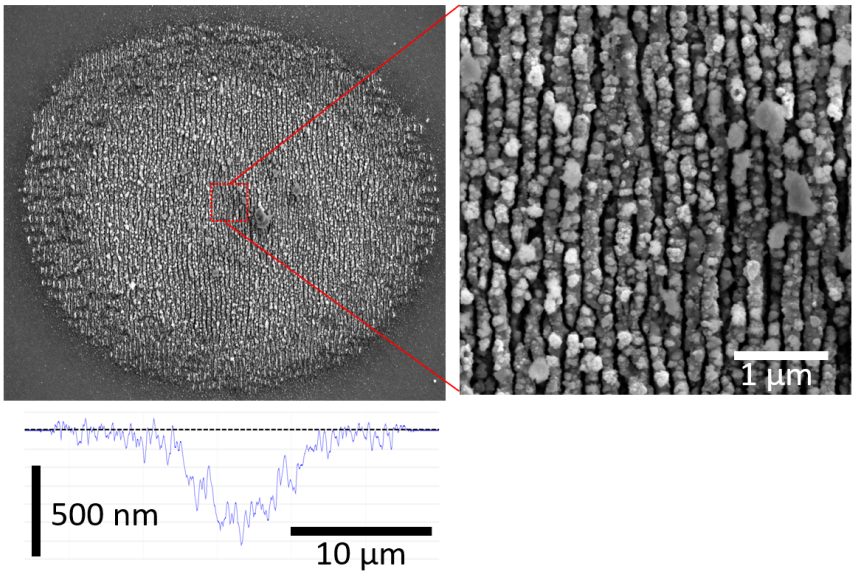

Figure 4.10: SEM and AFM of the GaAs morphology that forms after 10,000 irradiations with 780 nm light at a peak fluence 0.065 J/cm^2 in vacuum. The structures have a periodicity of 180 nm. The HSFL present has a strikingly similar morphology to the kind that is found when irradiating in air. Most of the structures are below the original surface.

that the corrugation shown in Figure 4.10 is completely below the original surface, as confirmed by AFM. The similar appearance indicates that the final morphological change during irradiation, stress induced bifurcation, occurs in both air and vacuum.

While both irradiation in air and in vacuum eventually result in extremely similar corrugation, the pathway to achieve said corrugations differs greatly. The fact that the 165 nm shallow grating does not form is indicative that desorption is causing the removal of adatoms before they can coalesce into islands. Eventually, as vacancies diffuse to the surface, desorption causes the removal of atoms near the vacancies, forming the crater observed in the AFM. The surface at the bottom of the crater eventually becomes sufficiently rough for the excitation of SPPs to occur, which causes inhomogeneous desorption. At this point, desorption is mediated by the SPPs, which causes the corrugated surface below the original surface that is observed. The fact that this periodic structure is formed by desorption, not the material reconfiguration process, can explain the difference in the shapes of both periodic structures. Since

laser desorption has been shown to be highly fluence dependent [87], the smoother surface profile can be explained by the fact that small changes in the local fluence have a large effect on the desorption rate. In the last stage, while desorption could still be occurring, the similarity of the HSFL in air and vacuum indicate that it occurs due to stress instability in the corrugated volume due to the formation of point defects. Thus, while the beginning of the formation of HSFL with 780 nm light in vacuum is caused by desorption of atoms, the last stage is not believed to differ from the formation of HSFL in air.

The experiments in vacuum with 780 nm light make it clear that it is vacuum, not wavelength, that activates the desorption process. The reason why air seems to inhibit the desorption process has not been fully resolved, specifically, if pressure or oxygen content inhibit desorption. Pressure can inhibit the desorption process by increasing the ability for desorbed atoms to be adsorbed back to the surface. The mean free path of an atom in vacuum is orders of magnitude larger in vacuum than in free air, thus in air, desorbed particles could collide with molecules in the atmosphere and be redeposited. Oxygen, on the other hand, can bond with the dangling bonds in the surface, which decreases the surface energy thus decreasing the likelihood that atoms will be desorbed. A thin layer of oxide that could grow during irradiation would also serve as a barrier that desorbed atoms have to cross in order to completely delocalize from the surface, increasing the possibility of re-adsorption.

In summary, this chapter has shown a new type of HSFL that emerges when irradiating with ultrashort UV laser pulses driven by surface defect formation and desorption of atomic constituents, as well as showed that the irradiation environment plays an important role in the mechanism of HSFL formation. The irradiation with 780 nm light in air showed that the previously reported corrugated structure present both above and below the surface with an average period of 180 ± 20 nm was able to be reproduced [5, 8]. However, when repeating the experiment in vacuum, a structure

with the same periodicity emerged, but was completely below the original surface. Furthermore, HSFL was shown to form at a lower number of irradiations in air compared to vacuum. To investigate the effect of wavelength on the formation of HSFL, GaAs was also irradiated with 390 nm light in air at a fluence just below the melt threshold, which showed no periodic surface structure was present. Instead, chunks of oxide grew above a network like structure. The experiment was also repeated in vacuum, where HSFL with an average period of 65 nm and 100 nm deep trenches formed. HSFL with a sub 100 nm spatial period had previously not been observed in GaAs. The structures were completely below the original surface, suggesting that the formation of HSFL with 390 nm light in vacuum is driven by desorption. Using the thin film plasmonic model, it was shown that the period of the HSFL was consistent with desorption localized at half the SPP wavelength.

CHAPTER V

Excited State Enhanced Diffusion

One aspect of ultrafast laser material interactions that has not been discussed in previous work is the rate at which these morphological changes are occurring. In this chapter, the formation of HSFL with 780 nm light first discussed by Abere et. al.[5] will be revisited to determine whether the growth rates observed can be explained using thermal models, or whether it is necessary to invoke a non-thermal enhancement by the laser. If it is found that the laser has a strong non-thermal enhancement to the diffusion, a similar treatment will be taken with the HSFL formation discussed in the previous chapter.

5.1 Growth Rate of HSFL Formation with 780 nm Light

To determine whether there is a non-thermal enhancement of the diffusion coefficient during the growth of the HSFL that forms upon irradiation with 780 nm light in air, the diffusion coefficient of the atoms needs to be estimated. Calculating the diffusion coefficient presents a few challenges. The first challenge is that the HSFL does not grow uniformly during irradiation, but instead has distinct stages, as outlined in section 2.3.2. This means that doing a post-mortem analysis of the HSFL can, at best, result in an average diffusion coefficient. Nonetheless, for the purpose of this discussion, the average diffusion coefficient should be sufficient, since mainly

order of magnitude will be considered. The other challenge is that assumptions need to be made on what the temperature of the material is, although these assumptions will always be made to err on the side of underestimating the diffusion coefficient. For the growth of HSFL with 780 nm light, due to the fact that gallium droplets are not observed, the temperature does not exceed 930 K [125], thus a temperature of 930 K will be used for all experiments.

While there have been significant studies on the growth of HSFL on GaAs [5, 8], no studies on whether the growth occurred during or after excitation have been done. To determine this, the reflectivity of the material as a function of shot number was measured, as shown in figure 5.1. The data in Figure 5.1 was gathered by first pumping the sample at a peak fluence of 0.065 J/cm^2, then probing with a less intense probe at an arbitrary delay. The experiment was repeated 10 times and averaged to improve the signal to noise ratio. While no actual information on the mobility of the atoms could be extracted due to the small magnitude of the changes in reflectivity between laser pulses, this experiment reveals that all the growth occurs during the time the material was being actively irradiated. In the case for the growth of HSFL with 780 nm light, the growth occurred in the span of one second. While it appears that the growth occurs mostly within only around 400 pulses, this might not be necessarily accurate. Since the experiment only measures reflectivity, it is possible that the initial growth was not properly reflected in the data because the structures were not sufficiently large to interact with the incident laser. Furthermore, when the corrugated structure forms and the light is scattered significantly, increases in the growth might have a smaller effect on the periodicity. Lastly, the pump and probe pulse used were Gaussian, and while there was an effort to make the pump sufficiently large such that the probe focus was fully within the irradiated area, the effect of different growth rates at different fluences cannot be easily extracted. Thus, the only meaningful data that can be extracted from this is that growth occurs while

the material is being actively irradiated. While it takes about one second for these structures to form, the material is not thermally or electronically active throughout the 1 millisecond between pulses. Within 10 ns, recombination leads to a relaxation of a large amount of the excited carriers to the ground state and thermal diffusion leads to significant cooling of the material [17]. Thus, any diffusion in the material occurs only during the first 10 ns after excitation.

To determine whether enhanced diffusion is observed, Fick's first law will be used to estimate a diffusion coefficient:

$$J_x = -D\frac{\partial C}{\partial x} \tag{5.1}$$

Where J_x is the atomic flux and is dependent on the gradient of the concentration of defects and D is the diffusion coefficient. Assuming that the concentration of point defects is changing linearly, Fick's first law can be approximated to:

$$J_x = -D\frac{\Delta C}{\Delta x} \tag{5.2}$$

where ΔC is the change of the concentration, and Δx is the distance in which the concentration changes by an amount ΔC.

To calculate the diffusion coefficient observed during the growth of the HSFL, the atomic flux across the original surface needs to be calculated. It will be assumed that the atomic flux of the interstitials is equal to the number of atoms that are in the corrugated volume above the original surface divided by the active diffusion time (10 ns). Using Figure 5.2, the total volume that is above the original surface is estimated. To calculate the number of atoms, this volume is then multiplied by the atomic density of GaAs, 44.2 nm^{-3}. The number of atoms above a 180 x 180 nm area after 1000 irradiations is then calculated to be 4.22×10^7 atoms. This is then converted to atoms per unit area by dividing by the area (180 x 180 nm^2) which

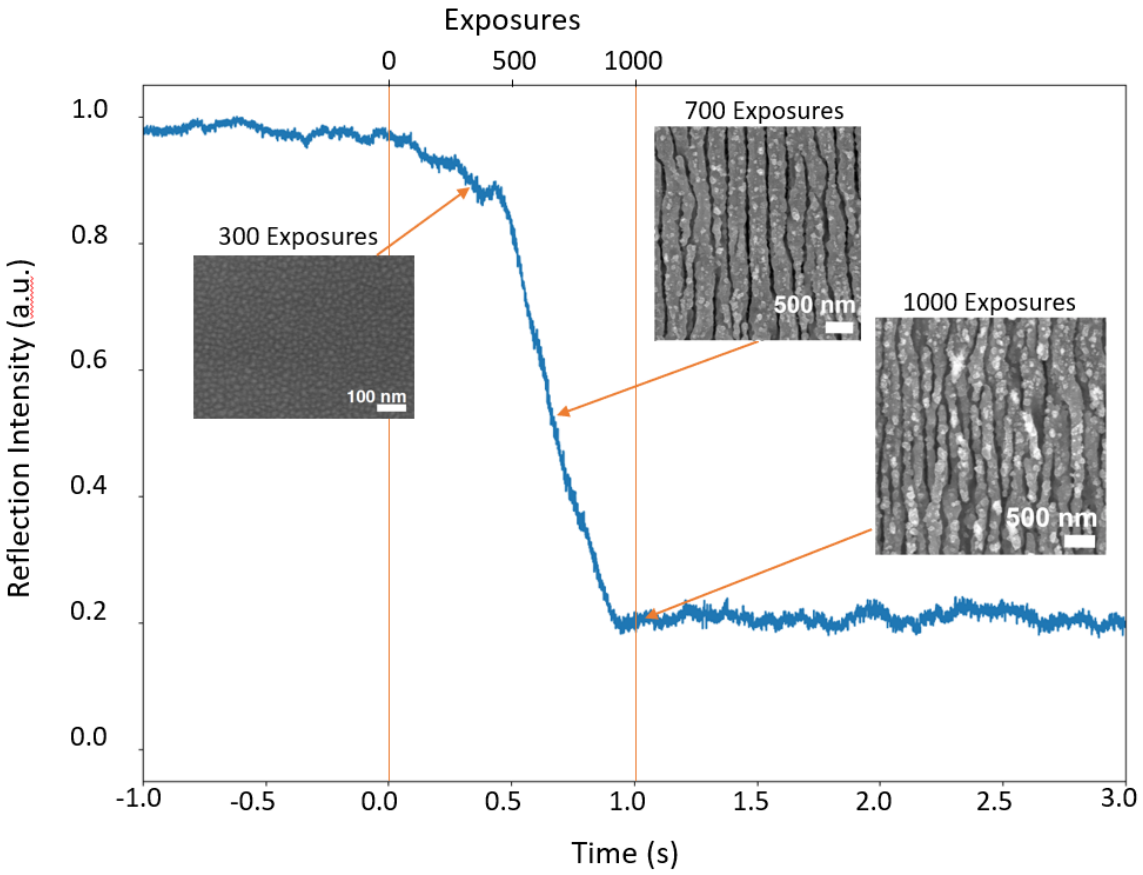

Figure 5.1: Reflectivity measurements of HSFL formation upon irradiation with 780 nm light at a fluence of 0.07 J/cm^2. At first, the change in the reflectivity is slow while the formation of the islands and shallow grating occur. When the 355 nm HSFL begins forming, the reflectivity changes at a much rapid rate. Bifurcation appears to occur at a similar rate as the formation of 355 nm HSFL. After the laser is turned off, the reflectivity of the HSFL does not change, indicating that the growth only occurs during excitation. Insets adapted from Michael J Abere. *From Point Defects to Ripples: Ultrafast Laser Induced High Spatial Frequency Laser Induced Periodic Surface Structures*. PhD thesis, University of Michigan, 2015

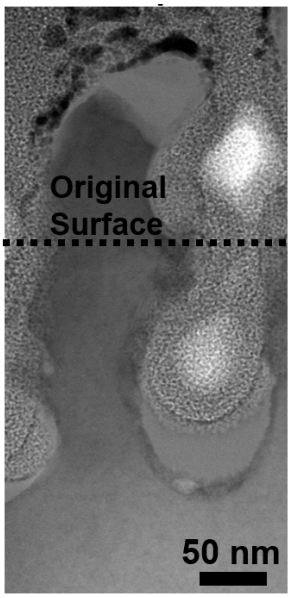

Figure 5.2: Cross Section TEM of GaAs Irradiated with 780 nm light in air. Mass transport from the trench to the original surface occurs throughout 1000 irradiations. The distance from the center of mass of the trench and the corrugation above the surface is 150 nm. Adapted from Michael J. Abere, Ben Torralva, and Steven M. Yalisove. Periodic surface structure bifurcation induced by ultrafast laser generated point defect diffusion in GaAs. *Appl. Phys. Lett.*, 108(15):153110, April 2016

results in 1.302×10^3 atoms/nm^2. This growth occurs during 1000 irradiations, thus assuming that the growth occurs uniformly as a function of shot number leads to 1.3 atoms/nm^2/shot. If the same active diffusion time assumption is made, then a growth rate of 1.3×10^8 atoms/nm^2/s (1.3×10^{22} atoms/cm^2/s) is calculated. To put this number in perspective, this is the equivalent of growing 10^8 monolayers per second.

To calculate the diffusion coefficient using Equation 5.2, the concentration of point defects needs to be estimated. During irradiation with 780 nm at a fluence of 0.065 J/cm^2, a minimum of 1 out of 1000 atoms need to become interstitials in order to account for the observed rate[1]. This means that the interstitial concentration is

[1]This was calculated by taking the number of atoms that arrive to the surface after irradiation and dividing by the extinction length of the laser, which is where the highest concentration of defects are found. Thus while the actual number of defects formed might be higher, this is the number of defects created assuming that they all arrive at the surface

roughly C = 0.0442 nm^{-3} (4.2×10^{19} cm^{-3}). If it is assumed that the bottom of the trench is the location with the highest concentration of interstitials, then as the trenches get deeper the distance interstitials need to travel increases. The difference between the minimum and maximum trench depth is only an order of magnitude (from 10 nm to 100 nm), thus it will be approximated to 55 nm in order to calculate an average atom flux of the HSFL formation process. Using Equation 5.2, the diffusion coefficient is calculated to be $1.61 \times 10^{-3} cm^2/s$.

To determine whether enhanced diffusion occurred throughout the formation process, and not only during the bifurcation process, the diffusion coefficient at the earlier number of irradiations is calculated. After 350 irradiations, the only structures present are 20 nm diameter, 0.5-0.75 nm tall islands [8, 126]. The distance from the center of the islands to the center of the nearest island is roughly 50 nm. To calculate the rate, a similar approach as previously was taken, treating the islands as cylindrical islands. The volume of an island with a diameter of 20 nm and a height of 0.62 nm was found. This was then converted to number of atoms by multiplying by the atomic density. Since the atoms that make up the islands could come up from anywhere and not just the area below the island, then to find the flux the total number of atoms was divided by an area with a size of 30x30 nm^2. Assuming that diffusion is active for 10 ns, this leads to a flux of 0.027 atoms/nm^2/shot, or 2.73×10^6 $atoms/nm^2/s$. To calculate a diffusion coefficient, it was again assumed that 1 out of 1000 atoms became interstitials. Since the highest concentration of interstitials is expected to be close to the surface, it was assumed that the change in the concentration occurred over 1 nm. Using Equation 5.2, it was then found that the diffusion coefficient was 6.5×10^{-7} cm^2/s. This diffusion coefficient, as well as the flux of atoms, is notably smaller than that which was previously calculated. One possible reason for this discrepancy is that surface diffusion, which is significantly faster than bulk diffusion [127], is playing a role once the corrugated structures form.

Another possibility is that the concentration of point defects does not increase linearly per irradiation. As the structures form, the underlying material becomes more defective and stressed, thus the probability of creating point defect increases after every irradiation. The rapid change in the reflectivity after 500 exposures in figure 5.1 could be evidence of this mechanism.

Next, we need to compare how this diffusion coefficient compares to values in the literature for the self-diffusion of Ga. The equation used to calculate the diffusion coefficient is:

$$D = D_0 e^{-\frac{E_a}{k_b T}} \tag{5.3}$$

Where D_0 is the diffusion prefactor, E_a is the activation energy, k_b is the Boltzman constant, and T is the temperature of the material. To again err on the side of caution, it will be assumed that the material is at a constant temperature of 930 K for 10 μs after excitation. This is a conservative assumption that would overestimate the diffusion coefficient. The diffusion coefficient for GaAs depends on the diffusive pathway [106]. In GaAs it has been shown that self diffusion is vacancy mediated and occurs either through nearest neighbor hops or second nearest neighbor hops. Diffusion to the peaks is most likely mediated by interstitial diffusion. This is because during the growth, point defect generation is expected to occur mostly in the trenches, thus there are not enough point defects generated in the volume above the original surface. Nonetheless, the most appropriate diffusion coefficient for vacancy mediated diffusion, interstitial mediated diffusion, and surface diffusion will be calculated for comparison. The values found in the literature, as well as the estimated diffusion coefficient, are summarized in Table 5.1.

The diffusion coefficients found in the literature are all significantly lower than those calculated for the formation of both the HSFL and the nano-islands. Even assuming that the material is brought very close to the melt temperature (1512 K), none

Mechanism	D_0 (cm^2/s)	E_a (eV)	D(930 K)	D(1500 K)
Self-Interstitial	6.05	4.89	1.91×10^{-26}	2.25×10^{-16}
Vacancy	4×10^{-5}	2.6	$3,25 \times 10^{-19}$	7.35×10^{-14}
Vacancy (FP)	1×10^{7}	5.6	4.48×10^{-24}	1.53×10^{-12}
Surface	1.113	1.31	8.85×10^{-8}	4.41×10^{-5}
Estimated (1k)	N/A	N/A	1.61×10^{-3}	N/A
Estimated (350)	N/A	N/A	6.5×10^{-7}	N/A

Table 5.1: Calculated diffusion coefficients for the various values found in the literature at 930 K and 1500 K for: Self-Interstitial mediated[128] diffusion, Vacancy mediated diffusion near the surface [129], Frenkel-Pair formation mediated diffusion[107], surface diffusion[127]. Compare to the estimated diffusion coefficients of $1.61 \times 10^{-3} cm^2/s$ and $6.5 \times 10^{-7} cm^2/s$.

of the interstitial or vacancy diffusion coefficients match the observed laser enhanced diffusion coefficient, $1.61 \times 10^{-3} cm^2/s$. The diffusion coefficients for interstitial, vacancy, surface, and laser enhanced diffusion are plotted in Figure 5.3.

The observed rates cannot be explained using a purely thermal model of diffusion, and thus a strong non-thermal enhancement of the diffusion coefficient must be present. The next section will discuss a model of how the ultrafast laser enhances the diffusion process.

5.2 Laser Enhanced Mass Transport

5.2.1 Ultrafast Point Defect Formation

In order to understand how mass transport in GaAs is enhanced, it is helpful to discuss how point defect formation occurs during ultrafast irradiation[5, 8]. When an ultrafast laser is incident on a semiconductor, lattice distortion occurs at fluences below the single shot melt threshold because of bond weakening [3]. This weakening is caused by a decrease in the attractive part of the interatomic potential due to the high carrier excitation [125]. X-Ray diffraction experiments confirm that the root mean squared displacement of atoms at room temperature reaches up to one angstrom in a few hundred femtoseconds [23]. The high degree of lattice disorder

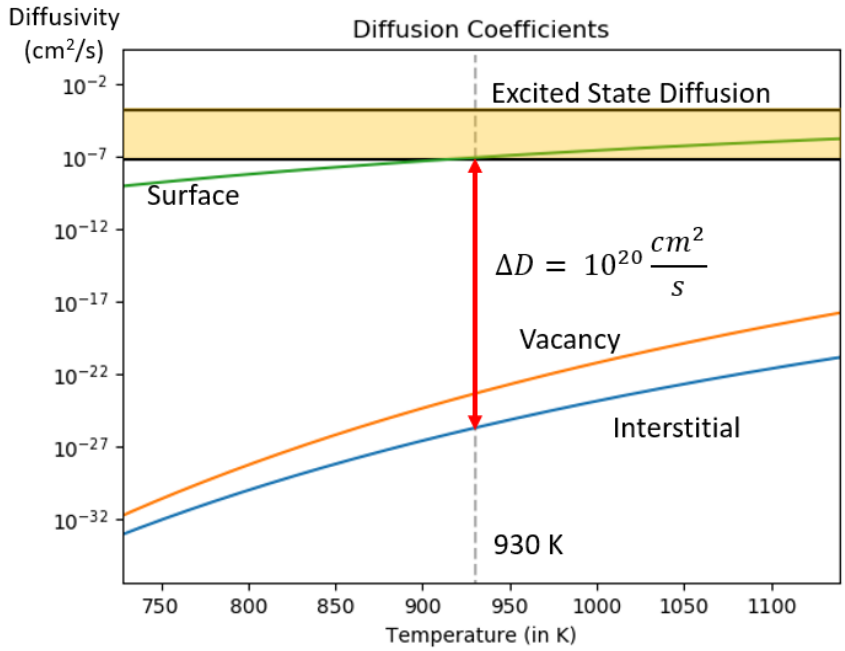

Figure 5.3: Diffusion coefficients of interstitial [110], vacancy [107, 110], and surface[127] diffusion found in the literature. The horizontal lines represent the region for the diffusion coefficient during excited state mediated diffusion. The vertical line represents the maximum temperature the sample could reach, 930 K. The diffusion coefficient for interstitial diffusion is enhanced at least 20 orders of magnitude.

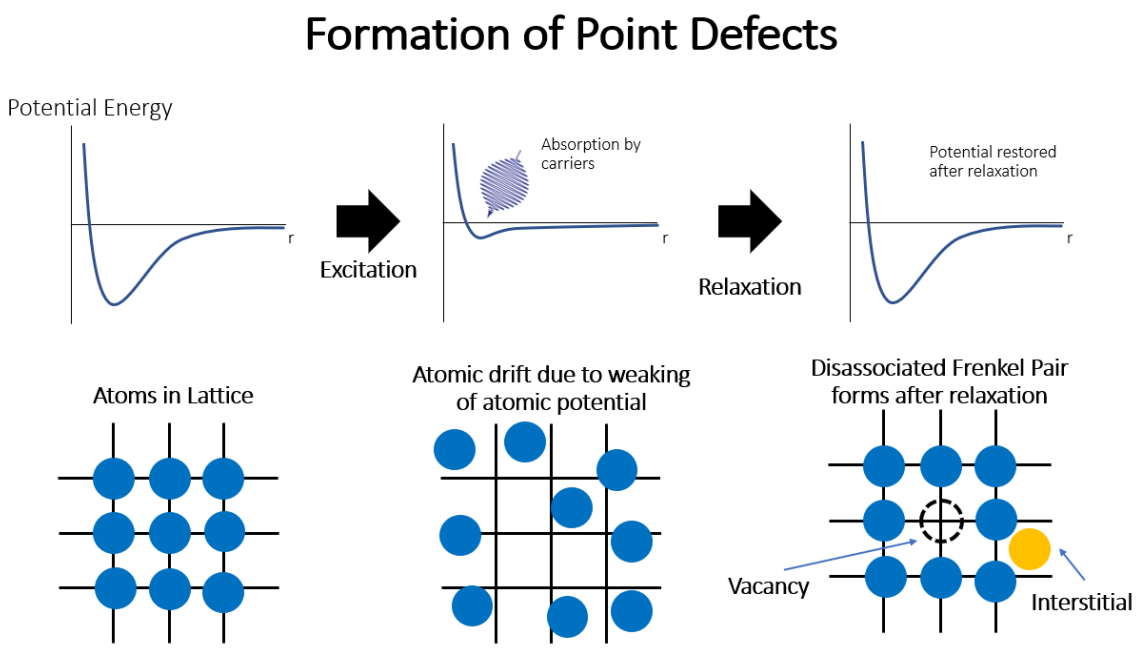

Figure 5.4: A schematic representation of the point defect formation mechanism. The incident pulse causes a weakening of the interatomic potential. The atoms can drift due to having an initial room temperature vibrational energy. Atoms can then recombine with excited carriers at interstitial points, where the carrier density is highest, creating a dissociated Frenkel pair. As the material continues to be irradiated, the point defect density increases. During the weakening of the interatomic potential, interstitial diffusion through the lattice is increased.

causes the band gap to close [1, 3], thus recombination of electron hole pairs can be nearly instant. This, coupled with the fact that the density of the carriers is highest near the interstitial sites [130], means that atoms that have enough kinetic energy to reach interstitial sites are much more likely to recombine with an electron-hole pair and become interstitials. This model for the formation of point defects is non-thermal, in contrast with point defect mechanisms with nanosecond lasers [131]. A schematic of the point defect formation mechanism is found in Figure 5.4.

5.2.2 Excited State Mediated Diffusion

During the first picosecond after irradiation the lattice atoms are highly disordered because the interatomic potential was significantly weakened. This meant that atoms

are free to move with whatever kinetic energy they had prior to ultrafast excitation. A schematic representation of important properties of the lattice during this regime is shown in Figure 5.6b. During this period the interstitial transport is not expected to follow thermal diffusion models, thus calculating a diffusion coefficient in the way that was done in the previous section is not accurate. On the other hand, these interstitials could be described as having Brownian motion. Using Equation 2.33 and the fact interstitials can travel up to half of the unit cell during the first picosecond after excitation [11, 23], a diffusion coefficient of $5.32 \times 10^{-4}\ cm^2/s$ is calculated. This diffusion coefficient is close the laser enhanced diffusion coefficient estimated previously, $1.61 \times 10^{-3}\ cm^2/s$, which is indicative that the interstitial transport that is observed during the formation of the HSFL is closer to kinetic transport than classical diffusion.

While kinetic transport of interstitials is expected to occur during the first picosecond after excitation [11, 23], it must be determined whether other mechanisms could be extending the kinetic transport regime. Even after the electrons form a Fermi-Dirac distribution, the interatomic potential is still weakened due to the high excitation of electrons (Figure 5.6). This means that throughout the next 10 ns, diffusion of interstitials is enhanced by the fact that the energy barrier for hopping is lowered. This lowering of the energy barrier is due to the fact that the strength of the bonds that have to be broken in order for an interstitial to diffuse from one interstitial site to another is much lower due to a large density of the bonds being in a anti-bonding state. A schematic of this is shown in Figure 5.5a.

Another possible source for the diffusion enhancement, which occurs in the same timescale as the previous mechanism discussed previously, is the recombination stimulated diffusion discussed in section 2.7.3, specifically the charge state effect mechanism. While the work has previously not been expanded to include femtosecond irradiation, it has been shown that enhancement of interstitial diffusion is dependent

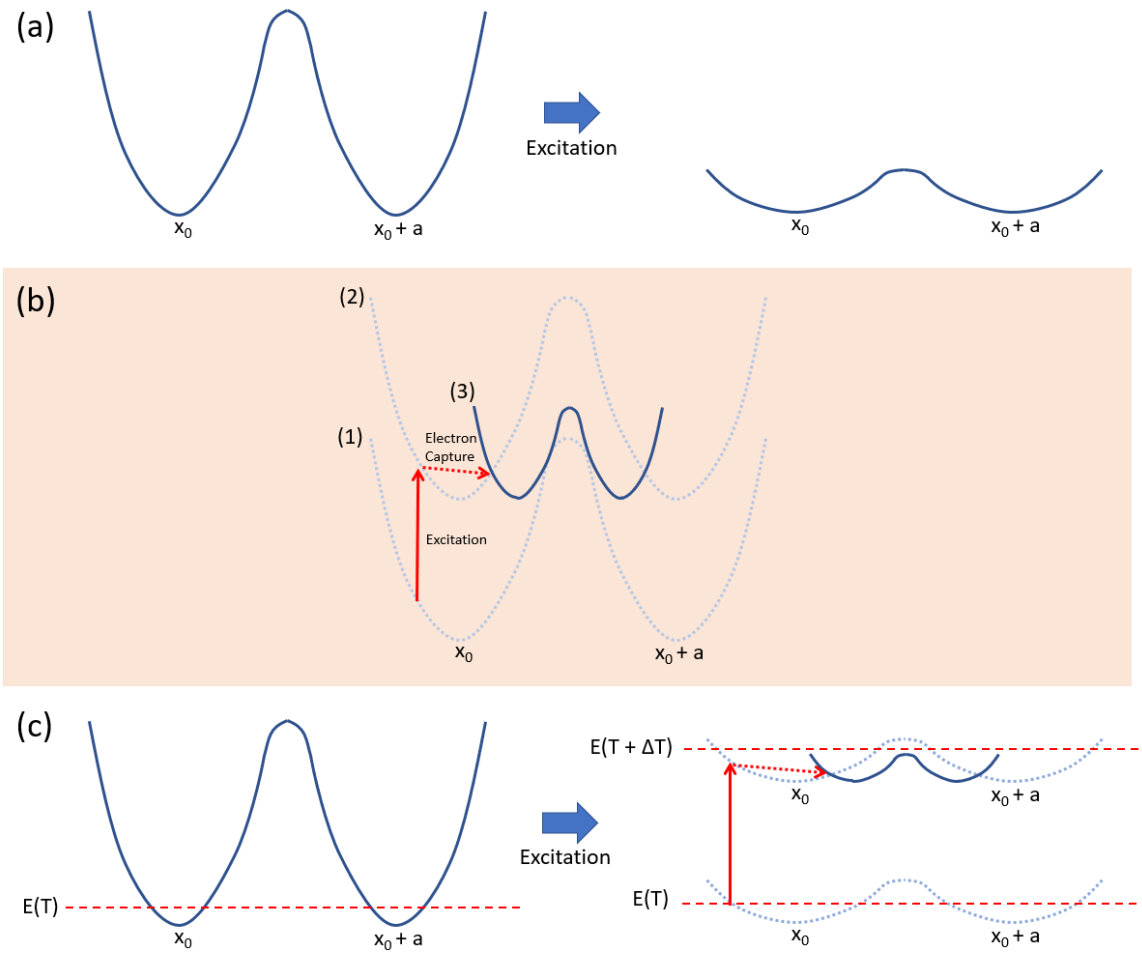

Figure 5.5: Configuration coordinate (CC) diagrams of the different mechanisms for excited state mediated diffusion. CC diagrams are schematic representations of the energy level of an atom. "x0" represents the origin interstitial location, and x0 + a represents an interstitial site located a distance "a" away. (a) Shows the weakening of the interatomic potential due to high electron excitation. (b) Shows the charge state diffusion mechanism [111]. Prior to excitation, the interstitial is in the neutral charge state represented by the energy curve labeled (1). After irradiation, the interstitial is excited to a higher level energy curve labeled (2). The interstitial can then capture an electron, which causes it to transfer to the charged state energy curve labeled (3), which has a lower energy barrier for excitation [10]. (c) Shows the combination of the weakening of the interatomic potential and charge state diffusion cause the activation barrier to be decreased further than if each individual mechanism acted alone. Furthermore, higher temperature causes the interstitial to have higher kinetic energy to overcome the already weakened barrier.

on irradiation intensity [111]. The high density of electrons in the conduction band means that interstitials have a high probability of capturing electrons, and thus allow diffusion through the charge state mechanism to occur. A schematic of this mechanism is shown in Figure 5.5b. It is important to note that the charge state diffusion mechanisms would also be enhanced by the bond softening, considering that the energy barrier for interstitial hopping would be further lowered, thus a combination of the bond softening mechanism and the recombination mechanisms lead to higher enhancement of mass transport rates than each mechanism working alone; The sum of the parts are greater than the whole. Lastly, a few picoseconds after excitation, carrier-phonon interactions lead to heating of the lattice. This means that for the next 10 ns, the lattice is at an elevated temperature. The diffusion coefficient has an exponential dependence on temperature, thus even though temperatures higher than 930 K are not observed, the interstitial transport occurs at a higher velocity than if the material remained at room temperature.

It is likely then that all these effects are working alongside each other in order to achieve the anomalous diffusion coefficients observed. During the first ps, ballistic transport of interstitials at room temperature drives the mass transport mechanism. Even after the electrons relax and room temperature transport is not observed for lattice atoms, the heating of the lattice and charging of the interstitials likely extend the duration of the kinetic transport mechanism past the 1 picosecond timescale. A schematic of all the mechanisms working together is shown in Figure 5.5c. Even when the interatomic potential is recovered to the point where kinetic transport is not possible even with a charged interstitial, classical diffusion of interstitials could proceed at an enhanced rate due to the lowering of activation barriers for hopping.

Excited state mediated diffusion should not be compared with diffusion of interstitials in a solid lattice, as was done in the preceding section. The diffusion mechanism discussed in this section is closer to diffusion of an atom in a liquid, where the atom

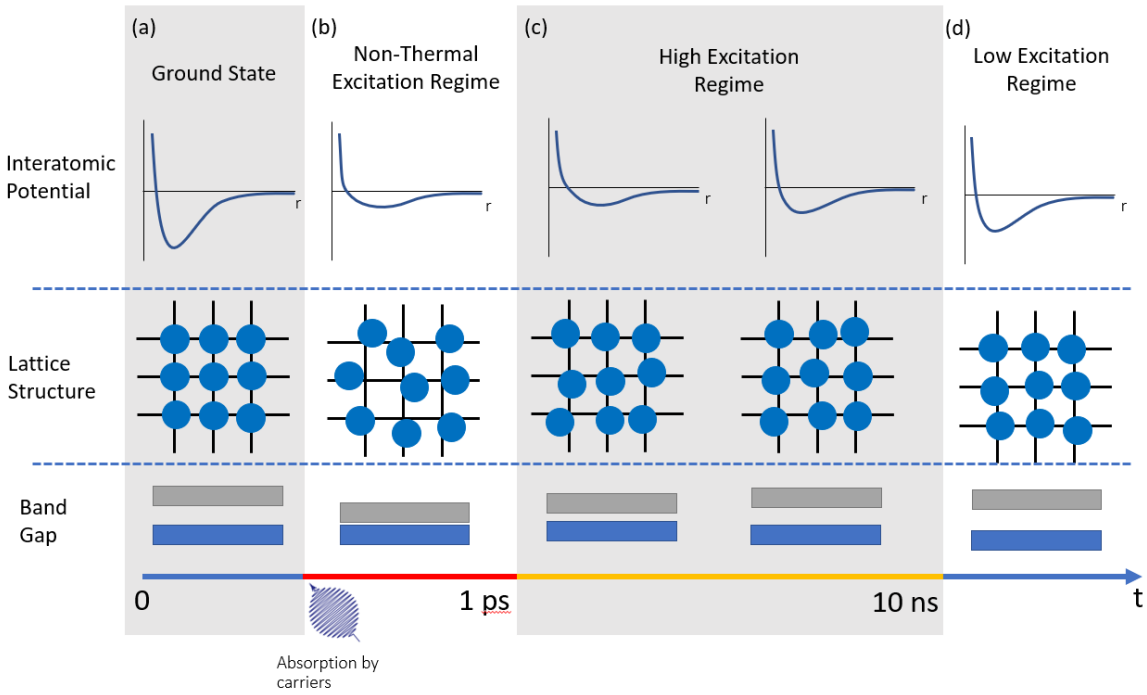

Figure 5.6: A schematic representation of the three proposed regions of excitation. (a) shows the material at room temperature. The band gap is fully opened, atoms are still in their respective lattice sites, and the electron are located in the valence band. (b) shows the first 1 ps after excitation. The electrons are now in an excited non-thermal distribution in the conduction band. The excitation puts electrons from the bonding state to the anti-bonding state, weakening the interatomic potential. The weakening of the interatomic potential causes atoms to drift with their room temperature velocity, which causes disorder in the lattice. Because of this increased variation of the atom locations, the material's band gap closes. (c) shows the next 10 ns of the excitation. The excited electron density has now thermalized to a Fermi-Dirac distribution. The lattice atoms are no longer free to drift, but the weakened interatomic potential still causes some deviation from the perfect lattice sites. Over the 10 ns, the electrons relax to the ground state, which causes the interatomic potential to recover and the bandgap to open. (d) After 10 ns, most of the electrons relax to the ground state, which completely opens up the band gap.

is weakly bonded and there is decreased long range ordering. The diffusion coefficient for a Ga interstitial in liquid GaAs at the melt temperature is 5×10^{-7} cm^2/s [132], which is within the range of calculated diffusion coefficients for excited state mediated diffusion. Even though the materials studied in this thesis are not being melted, the similarity between the liquid diffusion and excited state diffusion mechanism is suggestive that the kinetic mass transport model that was proposed is correct.

The diffusion mechanism that occurs after kinetic transport is similar to the fast diffusion mechanisms that have been observed for certain dopants at high enough concentration in metals[133] and semiconductors[128]. The laser first serves to create a high population of interstitials far from vacancies, which causes diffusion to be mediated by interstitials. Then, while the self-interstitials would normally form fairly strong bonds with nearby atoms and thus diffusion would require the breaking of these bonds, the weakening of the interatomic potential from laser excitation means that the interstitials would be weakly bonded to the lattice atoms. This is analogous to dopant diffusion in the fast diffusion model, where the dopant atom in the interstitial site is not bonded to the lattice and can freely move around with a diffusion coefficient on the order of 10^{-4} cm^2/s, which is within a few orders of magnitude as the calculated diffusion coefficient during HSFL formation.

5.3 Removal Rate of GaAs in Vacuum

In the previous sections, it was shown that the formation of HSFL with 780 nm light in air requires laser enhanced diffusion to occur. In this section, the rates in which the phenomena discussed in Chapter 4 will be examined. Figure 5.7 shows AFM of the crater formed after 1000 irradiations with 390 nm light at a peak fluence of 0.018 J/cm^2. To calculate the removal rate, the depth of the crater was measured at various points in the crater. Since the height does not significantly change within a 500 nm distance, it was assumed that the removal was a cylinder with a radius of 250

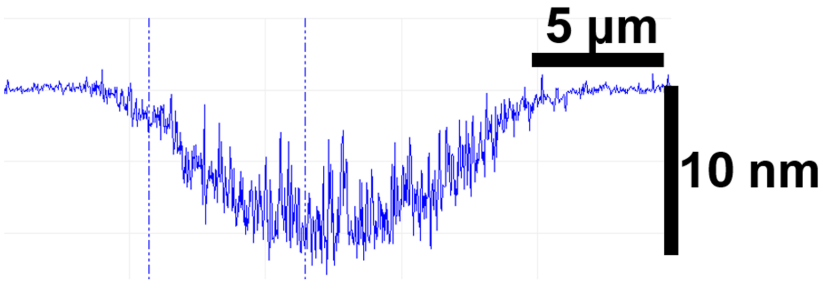

Figure 5.7: Cross section AFM of the crater formed after 1000 irradiations with 390 nm light in vacuum at a peak fluence of 0.018 J/cm^2. The depth of the crater is dependent on the local fluence. The depth at each fluence was used to calculated the average removal rate.

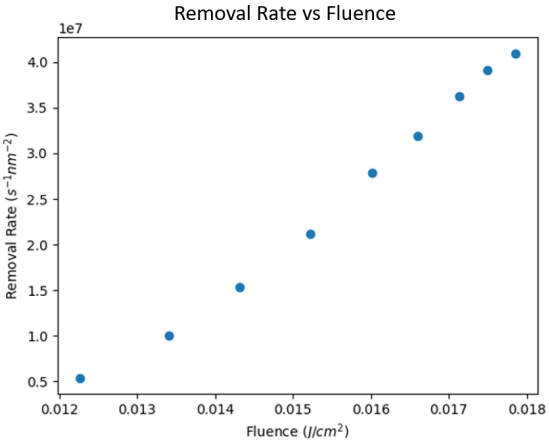

Figure 5.8: The removal rate as a function of fluence calculated using the AFM cross section of the irradiation crater formed in GaAs after 1000 irradiations with 390 nm light at a peak fluence of 0.018 J/cm^2.

nm, and a height dependent on the fluence. For peak fluence, it was determined that the height of the crater is roughly 9.3 nm. Using $\pi r^2 h$, and multiplying by the atomic density, it was found that 410 atoms were removed per nm^2 over 10,000 irradiations, or 0.41 atoms/nm^2/shot. Assuming removal only occurs for 10 ns, a removal rate of 4.1×10^7 atoms/nm^2/s is calculated.

The rates observed for this removal are similar to the rates observed for the growth of HSFL with 780 nm light that was reported in the previous section. The same calculation was repeated for various fluences, as shown by Figure 5.8.

The removal rate as a function of fluence appears to be mostly linear. The non-

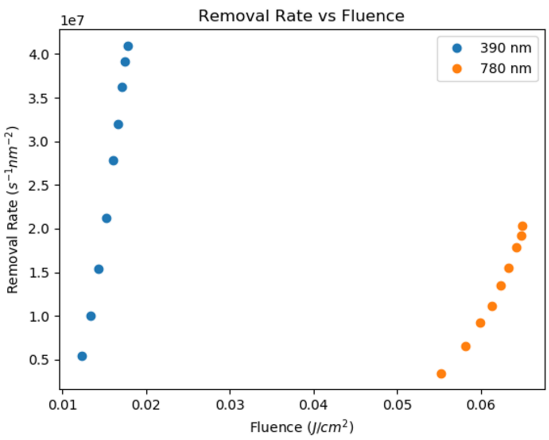

Figure 5.9: The removal rates for both irradiation with 780 nm and 390 nm in vacuum. The desorption rates observed are on the same order of magnitude for both irradiation conditions at fluences below the melt threshold in which the point defect formation and diffusion mechanism is expected to be active.

linear change between the two highest fluences could be explained as a saturation of the desorption, similar to the saturation that can be seen in Figure 4.2. Evidence of significant preferential removal of As in the form of gallium droplets do not appear, suggesting that the temperature for irradiation with 390 nm light at a fluence of 0.018 J/cm^2 also does not exceed 930 K. When comparing the rates observed with that of thermal desorption at similar temperatures [134], it can be seen that rate for desorption with a laser are at least 6 orders of magnitude higher, indicating that laser excitation has a major enhancement in the desorption rate.

A similar analysis to calculate the removal rate was done on the crater formed by irradiation with 780 nm light after 10,000 irradiations. The calculated rates for the 780 nm light irradiation in vacuum, alongside the calculated rates for 390 nm light in vacuum, are plotted in Figure 5.9.

The calculated rates from both 780 nm and 390 nm light irradiation are on the same order of magnitude at the fluences in which the formation of HSFL is observed. Enhanced desorption occurs between the bandgap collapse threshold and the melt threshold of the material, providing more evidence that bandgap closure is a necessary aspect of the enhanced desorption process.

Studies on the fluence dependence on removal yield for femtosecond excitation in Si has previously been done [135]. In this study, it was shown that the removal yield changed non-linearly as a function of fluence, which differs with the linear dependence of the removal rate with fluence shown in Figure 5.8. It is possible that at lower fluences desorption does not lead to macroscopic changes. On the other hand, desorption induced by excitation with 780 nm light does appear to be linear with fluence.

The most crucial difference between laser desorption in Si and GaAs is that laser induced desorption in GaAs has only been shown to occur in the presence of surface defects [120]. If the surface had pre-existing surface defects, only removal on the order of 1 ML would be expected. Once the first few layers are removed, the surface would become defect free. This is suggestive that there could be a link between the point defect mechanism described in the previous section and the desorption rate observed, since a flux of defects would be necessary to continuously feed the desorption process.

While there is evidence that point defect formation and diffusion are necessary for desorption, whether enhanced defect transport is occurring cannot be easily calculated from the removal rate. In order to determine this, a simple model was constructed to determine how the flux of surfacing point defects affects the removal rate. For simplicity, a discrete Monte Carlo (MC) model, which uses a Solid-on-Solid approach to describe the surface structure [136], was used. In a solid-on-solid model, crystal structure and surface reconstructions are not considered, and each surface atom can be described by a single value representing the height profile. In this model, the surface atomic structure is represented by a NxN matrix, where N is the number of atoms in the simulation. Physically, each element in the matrix represents an atom that is a distance (d) away from the other element. The value of each element represents how far from the original surface the topmost atom in each element is. A value of 0 represents that the atom is at the original surface, while a negative

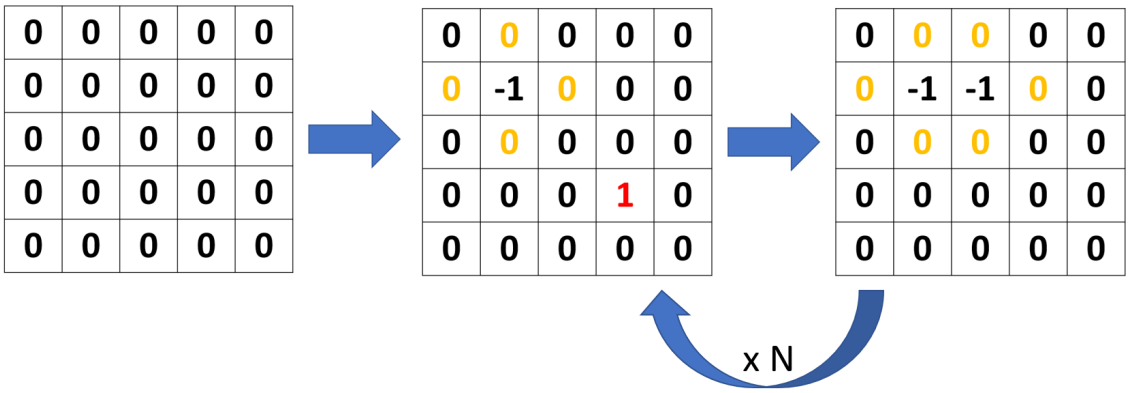

Figure 5.10: A schematic showing the algorithm used. A matrix with all elements set to 0 zero is first created. Atoms and Vacancies are introduced by either adding or subtracting to each element. The probability of removal for each atom is determined by the number of nearby atoms at a lower value, as shown by the colored numbers. Atoms are removed based on their probability, and the process is repeated up to N total number of irradiations.

value represents that the topmost atom is below the original surface. To determine the probability of removal, the values of neighboring elements are considered. If a neighboring element has a lower value, then the probability for removal increases. A schematic representation of this is shown in Figure 5.10.

When the simulation is run, the following happens:

1. A NxN matrix with all cells at 0 is created to represent a pristine initial surface

2. 2J number of cells in the matrix are selected, where J is the number of interstitials and vacancies that arrive at the surface every shot. Then, to represent interstitials, the current depth of half of the selected cells are increased by one. To represent vacancies, the current depth of half of the selected cells are decreased by one.

3. Each element is evaluated for removal. The higher the number of neighboring "atoms" the lower the probability of removal for a given atom, and vice versa.

4. (2) and (3) are repeated up to the number of irradiations.

While fairly simple, and does not include all the possible physics, this model should at least indicate whether an enhanced point defect mechanism is necessary for the removal rates that are observed. For the simulation that was run in this chapter, the following assumptions were made:

1. The removal probability of an atom is given by e^{E_a/k_bT}, where E_a is the activation energy for desorption.

2. The activation energy for desorbing an adatom was set to 0.13 eV. This corresponds to a 20% chance of removal of an adatom.

3. The desorption probability for desorbing a fully bonded atom on the surface is zero.

4. The probability of desorption between that of an adatom and of a fully bonded surface atom changes linearly.

5. The temperature of the material was 930 K.

6. The maximum value possible for the number of interstitials and vacancies arriving at the surface is 0.41 $1/nm^2$.

Since no data on the activation energies for laser induced desorption in GaAs is available, assumption (2) was made based on the activation energy for thermally desorbing an atom, 1.9 eV [137]. It is known that the point defect generation activation energy drops by a factor of x15 when comparing thermal and laser induced formation[131], thus a similar multiplicative factor was applied. Assumption (3) was done based on the fact that laser desorption from non-defective surfaces has not been observed in pristine GaAs [120].

Figure 5.11 shows the results of the simulation for different atomic fluxes. Figure 5.11(a) shows the simulation using an atomic flux of 0.001 atoms/nm^2/irradiations.

This flux is already higher than would be predicted using thermal models, yet the removal rate does not match the experimental observations. Figure 5.11(b) shows the simulation using an atomic flux of 0.01 atoms/nm^2/irradiations. The change in the depth increased, suggesting that the point defect formation and diffusion has a significant impact on the desorption rate. Figure 5.11(c) shows the result of the simulation after assuming an atomic flux of 0.22 atoms/nm^2/irradiations. As it can be seen from the results of this simulation, the resulting depth is on the same order of magnitude as that which is observed when irradiating with 390 nm light. This is strongly suggestive that in order to have removal rates on the order of magnitude of 0.41 atoms/nm^2shot, an enhanced point defect mechanism needs to occur.

In summary, this section has shown that the desorption rates observed when irradiating with 390 nm light and 780 nm light in vacuum are 6 orders of magnitude higher than would be expected in thermal desorption. It was also shown that a point defect flux of 0.22 atoms/nm^2/irradiations was necessary in order for the desorption at the observed rates to occur, even if the decrease of the activation energy for laser induced desorption is taken into account. This flux rate is similar to flux rate calculated in section 5.1, 1.61 atoms/nm^2/irradiations, which is indicative that the point defect formation and diffusion mechanism discussed in section 5.2 is occurring. The flux rate for irradiation with 390 nm light was determined by modeling the system using a discrete Monte Carlo model, and varying the point defect flux until the simulation results matched the experimental results. While this model showed the importance of having an anomalous point defect formation and diffusion mechanism, it is still far too simplistic to fully determine what the actual flux rate is. A simulation including surface reconstructions and a better value for the desorption activation energy should be used to determine the actual point defect flux.

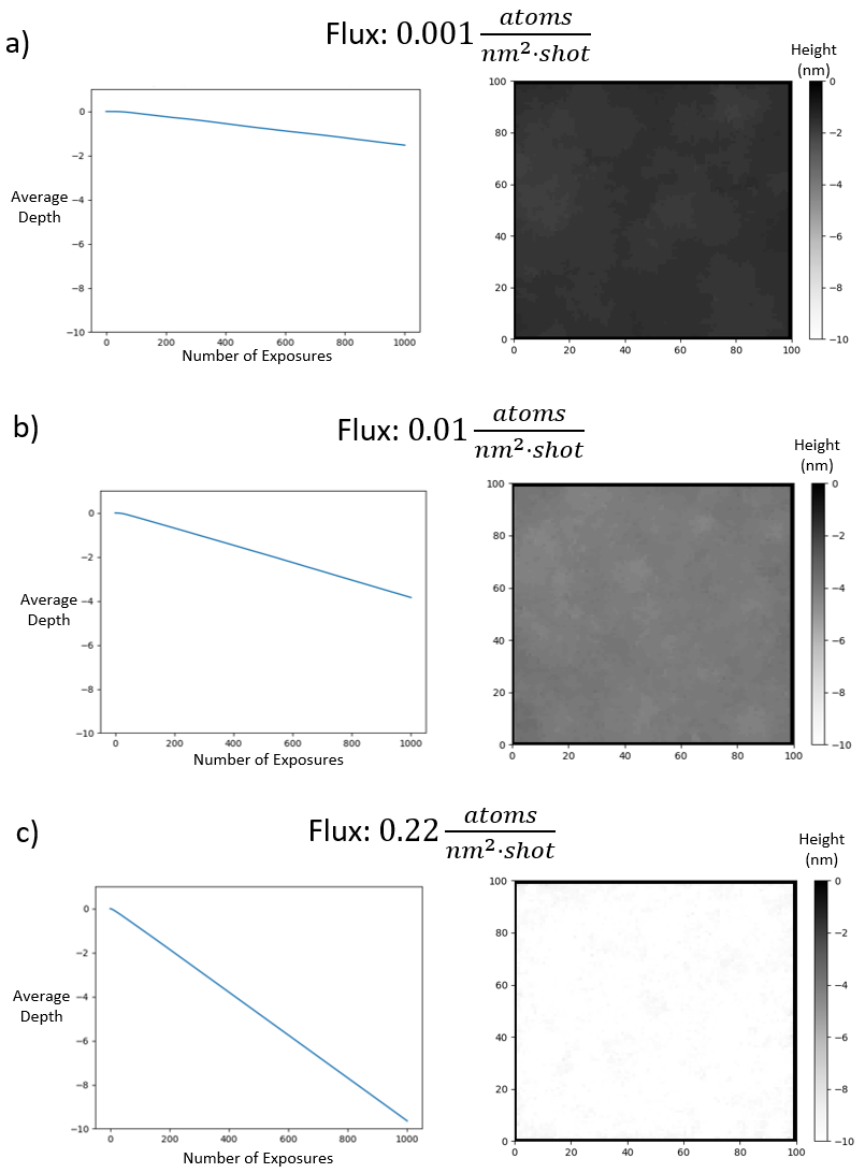

Figure 5.11: Simulations run for the point defect enhanced removal. (a) Shows the result with an atomic flux of 0.001 atoms/nm^2/irradiation. The average depth change is not as it was observed experimentally, indicating that a higher flux is necessary. An atomic flux of 0.001 atoms/nm^2/irradiation is still higher than thermal models would predict. (b) Shows the result with an atomic flux of 0.01 atoms/nm^2/irradiation. The average depth change is higher than before, showing the importance of point defect generation and diffusion. (c) Shows the result with an atomic flux of 0.22 atoms/nm^2/irradiation. The average depth change matches that which is experimentally observed. The 2D height profile shows evidence of layer by layer removal, which is what would be expected based on laser desorption studies of GaAs [120]

CHAPTER VI

Anomalous Oxidation of Silicon

6.1 Enhanced Oxide Growth in Si

Another system that was investigated was the growth of oxide on Silicon upon multiple irradiations with 390 nm, 150 fs laser pulses at various fluences below the single shot ablation threshold. Figure 6.1 shows the result of these irradiations. From this figure, it can be seen that there is a strong fluence dependence on the growth rate of the oxide. As the number of irradiations increases, the thickness of the oxide grows until it reaches a saturation height, in which the thickness of the oxide does not dramatically increase further. This saturation is represented by the fact that the height profile of many of the oxides goes from a gaussian-like profile due to different growth rates at different fluences to having a flat profile at the top, due to higher fluences reaching the saturation height faster. Cross section SEM (Figure 6.3) confirms that this oxide reaches heights up to 8 μm after 100 seconds of irradiation. Oxide growth on this scale and rate has previously not been observed in both thermal and laser assisted oxide growth.

The single shot ultrafast melt threshold of Si with 390 nm light is 0.045 J/cm^2, thus in order to not have to take into account possible enhancement effects of the growth rate due to melting, the oxide growth at a fluence of 0.039 J/cm^2 was used for a more in-depth analysis. This is also the regime in which the HSFL formation in Si

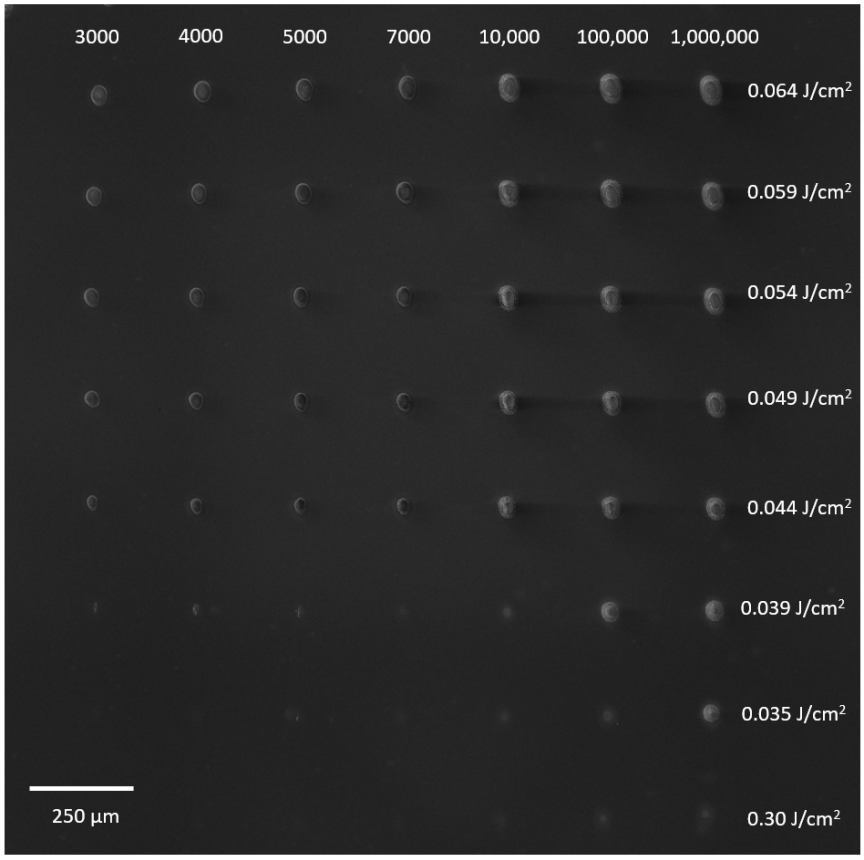

Figure 6.1: Overivew of the SiO_2 growth in Silicon. The number of irradiation increases from left to right, and the peak fluence decreases from top to bottom. There is a strong fluence dependance on the formation of the SiO_2. Strong enhancement in the growth of the oxide is observed when using fluences close to the single shot melt threshold of Si ($0.045\ J/cm^2$).

is observed, thus allows for a cleaner comparison between the underlying mechanisms for the enhanced growth rate during the formation of HSFL and the growth of oxide on Si upon irradiation with 390 nm light. While at first these two mechanisms appear to be unrelated, this section will present evidence that the two processes are linked by an enhanced point defect diffusion and transport mechanism.

Oxide growth in Silicon occurs at the interface. As the oxide growths, the Silicon underneath gets replaced with SiO2. There are two distinct regimes that occur during the thermal growth of oxygen [95]. The first regime is when the oxide is <100 nm thick. In this regime, the oxide growths at a rapid rate, and it is limited by the availability of Si to bond with oxygen, the disassociation of O_2 into 2O for dry oxide growth, and the disassociation of H_2O into H + 2O for wet oxide growth. The second regime occurs when the oxide layer thickness is greater than 100 nm. The growth rate of the oxide during this regime is much slower than that during the first 100 nm. Since as mentioned before, growth occurs at the interface, the limiting factor for growth during this regime is the diffusion of oxygen or water molecules through the oxide into the interface [93]. The rate of growth is dependent on whether the oxide is grown in a dry or wet environment, since O_2 has a slower diffusion rate than H_2O in SiO_2 [138].

Figure 6.2 shows the morphology during the initial growth of the oxide. As it can be seen, it does not grow uniformly throughout the irradiated area, and the formation of islands is observed. It is not yet clear whether the morphology is in the Si or in the oxide. Since thermally grown oxide is expected to grow uniformly, this morphology makes comparison difficult.

Figure 6.3 shows a cross section image of the growth that occurs after 100,000 exposures with 390 nm light at a fluence of 0.039 J/cm^2. Scattering from the rough surface and from multiple interfaces in the oxide lead to less light making it to the Silicon underneath, which can serve as an explanation why the growth of the oxide

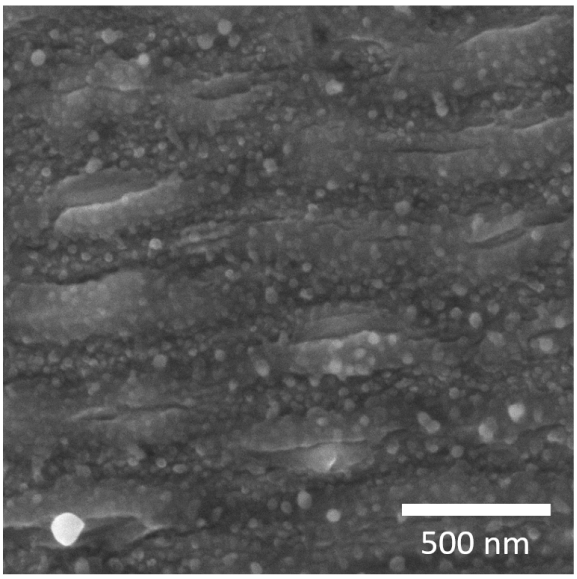

Figure 6.2: SEM of the oxide that grows after 500 exposures with 390 nm pulses at a local fluence of 0.039 J/cm^2. The formation of islands and of a corrugated surface is observed, yet whether these are in the oxide or the oxide is forming a layer over this morphology has not been determined.

appears to saturate after a certain thickness.

The cross-section image reveals a discrepancy between the known models for oxide growth in Silicon and the oxide growth that is observed. Since oxide growth occurs in the interface, the only reason that oxide is observed above the original surface is because of the difference in the density between the oxide and silicon. The lower density and higher molar mass of amorphous SiO_2 (2.2 g/cm^3, 60.08 g/mol) compared to those of Silicon (2.3 g/cm^3, 28.08 g/mol) mean that oxide takes up more volume per mol than Silicon. The fraction of the oxide below the original surface can be calculated using [139]:

$$\frac{t_{Si}}{t_{SiO_2}} = \frac{V_{Si}}{V_{SiO_2}} = \frac{M_{Si}/\rho_{Si}}{M_{SiO_2}/\rho_{SiO_2}} \tag{6.1}$$

where t_{Si} is the thickness of the silicon that is consumed, t_{SiO_2} is the total thickness of the oxide, V is the volume corresponding to each thickness, M is the molar mass, and ρ is the density. Plugging in the values for amorphous SiO_2 and crystalline

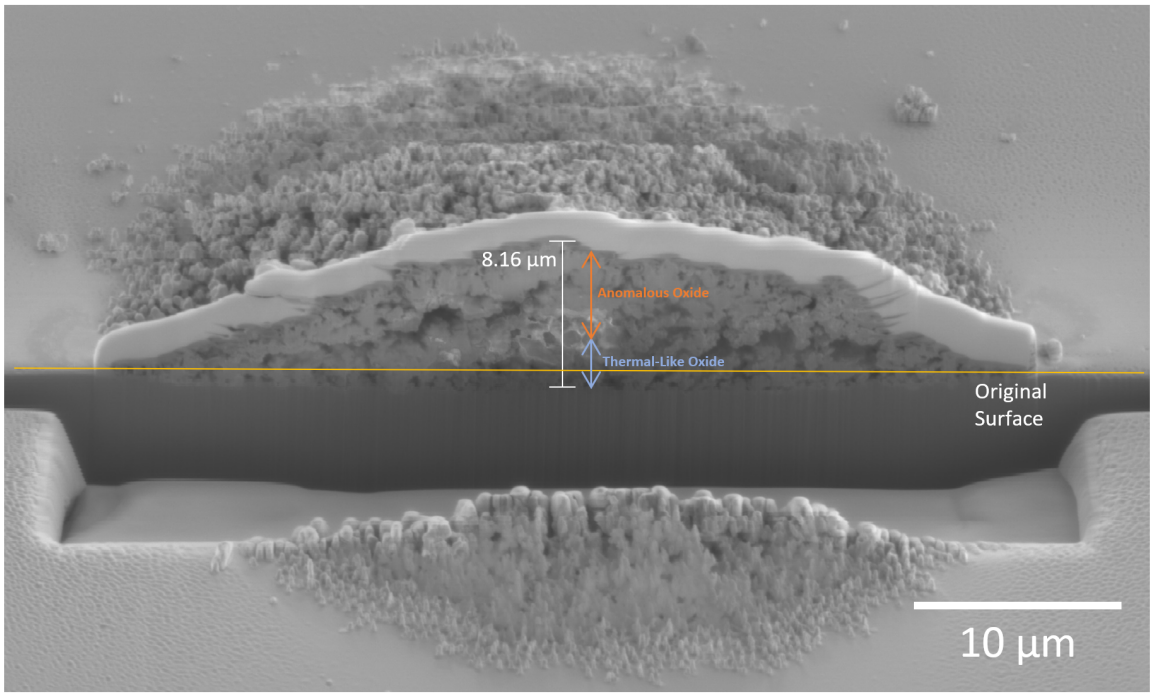

Figure 6.3: Cross-Section SEM of the oxide that grows after 100,000 irradiations of Silicon with 390 nm light at a peak fluence of 0.039 J/cm^2. The oxide thickness as the peak is 8.16 μm. 77% of the oxide is above the original surface (represented by the yellow horizontal line), which is higher to what is expected if the growth of the oxide followed the existing model. The bright region on top of the oxide is platinum that was deposited to protect the sample from ion beam damage. The sample stage is rotated 52 degrees, which causes the mismatch between the reported thickness and the scalebar.

Silicon, 44% of the SiO2 is found below the original surface. As shown in Figure 6.3, the thickness of the oxide below the original surface is only 17% of the total oxide thickness, even accounting for the large voids present in the oxide. This indicates growth does not only occur in the oxide/Si interface, but also in the Air/Oxide interface, which can only occur if Silicon interstitials migrate to the surface of the oxide. Figure 6.4 shows a schematic representation of each of the oxides. To determine the thickness that corresponds to oxide growth at the interface, the oxide thickness below the surface was measured, then the total thickness was calculated by using the fact that 44% of the total SiO_2 is below the surface for oxides grown at the interface. It was found that thickness of the oxide grown at the interface was 2.34 μm, with 1.078 μm below the original surface and 1.262 μm. It should be noted that the thickness of the interface grown oxide matches with the distance between the interface and the bottom of the large crack in Figure 6.3, although whether this is coincidental or physical has not been determined.

The fact that over 80% of the oxide is above the original surface is further evidence of the hypothesis that a point defect formation and diffusion mechanism results in the anomalous oxide growth observed is correct. Figure 6.5 shows a cross section SEM of the oxide that is grown after 1 million irradiations. The thickness of the oxide has not increased significantly, going from 8 μm to 10 μm in 900,000 irradiations. The only significant difference is that the voids are much smaller. This further supports the idea that there is a third mechanism in which growth is dictated by the diffusion of Silicon atoms through the oxide. The silicon interstitials that reach the voids bond with oxygen species that are present inside the voids, or that diffuse to the voids from the atmosphere.

This means that unlike for thermal oxide growth in which there exists two distinct growth regimes, growth with ultrafast lasers has a possible three distinct regimes. The regimes are as follow:

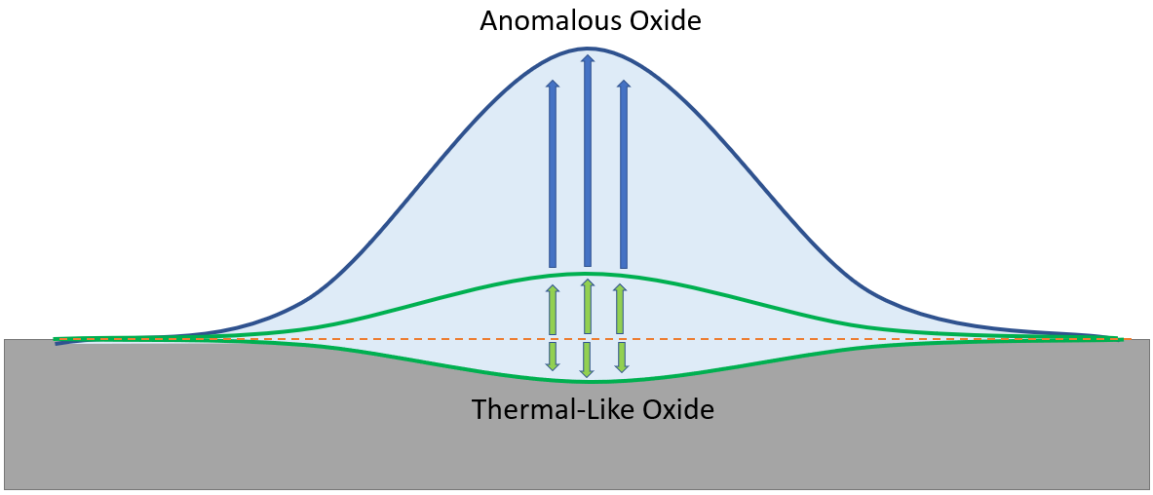

Figure 6.4: A schematic representation of the oxide growth upon ultrafast laser irradiation, displaying that growth occurs at two different interfaces. One of the oxides grows in the same manner as thermally grown oxide, where oxygen atoms diffuse through the oxide to the SiO_2/Si interface. The other oxide, which has not been previously observed in literature, grows in the SiO_2/Air Interface. This oxide growth is driven by Si atoms diffusing through the oxide layer to the outer interface. The large flux of Si atoms that make up this oxide can only be explained if an enhanced point defect and diffusion mechanism is invoked.

1. Oxide thickness less than 100 nm: The thickness is thin enough so that there is an abundance of oxygen, thus the limiting factor is the ability for oxygen species to bond with Si atoms on the surface.

2. Oxide thickness between 100 nm and 8 μm: Oxide growth is now caused by two different mechanisms. Oxygen diffuses to the oxide/Si interface and eats away at the Silicon substrate causing the formation of oxide both above and below the surface. At the same time, Silicon diffuses through the oxide and binds with oxygen atoms in the atmosphere to grow oxide solely above the original surface.

3. Oxide thickness around $8\mu m$: The rate of oxide growth decreases as this point. The voids inside the glass begin to close due to diffusion of silicon atoms from the bulk which bonds with oxygen species that diffuse into the voids.

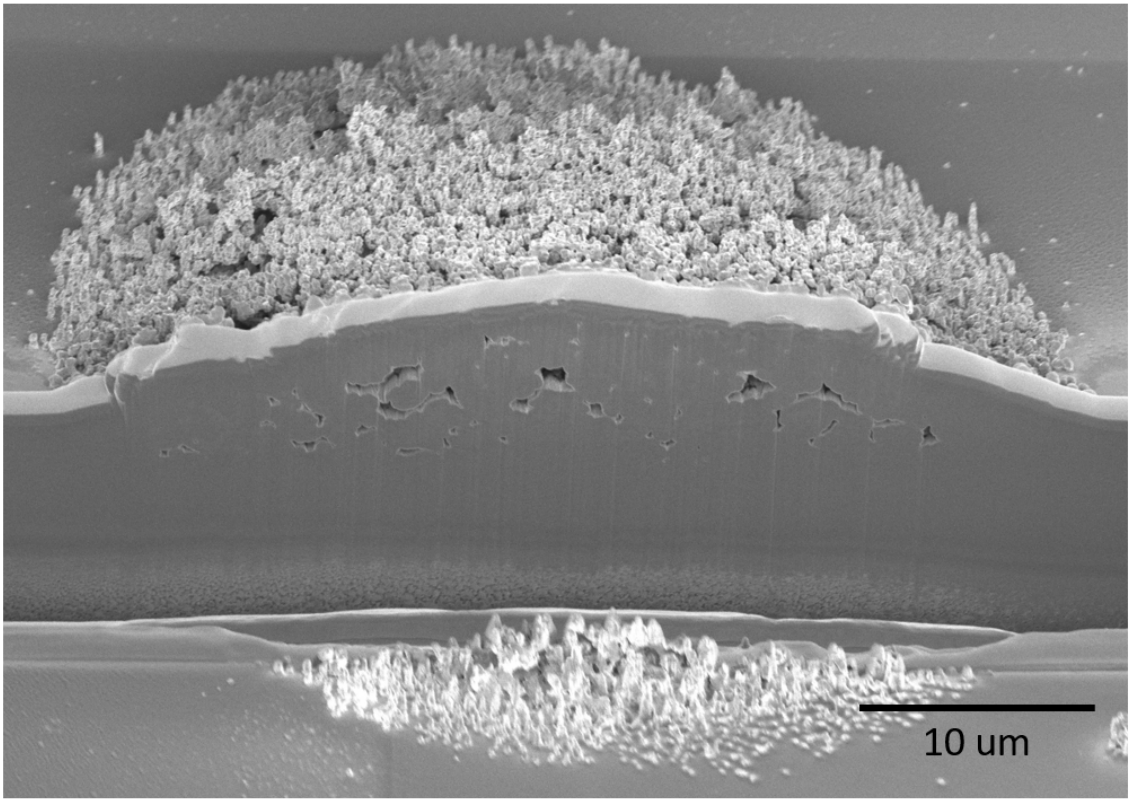

Figure 6.5: Cross-Section SEM of the oxide that grows after 1,000,000 irradiations of Silicon with 390 nm light at a peak fluence of 0.039 J/cm^2. The height of the structure has not increased drastically, showing that the oxide growth saturates. Furthermore, the density of the SiO_2 increases due to filling of the voids. The sample stage is rotated 52 degrees.

6.2 Diffusion Rate Calculations

Before further discussion on how the laser enhances the growth rate of the oxide in each regime, calculations on how much the total average growth rate is increased needs to be done. To do this, the cross section of the oxide that grows upon after 100,000 irradiations with 390 nm light at a fluence of 0.039 J/cm^2 was used (Figure 6.3b). Since there are distinct mechanisms for the formation of this oxide, the thickness of the oxides, t_{SiO_2}, will be split between each mechanism. The measured and calculated values for total oxide growth, growth that occurs at the SiO_2/Si interface, and growth that occurs at the SiO_2/Atmosphere interface are found in Table 6.1, along with calculated growth rates and calculated diffusion fluxes for the diffusive species. As in previous calculations, the growth rate and flux were calculated by assuming that the growth occurs until 10 ns after excitation, which is when the electrons in the material are still in a Fermi-Dirac distribution in the conduction band. The calculated growth rate is $8.16 \times 10^3 \mu m/s$. This calculation was repeated for different fluences along the Gaussian pulse, which is shown in Figure 6.6. It is interesting to note that the effect of fluence on the growth rate depends on which interface the growth occurs. Growth rate appears to be much more dependent on the fluence for the Air/SiO_2 interface, although this could be explained if growth at this interface reaches saturation at a lower number of irradiations. It should also be noted that while growth at the Air/SiO_2 interface accounts for the largest amount of growth at the peak fluence, the threshold fluence in which this mechanism is active is slightly lower than that for growth at the SiO_2/Si interface.

For a point of reference, the thermal growth rates for oxides need to be calculated. The most basic model for thermal oxidation of Si is the Deal-Grove model [93]. In this model, the growth time, τ_{SiO_2} is calculated as:

	t_{SiO_2} (μm)	Rate ($\mu m\ s^{-1}$)	Flux ($nm^{-2}s^{-1}$)	Flux ($nm^{-2}shot^{-1}$)
Total	8.16	8160	N/A	N/A
SiO_2/Si	2.34	2340	5.3×10^7 (O)	0.53 (O)
SiO_2/Air	5.85	5850	1.34×10^8 (Si)	1.34 (Si)

Table 6.1: Summary of the oxide thickness, growth rate, and atomic flux calculated for the oxide, oxide grown at the SiO_2/Si interface, and oxide grown at the SiO_2/Air interface. The fluxes given are for the atoms which are expected to be the diffusive species for growth at the selected interface, thus no flux was calculated for the total thickness.

$$\tau_{SiO_2} = \frac{t_{SiO_2}^2}{B} + \frac{t_{SiO_2}}{(B/A)} \tag{6.2}$$

where B is the parabolic rate constant for the initial rapid growth, and A/B is the linear rate constant for the slower growth after 100 nm. The temperature dependence of these coefficients is given by:

$$B = C_1 e^{-E_{a1}/k_b T} \tag{6.3a}$$

$$B/A = C_2 e^{-E_{a2}/k_b T} \tag{6.3b}$$

Where E_{ai} are the activation energies for the processes, C_i is the pre-exponential factor, and T is the temperature of the silicon substrate in Kelvins. The Activation energy and pre-exponential factors are dependent on the crystal orientation and whether growth is occurring in a wet or dry environment. Since silicon was irradiated in air with a relative humidity of 40%, the wet oxidation parameters will be used. While it has been shown that the substrate remains relatively cool for excitation below the single shot melt in silicon[125], a temperature just below the melting point of silicon (1680 K) will be used to err on the side of caution. Using a temperature of 1600 K, as well as the parameters for wet oxidation for (100) oriented Silicon, the total time necessary to grow 8 μ of oxide is 47.63 hours. This leads to an average

growth rate of $4.6 \times 10^{-5} \mu m/s$, which is 8 orders of magnitude lower than the ultrafast enhanced growth rate ($8.16 \times 10^{3} \mu m/s$). This is clear indication that the laser has a strong non-thermal effect on the growth rate. It should be emphasized that even though the growth rate was enhanced by many orders of magnitudes, this is likely still an underestimation of the enhancement, considering that modeling done on ultrafast excitation of Si at the single shot melt threshold show that the lattice does not reach the melt temperature.

6.3 Possible Enhancements to the Diffusion Coefficient

Now that it has been determined that the growth rate of the oxide is enhanced by at least 8 orders of magnitude, the next step is to speculate on possible ways that the laser pulse is enhancing the growth rate in the first two regimes. While no data on ultrafast growth during this regime is available, it follows from previous investigations on irradiation below the melt threshold that growth during the first regime is expected to be enhanced by the formation and diffusion of point defects. As discussed previously, this regime is limited by the reaction rate of silicon and oxygen. An increase in the point defect density weakens bonds of nearby atoms and increases the density of dangling bonds, which increases the likelihood that an oxygen species will bond with a surface atom. Alternatively, studies with nanosecond lasers have shown that photodissociation of O_2 molecules with UV lasers can enhance the growth rate by increasing the availability of atomic oxygen[12]. To dissociate O_2 molecules, a laser wavelength lower than 239 nm needs to be used. This means that in order to dissociate with 390 nm light, two-photon absorption needs to occur. No sign of a non-linear dependence on growth with fluence was observed, which is indicative that the laser is not enhancing the growth of oxides by directly dissociating O_2.

While two different mechanisms are occurring in parallel in the second regime, it is helpful to separate them and discuss them separately. The first mechanism is the

enhanced growth rate at the interface. As discussed in section 2.6, studies on the light enhanced oxidation of Silicon have been done. To briefly summarize, light is believed to enhance the diffusion of oxygen by photoinjection of hot electrons from the silicon conduction band to the SiO_2 conduction band[140]. The electrons then attach to diffusing oxygen atoms, which cause them to dissociate into O and O^-. The O^- atoms can then more easily pass through the blocking layer the interface that usually inhibits the diffusion [141]. To better get an understanding of the enhancement process, the diffusion coefficient for oxygen through the SiO_2 needs to be calculated. While previous calculation assumed wet oxidation, it has been shown that the non-thermal enhancement of the laser is larger for dry oxidation [13], thus the diffusion coefficient for molecular oxygen will be calculated instead. To calculate this, it is useful to begin with Equation 2.27:

$$\frac{dt_{ox}}{d\tau} = \frac{B/2}{A/2 + t_{ox}} \tag{6.4}$$

For sufficiently thick oxide ($A/2 << t_{ox}$), this equation reduces to:

$$\frac{dt_{ox}}{d\tau} = \frac{B}{2t_{ox}} \tag{6.5a}$$

$$t_{ox}dt_{ox} = \frac{B}{2}d\tau \tag{6.5b}$$

Assuming no initial oxide thickness, taking the integral of the above equation leads to a relationship between the final oxide thickness and the parabolic constant B:

$$t_{ox} = \sqrt{B\tau} \tag{6.6}$$

This equation resembles that for the mean displacement of a Brownian particle.

This makes sense, considering that diffusion in this regime is largely impacted by the diffusion of oxygen through the SiO_2, and B is closely related to the diffusion coefficient through equation 2.29b. Combining this equation and equation 5.10, an equation for the diffusion coefficient can be found:

$$D = \frac{t_{ox}^2 M}{2 N_s \tau} \tag{6.7}$$

Whereas before, t_{ox} is the final thickness of the oxide layer, τ is the time in which the growth occurred, M is the number of oxidant molecules incorporated per unit time ($2.2 \times 10^{22} cm^{-3}$ for dry growth), and N_s is the solubility limit for O_2 in SiO_2. To calculate the diffusion coefficient, first the solubility limit needs to be determined. The temperature for the SiO_2 layer is not expected to change significantly, thus the temperature of the oxide will be assumed to be at room temperature. It should also be noted that photoinjection should only affect the oxide up to 100 nm from the interface[141], thus τ is assumed to be the total time that the laser was actively irradiating the material (100 seconds). Using these values, the value for the diffusion coefficient of oxygen is found to be $1.596 \times 10^{-7}\ cm^2/s$ at room temperature. The diffusion coefficient for an oxygen molecule in SiO_2 at room temperature is $5.96 \times 10^{-24}\ cm^2/s$, which is an 17 orders of magnitude difference. A possible mechanism for the enhanced diffusion mechanism is the dissociation of molecular oxygen through two photon absorption. If this was the cause of the enhancement of this mechanism, then one would expect the growth rate to depend non-linearly with fluence. Figure 6.6 shows the measured growth rates for the growth rate of each mechanism. The linear relationship between this growth rate and fluence indicate that the mechanism is linear in nature, which rules out any mechanism that relies on two photon absorption. The more likely possibility then is that the diffusion of oxygen is enhanced by the defective nature of the grown oxide. The porous nature of the oxide that grows means that oxygen has a more direct pathway to reach the blocking layer, where photoinjected

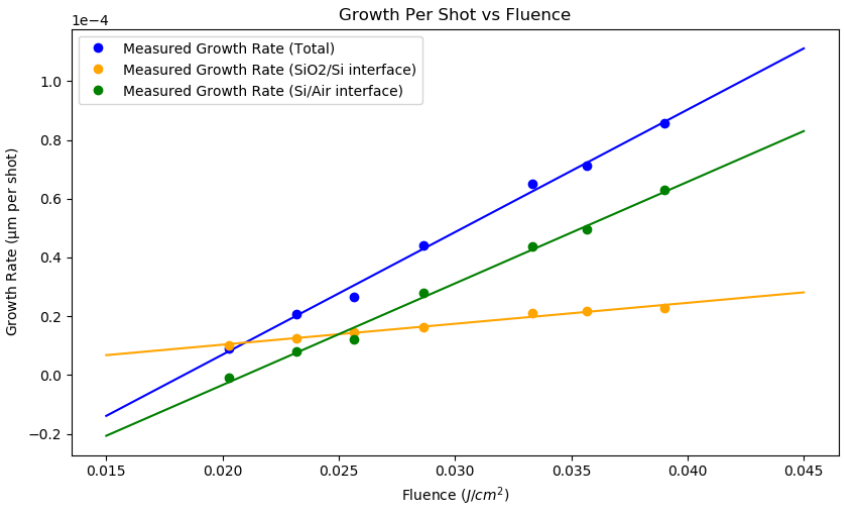

Figure 6.6: The growth per irradiation for various fluences within the irradiation area. The orange line represents the growth rate at the SiO_2/Si interface. The green line represents the growth rate at the SiO_2/Air interface. The blue line shows the total growth rate for both interfaces. At the lower fluences, growth occurs predominantly at the SiO_2/Si interface. As the fluence increases, the growth rate at the SiO_2/Air interface becomes the dominant growth.

electrons can cause the O_2 molecule to dissociate to O and O^-.

The second mechanism, which is unique to ultrafast enhanced oxide growth, is SiO_2 growth at the SiO_2/Air interface. As shown in table 6.1, the growth at this interface constitutes the largest amount of oxide growth. The growth rate at SiO_2/Air interface as a function of fluence is shown in Figure 6.6. As with the growth at the SiO_2/Si interface, this growth rate is linear, indicating that it is caused by a linear process. Growth at this interface can only occur if Si atoms are traveling to the surface of the oxide. The number of Si atoms that need to cross the SiO_2/Si interface is calculated by first determining how many Si atoms are found above a 1x1 nm^2 area, and dividing by the total number of irradiations. To calculate the atomic flux, the time for the diffusion to occur is again assumed to be 10 ns. It should be noted that this calculation represents the minimum number of Silicon atoms that need to cross this interface in order to explain the growth rate observed. The most striking aspect of the calculated rate is the similarity to the rates calculated for the arrival of

point defects at the surface during HSFL formation of GaAs irradiated with 390 nm light. This is indicative that the same ultrafast laser enhanced mass transport that was previously highlighted is also occurring in Silicon. Studies on the irradiation of Silicon with 390 nm light in vacuum have shown that at similar fluences that were used in the experiments presented in this thesis, HSFL forms due to point defect formation and diffusion [7]. It should also be noted that the fluence in which no more island formation was observed in silicon is similar to that in which the growth rate at the Air/SiO_2 interface was negligible. This is further suggestive that the enhanced point defect formation and diffusion mechanism is active during irradiation of Silicon. It should also be noted that after the Silicon crosses the interface and goes into the SiO_2 structure, it needs to further diffuse to the surface. Assuming that the SiO_2 remains in room temperature during irradiation, the diffusion coefficient for a Si interstitial in SiO_2 was calculated to be on the order of 10^{-80} cm^2/s [142]. The incredibly small value for the diffusion coefficient is due to the large activation energy (4.75 eV) for diffusion of Silicon in SiO_2. It is possible that the porous nature of the SiO_2 is enhancing the diffusion coefficient by allowing the diffusion along the surface. Another possibility that while less probable, still deserves some mention, is the possibility that the diffusion observed in the SiO_2 is primary diffusion of Si^+ ions that are desorbed by the laser [143]. Photoinjection of electrons from the Si to SiO_2 could result in a positively charged Si, which can then serve as a driving force for the desorbed Si^+ atoms. Lastly, studies have shown that enhanced diffusion of Si can occur by Si bonding with oxygen to form SiO molecules, although the observed enhancement does not appear to account for the observed rates [144]. Ultimately, more studies in order to understand the diffusion of Si through the SiO_2 need to be done. Nonetheless, there is strong evidence for the need for an enhanced Si diffusion in the Silicon to provide enough Si atoms to form the oxide observed. It should be noted that irradiation with 780 nm light did not result in the formation of structures or

oxidation upon irradiation below the melt threshold. It is likely that direct excitation of the atomic bonds, which is achieved with 390 nm light and not 780 nm light, is necessary in order for atoms to have enough mobility to create a high concentration of interstitials.

In summary, oxide growth at rates that had previously not been observed has been discussed. Furthermore, two mechanisms for the oxide rate were highlighted. One of the mechanisms is that of the oxide growing at the SiO_2/Si interface. Enhancement of the growth rate for this mechanism is believed to be caused by the photoinjection of electrons into the SiO_2, which causes the dissociation of O_2 into O and O^-, which can get through the blocking layer near the interface. The other mechanism, which appears to be unique to excitation with ultrafast laser, is growth that occurs at the SiO_2/Air interface. This growth is facilitated by the enhanced generation and diffusion of point defects in the Si, and further diffusion through the SiO_2. The exact mechanism for enhanced diffusion through the SiO_2 has yet to be determined.

CHAPTER VII

Summary

In summary, this thesis demonstrated the existence of an excited state mediated diffusion mechanism. It did so by reanalyzing the formation mechanism for HSFL that emerged upon multiple irradiations with 780 nm light in air. In this formation mechanism, irradiation causes point defect formation in the bulk. After further irradiation, these point defects migrate to the surface and form islands. These islands grow until they are large enough to scatter light. The scattered light excites SPPs, which localize the absorption of light and cause a shallow grating to form. Light then couples with this grating more efficiently, which causes another grating with a periodicity of 355 nm to emerge. Further irradiation causes a stress induced bifurcation of the 355 nm period gratings.

The mobility of the interstitial atoms as they travel from the bulk to the surface to form the initial islands and to form the HSFL structures were then calculated. This was done by determining the total number atoms per area that were arriving at the surface after every irradiation during the first 300 exposures in which the island grew, as well as the total number of atoms that had to cross the original surface every shot in order to form the HSFL structures. It was then noted that while there was 1 ms between pulses, the material was only realistically active for 10 ns after excitation. Using this assumption for how long the growth of the structures took, a flux of

2.7×10^6 $\frac{at}{nm^2 \cdot s}$ for the island formation and 1.3×10^8 $at/nm^2 \cdot s$ for HSFL formation were calculated. The discrepancy between the calculated fluxes was attributed to the possibility that internal stress of the HSFL structures, as well as surface diffusion, were not being considered. The flux values were then used alongside of Fick's first law for diffusion to calculate a diffusion coefficient for the interstitials as they diffuse for the first 10 ns after excitation. This resulted in an estimated diffusion coefficient between 6.5×10^{-8} cm^2/s and 1.61×10^{-4} cm^2/s. This value was compared with the experimentally derived diffusion coefficient of interstitials, which was calculated to be 1.91×10^{-26} cm^2/s at 930 K, which was determined to be the hottest temperature the sample could reach after excitation. This indicated that upon ultrafast excitation, the mobility of interstitials was being enhanced by roughly 20 orders of magnitude. A model for how the laser could be enhancing diffusion was then proposed: During the first ps after excitation, the non-thermal nature and high degree of electron excitation causes the interatomic binding potential to effectively disappear, meaning that atoms are free to drift with whatever thermal velocity they had at room temperature. While the regime has been determined to only last 1-2 ps before the interatomic potential begins to recover, the combination of a still weakened potential, increase in interstitial velocity due to lattice heating, and charging of the interstitials could be extending this regime past 1 ps. Alternatively, even if the ultrafast diffusion mechanism regime is not extended, those three effects could be further enhancing the diffusion for the next 10 ns or so.

Another mechanism that was investigated in this thesis was the formation of HSFL upon irradiation with 390 nm and 780 nm light in vacuum. It was found that upon irradiation with 390 nm light, HSFL with an average period of 65 nm emerged. Unlike the HSFL formation with 780 nm light in air, it was shown that this HSFL did not change periodicity throughout the formation process. It was shown through cross section SEM and AFM, that the HSFL structures were completely below the original

structures, indicating that desorption was in part driving the formation of the HSFL structures. It was then shown that upon irradiation with 780 nm light in vacuum, the structures were also below the original surface, which was indicative that pressure determined whether desorption was active or not. A model for the formation of the HSFL that includes desorption was also proposed; The laser first created point defects in the bulk, which diffused to the surface after further irradiation. Adatoms that made it to the surface were readily desorbed, leaving just the vacancies. Desorption the occurred near vacancy sites, since laser induced desorption only occurs on surface defects. As more vacancies traveled to the surface, the step edge density increases with then further increased the desorption rate. This desorption then creates a rough surface from which light can scatter an excite SPPs. These SPPs then localize the desorption mechanism in locations where the intensity was highest. A Drude-Lorentz model was used to determine the dielectric function of the material upon excitation. It was then shown that a thin film plasmonic model for the excitation of SPPs was in good agreement with the experimental evidence. Proof of this mechanism was found in TEM and NBED of individual corrugations, which showed that a single crystal spot patter was present throughout the whole corrugation. This indicated that a process where point defects were being desorbed, and interstitials were not accumulating, was likely correct.

The removal rate for the formation of the HSFL with both 780 nm and 390 nm light in vacuum were then calculated. It was found that this removal rate was roughly 6 orders of magnitude higher than expected for thermal desorption at similar temperatures. To determine whether this desorption was caused by an enhancement in point defect diffusion, results from a simplified discrete Monte Carlo model were presented. This model showed that in order to observe desorption on the scale that was experimentally observed, a flux of atoms of $0.22 \times 10^8 \ \frac{at}{cm^2 \cdot s}$ had to travel from the bulk to the surface. This flux was within one order of magnitude from the calculated

flux during the formation of HSFL with 780 nm light in air. This was evidence that the excited state diffusion mechanism was present, and in fact feeding the desorption process that ultimately caused the HSFL.

The last major result that was discussed in this thesis was the growth of oxides on silicon upon ultrafast irradiation. It was shown that after 100,000 irradiations with 390 nm light in air, an oxide with a thickness of 8.16 μm formed. The oxide growth rate was calculated, and it was determined that the growth rate was roughly 10 orders of magnitude faster than for thermally grown SiO_2. The oxide that grew was highly defective and had large voids, which appeared to fill in after further irradiations. One aspect of the laser grown oxide, which is only observed when ultrafast lasers are used, is the fact that growth occurs at both the SiO_2/Si interface, and the SiO_2/Air interface. This was determined by comparing the oxide thickness below the surface to what would be expected if the oxide was only thermally grown. The oxide thickness was then split into two different regions, the thermal like oxide and the anomalous oxide. The enhancement of the thermal like oxide growth rate was determined to be due to the breaking of the bonds in the O_2 or H_2O molecule due to photoinjection from the excited Si conduction band to the SiO_2 conduction band. The growth of the anomalous oxide was determined to be caused by interstitials coming from the Si bulk to the SiO_2/Air interface. The flux of Si atoms that was necessary in order to grow oxide with the observed thickness was then calculated to be $1.3 \times 10^8 \ \frac{at}{cm^2 \cdot s}$. This value is within one order of magnitude of the calculated fluxes for the formation of HSFL with 780 nm light in air and vacuum, and 390 nm light in vacuum. This was taken to be a strong indication that the excited state mediated diffusion mechanism was occurring in Silicon, and further enhancing the oxidation rate.

Ultimately, while three different systems and mechanisms were presented in this thesis, the most striking result is that the excited state mediated diffusion appears to be present in all of them. Even when other mechanisms such as desorption and

oxidation are observed, they are in fact being further enhanced by the excited state mediated diffusion mechanism. This shows that this mechanism is likely universal for ultrafast irradiation of semiconductors, and with further understanding, can be harnessed to modify materials in ways that were previously thought inaccessible.

CHAPTER VIII

Future Work

While this thesis has further established the point defect mechanism outlined by Abere et al [8], as well as expanded it by adding desorption and presented evidence that a point defect diffusion mechanism was also occurring, it did not solve all the questions it proposed. Like in all good science, this research resulted in creating more questions than answers. In this section, questions that still need to be answered will be stated, as well as possible pathways to discovering an answer.

8.1 Silicon and Beyond

While this thesis established a model for the formation of anomalous oxide upon ultrafast irradiation, it did not properly analyze the early stages of the formation. Thus, SEM at an earlier number of irradiations, before growth at either interface has a chance to saturate, should be done. This will allow for a better and more comprehensive measurement of the growth rate at each interface. Experiments should also focus on varying the humidity, ranging from pure dry air to a high relative humidity. Studies have shown a large difference in the growth rate for dry and wet oxidation [145], thus this would allow determination of whether the laser has an effect on the diffusion of O_2, H_2O, or both.

Another aspect the oxidation of silicon that has not been explored is understanding

the void formation during growth, as well as possible ways to eliminate them. Before this process could be applied for the formation of SiO_2 to use in devices, the oxidation process should result in high quality and defect free oxides. While it was shown that eventually the large voids get filled in, it requires almost 10 times as many irradiations, so would be beneficial to eliminate them altogether. One possible experiment that could result in the no voids forming is if a lower repetition rate is used., thus allowing the sample to completely return to its initial conditions. This could make the growth to occur more uniformly throughout the irradiation area. Another possible solution is using a flat top beam. It is possible that the defects are caused by different growth rates at different areas of the beam. Lastly, it has been shown that dry oxidation generally leads to better quality oxides [139], thus repeating this experiment without the presence of moisture could also result in a high quality oxide layer.

Another experiment that could lead to better understanding and control over the oxidation process is to irradiate the Si with a thermally grown oxide layer already on the surface. This experiment would serve various purposes. The first is the possibility of growing higher quality oxides. One possibility for the cause of these voids is the initial rough oxide that forms after a few hundred irradiations, thus mitigating this step might result in reducing the formation of voids. This experiment would also help in determining the cause of the voids. Having an already grown oxide layer, close to the thickness at which the thermal-like oxide saturates, would mean that only the anomalous oxidation grows. Thus, if voids appear due to oxide growth at different rates at each interface, this would eliminate the formation of voids. If growing a thermal oxide does result in relatively defect free structures, then one can imagine a process for the formation of high quality thick oxide where first a oxide is thermally grown, then further growth is driven by ultrafast irradiation. In order to determine the optimal oxide thickness, this experiment would have to be repeated with various initial oxide thickness. Of course, this process depends on whether the

anomalous oxide could grow over a non-native oxide in the surface. This leads to the second aspect of this experiment, which is understanding the Si diffusion through the oxide. While this thesis showed that the flux of silicon atoms into the oxide occurred through excited state mediated diffusion, it only speculated on how the silicon diffused through the SiO_2. Specifically, this thesis proposed that surface diffusion, which is significantly faster than bulk diffusion, was to blame. This experiment would then determine the validity of this hypothesis, since surface diffusion would be severely hindered by the lack of voids in the oxide.

While the mechanisms for the enhancement of oxide growth in Silicon are fascinating and open the door for the possibility of improving the manufacturing of Silicon for photonics and electronic device applications, this mechanism could lead to the ability to form other materials as well. The process outlined for the anomalous growth of oxide could also occur to enhance the growth of another material. Thus, these experiments should be carried out in the presence of another gas, and with no oxygen present. If, for example, a nitrogen or acetylene overpressure is used, it might be possible to create a SiN or SiC layer above the silicon.

This mechanism could also lead the opportunity for carbon capture from CO_2 and CO in the atmosphere. The laser could serve to break the carbon bonds separating it into C and O, then the oxygen would react with the silicon, causing oxidation. This would leave sole carbon atoms behind, which would not be in gas form anymore, and thus could be easily extracted. It might be possible to have the silicon serve to completely extract the carbon. A schematic of this process is found in figure 8.1a.

Lastly, this thesis did not investigate the silicon that remained below the oxide. Analysis should be done in this region to determine whether a large density of vacancies are present. This would serve to further verify the point defect formation and diffusion model, which predicts that vacancies are left behind. If it is found that a high density of vacancies are left, this could present a novel way to dope silicon. The

possible process would be to form a SiO_2 layer using ultrafast laser irradiation. This would create a localized area under the oxide with a high concentration of vacancies. The substrate could then be submerged in HF, which removes the oxide while having little effect on the silicon [146]. Then, after the oxide is removed, the Silicon could be placed in a high pressure chamber with the desired dopant, which could then permeate into the silicon and recombine with the vacancies. This would lead to the ability to selectively and precisely dope Silicon, allowing one to easily create complex doping architectures. Figure 8.1b shows a schematic of this process. As an alternative mechanism, the formation of the oxide with femtosecond lasers could also serve to create a blocking layer of oxide for doping purposes [147]. Instead of irradiating where doping is wanted, irradiating instead occurs where doping is not desired. Then, the sample could be irradiated with high energy dopant ions, which would go into the Silicon not protected by the oxide [147]. A schematic of this process is shown in figure 8.1.

While this thesis focused on silicon, some experiments done on the oxidation of GaAs have been done. The resulting morphology after 10,000 and 100,000 irradiations with 390 nm light at a fluence of 0.02 J/cm^2 are shown in figure 8.2. While the rates observed do not appear to be as massive as for Silicon, these result show that ultrafast oxidation of semiconductors might be an universal phenomena. Further investigation using different semiconductors need to be done, as well as studies on the quality and thickness of the oxides. This could be a pathway to easily form oxides in all semiconductors. Furthermore, it also opens the possibility for growing a large arrangement of materials on semiconductors. For example, growing GaN when irradiating GaAs in an N rich atmosphere.

8.2 Directly Measuring Transport Rates

While this thesis successfully established that anomalous diffusion was occurring, it was not able to determine the exact diffusivity of atoms upon ultrafast irradia-

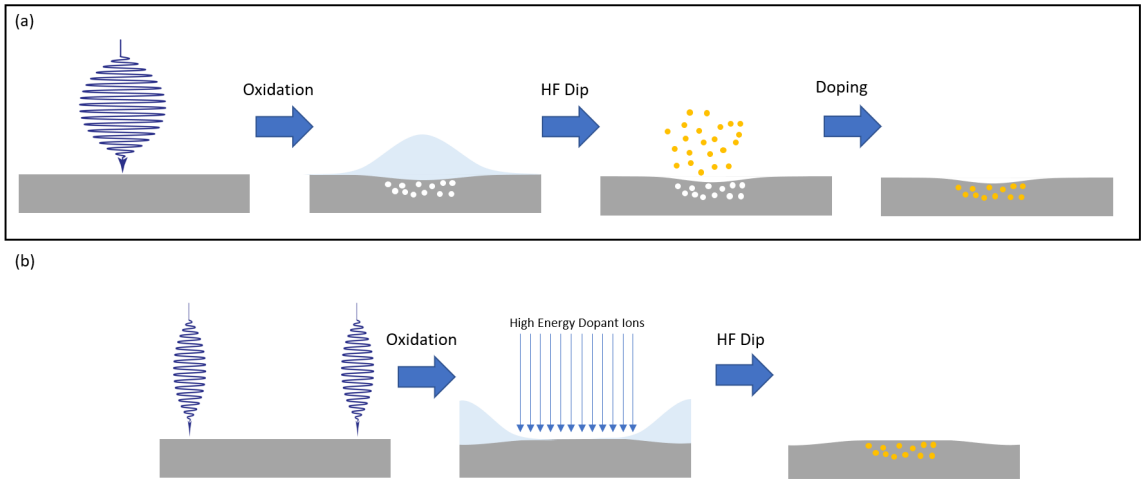

Figure 8.1: Schematic for possible ways to selectively dope Silicon. (a) The incident beam is incident where doping is desired, which causes anomalous oxidation. Since the anomalous oxide growth relies in Silicon atoms diffusing through the SiO_2, this leaves vacancies behind. The substrate is then dipped in HF, which removes the oxide while leaving the Silicon relatively untouched. The substrate is then placed in a chamber with the desired dopants. The dopants that permeate through the silicon recombine with the vacancies. (b) The incident beam is incident where doping is not desired. The oxide then acts as a protective layer for bombardment of high energy dopants. The substrate is then dipped in HF to remove the oxide. The one drawback of this technique would be that the substrate surface would be disturbed due to the fact that some of the oxide grows at the SiO_2/Si interface. This can be mitigated if a mechanism for suppressing thermal-like oxide growth can be found.

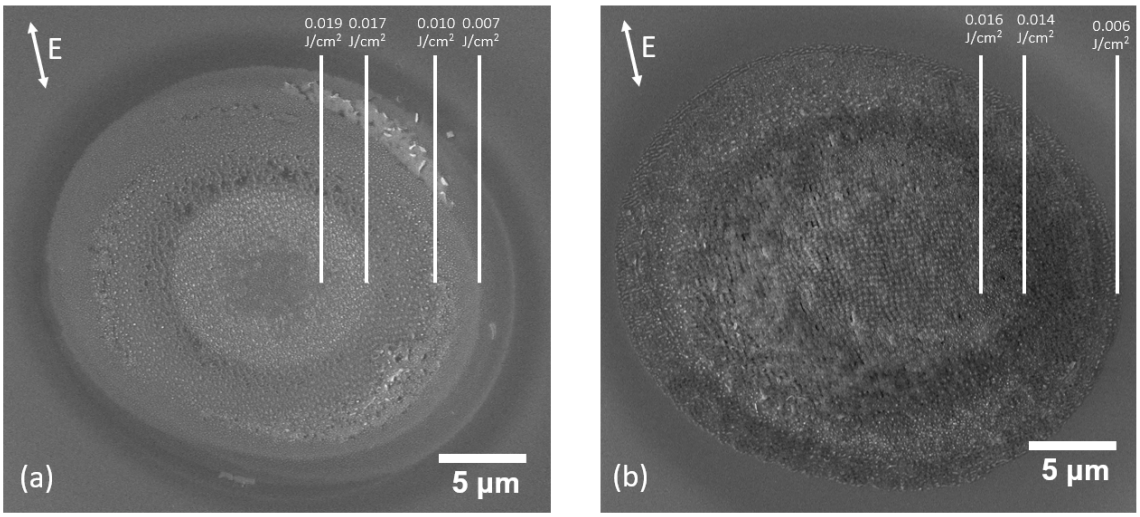

Figure 8.2: The results of irradiating GaAs with a 390 nm light at a peak fluence of 0.02 J/cm^2. (a) Shows the growth of gallium oxide after 10,000 irradiations. (b) Shows the growth of gallium oxide after 100,000 irradiations. The structures were confirmed to be oxygen rich through XEDS. While the thickness of the oxide does not appear to be as large as for Silicon oxidation, it confirms that laser enhanced oxidation is a universal process.

tion. Since all the experiments done were post-mortem, and relied on assumptions to determine the properties of the material during irradiation, only an estimation of the diffusion coefficient was able to be extracted. To better calculate the diffusion coefficient then time resolved measurements are necessary. Because of the fact that the changes in the material within a pulse, and even pulse to pulse, are so miniscule, then optical pump probe experiments are not sufficient. Three possible pathways of achieving spatial resolution of a few nm are: Electron, Scattering, X-Ray scattering, and EUV Imaging.

8.2.1 Electron Scattering

The wavelength of an electron is generally smaller than one nanometer, which make it an ideal candidate for probing of nanometer changes in the material[1]. Traditionally, a beam of electrons are formed by the use of thermionic or field[148] emission.

[1]For example, using the DeBroglie equation, the wavelength of an electron traveling at 1 kV is 0.038 nm.

The issue with these electron sources are that they result in a continuous wave of electrons, which cannot be used to extract temporal information. Thus, for electrons to be used in time resolved pump probe experiments, an electron gun that emits a pulse of electrons must be built. To create an electron pulse, an ultrafast laser pulse can be used to irradiate a negatively biased photocathode. If the energy of the photons are greater than the energy of the work function of the material used as a photocathode, then electrons can be extracted with a temporal profile similar to that of the incident pulse[149]. The electrons would then be accelerated towards a gold or copper grid, which would be grounded to serve as an anode and to attract the electrons. As the electrons travel, space charge effects broaden the pulse spatially and temporally. To have a better wavefront, a pinhole can be placed in the path of the electrons to remove electrons whose momentum direction differs from the propagation direction of the central electrons. A schematic of this gun with an overlay of COMSOL results showing the behavior of electrons, is shown in Figure 8.3a. Figure 8.3b shows the gun in action, showing that electrons can be reliably generated. The next step would then be to determine time zero, which is the delay in which the electron probe and the photon pump overlap in space and time. In optical pump probe, this is often done by using a second harmonic crystal and changing the delay until a second harmonic signal is obtained. With an electron beam, the second harmonic crystal can be replaced with a sharp metal tip. When the photon pulse is incident on the tip, a cloud of electrons are released after irradiation, which lasts for a few ps[150]. If both the photon and electron pulses are overlapped in time, then the electron gas would cause a disturbance on the trajectory of the electron beam as it passes. Since this disturbance only occurs when both pulses arrive at the tip at the same time, this serves as a reliable way to find time zero.

The expected result of this experiment should be similar to that of RHEED oscillation in MBE growth [151]. During the formation of islands on the surface, the

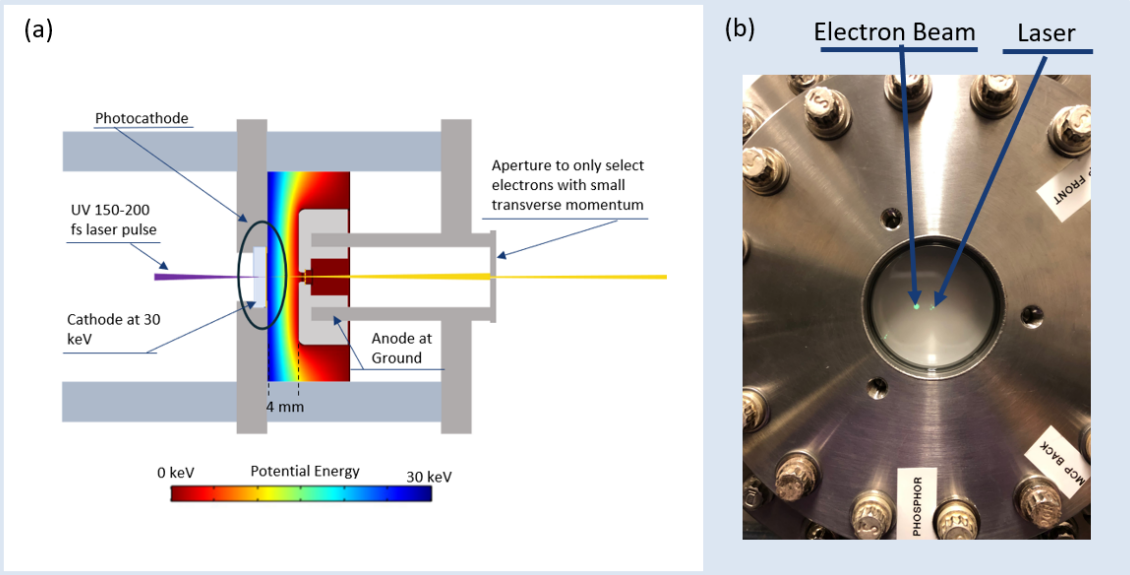

Figure 8.3: (a) Schematic of electron gun to be used in electron scattering experiments. The laser pulse is incident on a photocathode at -30 kV. This causes the emission of electrons, which are accelerated towards the anode at ground. The electrons are then incident on an aperture. (b) Picture showing working electron beam.

specular beam should lose intensity as the coverage of islands increases. The slope of the change in intensity of the oscillator would then tell how fast the islands are growing, which is essentially a direct measurement of the arrival rate or diffusion rate. This can then be used to compare with the calculated numbers, to ensure their validity.

8.2.2 X-Ray Scattering

Another experiment, which is analogous to the electron scattering experiment, is using an x-ray beam instead of a UV-VIS or electron beam. X-Rays are photon with energies greater than 100 eV, which means that have wavelengths smaller than a nanometer. This means that x-rays have the resolution to observe the minute changes in the growth of the HSFL. While most x-ray sources do not have the temporal resolution to observe changes in the picosecond regime, high intensity and high powered lasers can be used to create ultrafast x-ray pulses [152]. The laser would then, just as

with electron scattering, serve as the x-ray source and pump source. The benefits of this experiment is that, since a high powered laser is needed to generate x-rays, then the laser has enough energy to spread the beam into a large area, which makes the experiment easier to complete.

8.2.3 Extreme Ultraviolet Laser

Lastly, another experiment where the small changes in the growth can be observed is by using a High Harmonic driven Extreme Ultraviolet laser (EUV). These lasers can reach wavelengths on the order of a few nanometers, which mean that have the spatial resolution necessary. The simplest experiment would be then to use these lasers to do pump probe reflectivity. More interestingly though, would be to use these lasers to image the structures during growth. EUV pulses have been used to image nanostructures with similar resolution to that of an SEM [153]. This is accomplished by probing different parts of the region of interest, and using an algorithm to take the diffracted signal and build an image. While temporal information might be lost using this method, getting an image of the structures during each step could lead to better understand of the growth process.

8.3 Better Understanding of Material Response

8.3.1 Wavelength and Activation Energy

This thesis showed that there was a large difference between the resulting structure after irradiation with 390 nm light and 780 nm light. This then leaves the question of what occurs when irradiating at wavelengths beyond 390 nm and 780 nm, as well as between the two wavelengths. Observing the emergent structures as a function of wavelength would allow better understanding of how the dielectric function behaves, as well as whether the different mythologies observed have a specific wavelength in

which they begin occurring. Determining the wavelength at which an effect is first observed would allow associating that effect with activation energies of specific processes in the material. Likewise, doing a wavelength dependent study on the oxide growth would serve the same purpose. Studies have shown that there is a large difference in the enhancement between irradiations at different wavelengths[13]. In this study, these differences were then used to determine the exact processes for the formation of the oxide. Thus, replicating this study on the formation of ultrafast lasers would allow for the determination of specific processes that are the cause of the enhanced oxidation

8.3.2 Dielectric Function Measurements

Further understanding of how the bandgap behaves during and after irradiation needs to also be gained. Specifically, what effect the pump wavelength has during the bandgap collapse regime. To obtain information of how the bandgap behaves after excitation, a two-angle reflectivity experiment, similar to those done by Glezer et al [3] should be done. It is likely that the initial electron configuration, which is dependent on the incident wavelength, might have a significant role on the response of the material, yet these measurements have been contained to a single wavelength.

Another aspect of the of the dielectric function that needs to be considered is the effect that point defect and roughness after multiple irradiations have on the dielectric function. The formation of point defects in the bulk and surface have a non-negligible effect on the dielectric function[154], even more so at high densities. This should be explored both computationally and experimentally. A white light source with frequencies in the visible to infrared range could be used to directly measure changes in the dielectric function[26] and band gap. These changes could then be verified by recreating the defected lattice with DFT to calculate the band structure. Once there is better understanding of the transient and non-transient effects of laser irradiation,

then the model used to calculated the excited dielectric function[8] can be extended.

The modeling of the dielectric function should then be combined with better understanding of the SPP coupling mechanism. While models exist that have proven useful for the prediction of HSFL, as of now, no model can explain all the cases. One aspect that has not been taken into account is the exponentially decreasing dielectric function due to the exponentially decreasing laser energy density as the light propagates through the material. The models in the literature generally assume that there is a distinct boundary between the excited and non-excited volume [77]. Doing COMSOL modeling of the SPP excitation with a varying dielectric function would then show whether the existing models are accurate enough, or whether these models should be expanded. The COMSOL results could then be experimentally verified by directly measuring the SPP dispersion curve, as done by Kitson et al[76]. This would provide a challenge, as the experiment would have to be done while the material is still metal-like. In other words, would require a fairly complex pump probe measurement technique. Since this experiment could be done dynamically, then it could also serve to determine how the SPP dispersion curve changes throughout multiple irradiations.

APPENDICES

APPENDIX A

Goals

A.1 Establishing the role of desorption on the formation of periodic structures

Analysis on the structures formed after irradiation of GaAs with both 390 nm and 780 nm light in vacuum showed that these structures were below the original surface. This indicates that material removal, not material reorganization, was driving the formation. TEM was done, which showed that the remaining structure was single crystal, with no sign of melting or accumulation of point defects. The fact that melting was not observed, even though the removal rate could not be explained with thermal desorption below melt, suggests that the desorption was caused by non-thermal effects. Since no point defects were also observed, it was also suggested that point defect occurred at interstitial and kink sites on the surface, which left only vacancies behind. This latter point is supported by the fact that no laser desorption of GaAs has been observed from pristine surfaces.

It was also found that the structures formed upon irradiation with 780 nm light in both vacuum and air were strikingly similar once fully formed. The only difference

that was observed was that the structures formed after irradiating in air were above the original surface, while the structures formed after irradiating in vacuum were below the original surface. This was indicative that lowering the pressure is what activates the desorption process. It was also shown that when desorption was active, even though the finalized structures looked the same, the evolution of the morphology was different. It was then suggested that the initial structures were formed by desorption, but a strain induced bifurcation of the initial structures were to blame for the last step of the HSFL formation.

A.2 Demonstrating that an enhanced mass transport mechanism occurs upon irradiation with ultrafast laser pulses in GaAs

The growth of HSFL upon irradiation with 780 nm light in air was reexamined to estimate the diffusion coefficient of the atoms that make up the corrugation. A cross section image was used to calculate the number of atoms that cross the original surface every shot. In order to calculate a flux, it was estimated that the material is active for only 10 ns after irradiation. This time was chosen because it corresponds to the time where a high number of electrons are in a Fermi-Dirac distribution in the conduction band, and the material is still at an elevated temperature. From this flux, Fick's law was used to calculate a diffusion coefficient. This diffusion coefficient many orders of magnitude higher than bulk desorption, and roughly 4 orders of magnitude higher than for surface desorption. While the calculated value is an estimation, and cannot be taken as is, the orders of magnitude differences are enough to strongly suggest that laser excitation is having an enhancement. Further evidence of the excited state mediated diffusion is found in the removal rate calculations for irradiation of GaAs in vacuum. It was shown that in order to have the removal rate observed, a flux of interstitials and vacancies on the same order of magnitude as for the formation of HSFL with 780 nm light was necessary.

A.3 Presenting a model for the growth of anomalous SiO_2

It was shown that a thick layer of oxide grew upon irradiation with 390 nm light at ambient conditions. The growth rate was found to be dependent on the fluence, with a sharp increase in the growth rate when near the single shit melt threshold of Silicon. Cross section SEM micrographs showed that the oxide had large voids, which slowly fill as the number of irradiations increased. The cross section SEM also showed that the oxide did not follow the same proportionality between oxide above and below the original surface as thermally grown oxide. While thermal models for oxide growth predict that 47% of the total oxide thickness should be below the original surface, it was found that only 13% of the total oxide thickness was below the original surface. It suggested that oxide was growing at the SiO_2/Si interface, just as for thermally grown oxide, but also at the SiO_2/Air interface. The mechanism for the enhancement was then determined to be different for each interface. For the SiO_2/Si interface, enhancement is more likely due to the photodissociation of oxygen atoms. Enhancement of growth at the SiO_2/Air interface, it was suggested that diffusion of Si atoms through the oxide, which could then bond with the oxygen atoms, caused the growth at this interface. The flux of Silicon atoms that were required to cross the original surface in order to have the observed growth rate was then calculated. It was found that this flux rate was on the same order of magnitude as the flux rate for irradiation in GaAs, suggesting that a similar point defect diffusion mechanism was occurring in Silicon as well.

A.4 Demonstrating that an excited state mediated diffusion mechanism is an universal mechanism that occurs upon ultrafast irradiation of semiconductors

The previous experiments have shown that a point defect formation and diffusion mechanism occur when irradiating below the single shot melt threshold. Both the 390 nm and 780 nm irradiation results in GaAs, as well as the 390 nm irradiation in Silicon have shown evidence that an excited state mediated mechanism for diffusion. This is suggestive that the mechanism itself is universal to all semiconductors, and not exclusive to GaAs. The one common denominator between the irradiation conditions was found to be that the fluence was just below the single melt threshold, where the band gap closure leads to weakening of the interatomic potential. From this observation, a possible mechanism for this enhanced diffusion was proposed. The basis of this mechanism involved the lowering of the activation energy to break the bonds required for an interstitial to hop from one site to another. It was pointed out that while this mechanism has not been applied to diffusion, this weakening of the interatomic potential leads to the formation of point defects. A recombination stimulated diffusion mechanism, further enhanced by the weakening of the interatomic, was also proposed as a possible enhancement.

APPENDIX B

Laser Troubleshooting

In this appendix, possible issues that could arise with the operation of the Laser will be discussed, and possible fixes with be described.

B.1 Seed Laser

If the laser is not outputting any light, or the laser beam is unstable during operation, then it is possible that the seed laser is either not operating properly, or is not mode locking. The first thing to check is the panel on the back of the laser, which is where the laser diode for the fiber seed laser is located. Make sure that it reads a power of 145 mW or higher, and that the two LEDs are turned on. If power lower than 145 mW is observed, then likely then there are some electronic issues, and it is best to contact the manufacturer. If the LED labeled 2 is turned off, then that means that the oven for the PPNL is not reaching high enough temperatures. To verify, use the port on the side of the laser and measure the resistance from the port labeled "PPNL Oven Monitor". The resistance measurement should read 1-3 kOhm for standard operation, but >10 kOhm if the oven is not functioning at all. If this is the case, make sure that all the connections in the fiber laser are properly attached, otherwise contact Clark-MXR for further assistance.

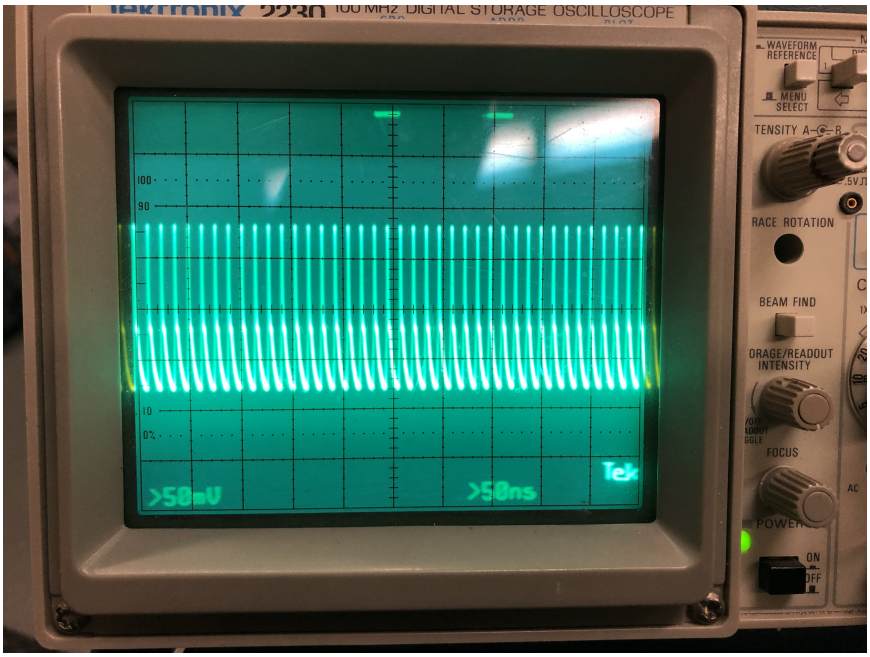

Figure B.1: Mode-locking signal, as seen in the Tektronix 2230 Analog Oscilloscope. Note the shape of the individual peaks.

If the seed laser appears to be functioning correctly (All LEDs on, reading 145 mW or more power) but there is still unstable output or no lasing, then the seed laser could be having trouble mode-locking. First check the mode-locking signal. Connect the analog oscilloscope to the "Mode-Locking Monitor" on the side of the laser without using the low-pass filter. The signal on the oscilloscope should look like in Figure B.1.

If it does not, then there are a few simple things that must be checked. First, make sure the pump is on, and has been operating at 20∘C for at least 24 hours. Also make sure that the room temperature is within two degrees Celsius of the usual operating temperature. If the pump is on, and the temperature of the lab is correct, yet the mode-locking does not look like in Figure B.1, then the free space optics may be adjusted. Instructions on how to do this can be found in the CPA-2001 User manual, under the troubleshooting section.

B.2 CPA Regen Alignment

If the laser power is unstable, or the power is not high enough, then a possible culprit is the alignment of the regen. Only minor adjustments of the injection should be done, since if the injection is further misaligned then recovering the alignment becomes extremely difficult. Make sure you do not touch the contacts on the Pockels cell, they are exposed and will shock you if touched. Before alignment, make sure the oscilloscope is showing the output of the regen diode. To align, first locate the output coupler in the regen, labeled A in figure B.2. Adjust the horizontal screw to make the individual peaks in the oscilloscope trace higher, as well as moving the peak of the envelope earlier in time. Do the same for the vertical adjustment screw. Next, locate the pump-thru mirror, labeled B in figure B.2. Adjust the horizontal screw while observing oscilloscope, then adjust the vertical screw. Repeat the adjustment of the output coupler and the pump-thru as necessary. After these adjustments are done, then in order to recover previous power the injection (labeled C in figure B.2) and the delays need to be readjusted to maximize output power.

B.3 Flash Lamp Replacement

If the power of the pump laser is lower than 5 W and the lamp current is set to be higher than 29 mA, the flash lamp needs replacement. To do this, first put on gloves to not damage the flash lamp, and goggles in case the flash lamp explodes. Make sure the laser is completely turned off, and the pump is turned off[1]. Remove the top plate of the flash lamp chassis and set it down on top of the laser. It will drip water, so be careful where it is placed. Carefully, unscrew the two screws on the side of the flash lamp holder. Remove one of the L Brackets from either side, and then carefully remove the flash lamp tube using the other L Bracket. Make a note of the orientation

[1]Note: This is referring to the pump for the regen and the flash lamp. The small pump for the seed laser needs to remain on

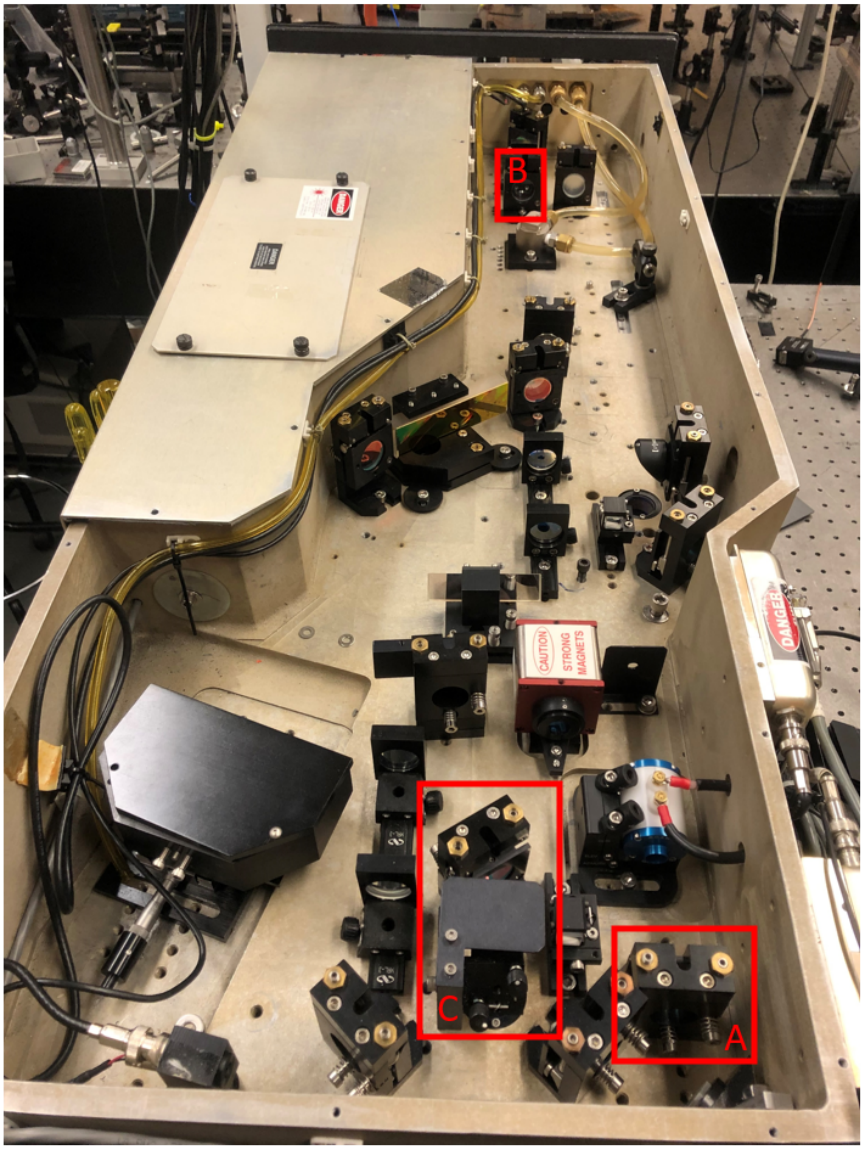

Figure B.2: Picture of the laser. Optical mounts to be adjusted are highlighted. (a) Output Coupler. (b) Pump-Thru Mirror. (c) Seed Laser Injection Mirrors.

of the flash lamp before removing, since the orientation matters. Carefully place the burnt flash lamp somewhere safe. Grab the new flash lamp bulb, and carefully use the L Bracket to insert it back into the chassis in the same orientation as before. Then place the other L-Bracket to hold the flash lamp in place. Put back the screws to attack the L-Brackets to the chassis. Next, make sure that the O-Ring is correctly placed, then re-place the top plate back on top of the bottom plate. Make sure that there are no openings on the sides. Screw the top plate back on in a shoelace pattern. Make sure again that there are still no openings on the sides. Turn on the pump, and inspect the flash lamp chassis for any leaks. If there are no leaks, turn the pump off and on a few times, then keep the pump running for around 15 minutes in order to remove air bubbles from the pump line. Now, make sure the flash lamp current is set to minimum, and then turn on the flash lamp. Observe the chassis for any signs of air bubbles, and wait until those air bubbles are not present anymore before increasing the current.

Once no air bubbles are present, slowly increase the current over the next 20 minutes until the current is at 24 mA. Open all the shutters and the HV voltage supply for the Q-Switch. Carefully, place the power meter right at the output of the green laser. Increase the current further until the power reads greater than 7 W, or the current is at 26 mA. If the current is at 26 mA and the power is less than 6 W, then keep it as it. The laser will still function but at a much lower power. Alignment of the pump laser or replacement of the LBO crystal might be needed. If the current is at 26 mW and the power is greater than 6 W, then increase it a bit further to try and reach 7 W but do not get past 27.5 mA. Now, carefully remove the power meter[2]. Adjust the delays on the DT 505, as well as do minor adjustments of the current (Less than 0.5 mA adjustments) in order to recover the timing. The pulse train, as seen on the oscilloscope, should resemble Figure B.3

[2]Some of the mirror holders can be misaligned if bumped with the power meter

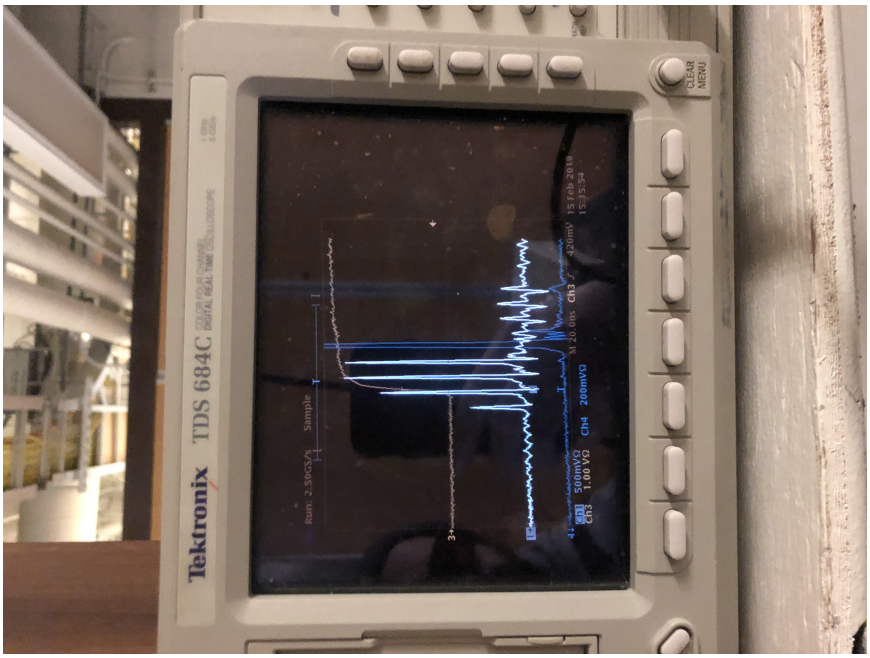

Figure B.3: Pulse Train of the regen. Note how there are only four peaks present. Also note how the pulse is being dumped right after the peak envelope.

APPENDIX C

Electron Gun Setup

In this appendix, information on how to properly prepare the electron gun vacuum chamber, how to turn on the microchannel plates (MCP) for the first time, how to align the third harmonic crystals, and how prepare the photocathode will be discussed.

C.1 Preparing the Vacuum Chamber

In order for the electron gun to be turned on without issues, the vacuum chamber needs to be pumped down to at least $10^{-7}\ Torr$. To do this, first make sure the valve between the roughing pump and the turbo pump is open, then turn on the roughing pump. After the pressure for the roughing line reaches roughly $1 \times 10^{0}\ Torr$, make sure the gate between the turbo pump and the chamber is open then turn on the vacuum pump. After 20-30 minutes, check the pressure using the ion gauge. If the pressure is close to $1 \times 10^{-7}\ Torr$, then turn on the ion pump. Keep both pump running until the ion pump has finished out-gassing. Once the ion pump is stabilized, turn off the turbo pump. The chamber should then reach at the very least a pressure of $10^{-8}\ Torr$ unless there is a leak present. The vacuum chamber should remain at a low pressure, since the MCPs are hygroscopic and can be damaged.

C.2 Microchannel Plate Setup and Operation

If the vacuum chamber has been opened, then the MCPs need to be turned on properly or they can be damaged. Information on how to do this can be found in the manual for the detector, but will be briefly summarized here. First, make sure the two power supplies are connected to the phosphor screen and the back MCP channel, and the front MCP channel is grounded. Then, make sure that the vacuum is at least 2×10^6 $Torr$, and that the MCPs have outgassed for at least 15 hours. Slowly apply 1000 V to the phosphor screen, while making sure that the current measurement on the power supply is not fluctuating. Then apply 800-1000 V across the MCPs for 30 minutes. Raise the phosphor screen an additional 1000 V in 100 V steps, and leave on for 30 minutes. Raise the potential across the MCP an additional 200 V, and leave on for 30 minutes. Repeat the last two steps once more, to get the phosphor screen to 3000 V and the MCP to 1400 V. Raise the MCP an additional 200 V and leave on for 30 minutes, then an additional 200 V and leave on for another 30 minutes. If extremely bright spots are observed, this could be due to dust or moisture, so leave on until the spots subside. Then raise the phosphor screen an additional 500 V, and leave on for 30 minutes. Then increase the MCP voltage in increments of 50 volts per 15 minutes until the desired voltage is reached. Do not exceed 2000 V across the MCPs. Raise the phosphor screen volatge in increments of 100 V per 15 minutes until the desired voltage is reached. Do not exceed 5000 V across the phosphor screen. Make sure that the total electron power does not excite 1/2 watt across the MCPs. This should only be necessary the first time the MCPs are turned on after they have been exposed to air.

C.3 Third Harmonic Crystal Alignment

The third harmonic of the 780 nm light laser needs to be generated in order to excite the photocathode. In order to do this, a third harmonic generation kit needs to be used. This kit includes two differently cut beta barium borate (BBO) crystals, a half-wave plate (HP), and a group velocity delay (GVD) compensation calcite plate (CP). First, the BBO crystal for second harmonic generation needs to be aligned. Use a power meter or photodiode, and follow the directions described in Chapter 3.5 to align the crystal. Then, the HP needs to be aligned because the second harmonic signal is perpendicularly polarized compared to the fundamental signal. Rotate the HP until the polarization of both beams matches. Next, because of GVD, the fundamental and second harmonic pulses are not overlapped in time, so the CP needs to be rotated until they are. The best way to do this is to insert the other BBO crystal, and rotate the calcite crystal until the third harmonic is observed. Then, the second BBO crystal needs to be properly aligned to maximize the signal. Once the second BBO crystal is aligned, return to the CP and HP and continue iterating until maximum power in the third harmonic is achieved. To separate the third harmonic from the fundamental and second harmonic, the harmonic separators should be used to only reflect the third harmonic light.

C.4 Photocathode Preparation

The cathode needs to be properly prepared in order to achieve high ratio between incident fluence and output electron current. The photocathode consists of a polished 1/2 inch fused silica window that is then sputtered with 15 nm of gold. To prepare for sputtering, first clean a 1/2 inch fused silica window using a detergent, and rinse with deionized (DI) water. Then, clean the window in a sonic bath of acetone, then methanol, and finally ethanol. The window should then be dried using extra-dry

nitrogen. The window is now ready to be sputtered. The sputter system in the Lurie Nanofabrication Facility (LNF) was be used for this. First, a 2 nm thick wetting layer of titanium should be sputtered in order to make sure the gold properly sticks to the window. Once the wetting layer is grown, then the gold can be sputtered. The thickness of the gold can be anywhere between 10-20 nm, although we found 15 nm was the best thickness for our uses.

APPENDIX D

Excited State Dielectric Function Code

This code calculates the excited state dielectric function of a material upon ultrafast irradiation. It does so by first calculating excited electron density for a given fluence. This electron density is then used to calculate the excited state plasma frequency. This is then used to determine the Drude-like free electron contribution to the dielectric function. For the ground state dielectric function, the values determined by Glezer et al[3] are used to fit a Lorentz two-oscillator model. Then, the excited state dielectric function is calculated by summing the Lorentz term with the Drude term. The only inputs necessary are the irradiation parameters, the linear and non-linear absorption coefficients, and the effective electron and hole masses.

```
import numpy as np
import matplotlib.pyplot as plt
from scipy.optimize import curve_fit


#Fixed Parameters:
f1 = 0.16
f2 = 0.84
gamma = 1e15
```

```
wplrt = 13.7


#Constants:
hbar = 6.5821 * 10**(-16)
h = 4.14*10**(-15)
wpl = 13.7 #Room Temperature Plasma Frequency of GaAs
c = 2.998*10**8 #Speed of light in m/s
cnm = 2.998*10**17 #Speed of light in nm/s
absDepth = 14 #Absoprtion depth in nm
ec = -1.602*10**(-19) #Electron Charge
eme = 0.067 #Effective Mass coefficient for electrons in GaAs
emh = 0.47 #Effective Mass coefficient for holes in GaAs
emoptST = 0.18 #Eff Mass From Sokolowski-Tinten for Silicon
me = 9.109*10**(-31) #Mass Electron
e0 = 8.85*10**(-12) #Vacuum Dielectric



#Room Temperature Lorentz Parameters:
w1rt = 3.10
w2rt = 4.77
v1rt = 0.73
v2rt = 1.9


#Calculate effective mass
ml = 1.9 #Langitudal Mass of GaAS (L valley)
mt = 0.075 #Transverse Mass of GaAs (L valley)
```

```
mlh = 0.085 #Light Hole Mass of GaAs
mhh = 0.50 #Heavy Hole Mass of GaAs

#Mass of Holes Calculation
mh = (mlh**(3/2) + mhh**(3/2))/(np.sqrt(mlh) + np.sqrt(mhh))

#Mass of Electrons Calculation
mel = ((1/3)*((2/mt) + (1/ml)))**(-1)



print("Effective Electron Mass: " + str(mel))
print("Effective Hole Mass: " + str(mh))




#Excitation Parameters for GaAs 780
fluence = 0.065 #Fluence in J/cm^2
lambd = 780 #wavelength of light in nm
lambdE = (cnm*h)/(lambd) #Energy of given wavelength
Ref = 0.33
fluenceRefl = fluence*(1-Ref) #Calculate reflection
fluenceRefleV = fluenceRefl * 6.242e18
absCoeff = 14486 #Absorption coefficient in cm-1
absCoeffNL = 2.2e-7 #Nonlinear Absorption coefficient cm/W
t0 = 150e-15
mel = 0.067
```

```
"""
#Excitation Parameters for GaAs 390
fluence = 0.018 #Fluence in J/cm^2
lambd = 390 #wavelength of light in nm
lambdE = (cnm*h)/(lambd) #Energy of given wavelength
Ref = 0.47
fluenceRefl = fluence*(1-Ref) #Calculate reflection
fluenceRefleV = fluenceRefl * 6.242e18
absCoeff = 7.28e5 #Absorption coefficient in cm-1
absCoeffNL = 0 #cm/W
t0 = 150e-15
"""

,,,
#Excitation Parameters for Si  (Sokolowski Tinten Paper)
fluence = np.linspace(0.01, 0.5, 1000) #Fluence in J/cm^2
lambd = 625 #wavelength of light in nm
lambdE = (cnm*h)/(lambd) #Energy of given wavelength
Ref = 0.2
fluenceRefl = fluence*(1-Ref) #Calculate reflection
fluenceRefleV = fluenceRefl * 6.242e18
absCoeff = 3.42e3 #Absorption coefficient in cm-1
absCoeffNL = 0.5e-7 #cm/W
t0 = 100e-15
,,,
```

```
#Calculate optical effective mass
mopt = 1/((1/mh) + (1/mel))
print("Effective Optical Mass: " + str(mopt))


# Calculate the excited free Electron density (cm^-3)
ne = (fluenceRefleV/lambdE)*(absCoeff +
     (absCoeffNL*fluenceRefl)/(2*np.sqrt(2*np.pi)*t0))
print("Excited Electron Density: " + str(ne))
#ne = 1e21

plt.loglog(fluence, ne)
plt.show()
# convert excited free electron density  to (m^-3)
nem = ne * 1e6

#Excited plasma frequency
excwpl = np.sqrt((nem * ec**2)/(me*mopt*e0))
ewplEnergy = hbar*excwpl

print("Excited Plasma Energy: " + str(ewplEnergy))

#Excited Plasma Frequency
wp = ewplEnergy
#plrt = ewplEnergy
```

```
#Create Drude Lorentz function.
def DrudeLorentz(w,w1,w2,v1,v2):
    A_osc = f1/(w1**2 - w**2 + 1j*w*v1)
    B_osc = f2/(w2**2 - w**2 + 1j*w*v2)
    drude = wp**2/(w*(w + 1j*hbar*gamma))
    #drude = (wp**2)/(w*(w* + (hbar*gamma)**2))
    return (1 + (wplrt**2) * (A_osc + B_osc) - drude)

#Create Drude Lorentz Function.
#This is only the real part
#Comment out drude term if ussing DrudeTermReal function
def DrudeLorentzReal(w,w1,w2,v1,v2):
    A_osc = f1*(w1**2 - w**2)/((w1**2 - w**2)**2 + w**2 * v1**2)
    B_osc = f2*(w2**2 - w**2)/((w2**2 - w**2)**2 + w**2 * v2**2)
    #drude = (wp**2/(w*(w**2 + (hbar*gamma)**2)))* w
    return 1 + (wplrt**2) * (A_osc + B_osc)# - drude

#Create Drude Lorentz Function.
#This is only the real part
#Comment out drude term if ussing DrudeTermReal function
def DrudeLorentzImag(w,w1,w2,v1,v2):
    A_osc = f1/((w1**2 - w**2)**2 + w**2 * v1**2)
    B_osc = f2/((w2**2 - w**2)**2 + w**2 * v2**2)
    #drude = (wp**2/(w*(w**2 + (hbar*gamma)**2)))* (-1*hbar*gamma)
    return (wplrt**2)*w*(v1*A_osc + v2*B_osc)# - drude

#Create Real Drude Term Function
```

```
def DrudeTermReal(w):
    return (wp**2/(w*(w**2 + (hbar*gamma)**2)))* w

#Create Imaginary Drude Term Function
def DrudeTermImag(w):
    return (wp**2/(w*(w**2 + (hbar*gamma)**2)))* (-1*hbar*gamma)



energies = np.linspace(0.1, 6, 10000)


#Use Mazur's Data to Fit Lorentz Terms
wMazur = np.array([1.59, 3.18, 3.1, 4.13])
yReal = np.array([13.657,11.102, 14.694, 9.9135])
yImag = np.array([0.66477,18.191, 19.910, 14.943])

def funcBoth(w,w1,w2,v1,v2):
    y_real = DrudeLorentzReal(w,w1,w2,v1,v2)
    y_imag = DrudeLorentzImag(w,w1,w2,v1,v2)
    return np.hstack([y_real, y_imag])

yBoth = np.hstack([yReal,yImag])
initGuess = [3.14,4.75,0.68,1.6]
bounds = [[2,2.5,0.5,0.5], [5,5,6,6]]

#Calculate Lorentz Parameters
```

```
poptBoth, pcovBoth = curve_fit(funcBoth, wMazur, yBoth,
                               p0=initGuess, maxfev = 5000)


n2 = -7.8 * 10**(-14) #cm^2/W
I = 0.018*0.5/200e-15
n0 = 4.0257

#Determine Kerr Effect
#Not significant enough to include
delKerr = 2*n0*n2*I + (n2*I)**2

#Calculate values of Drude
realDRT = DrudeLorentzReal(energies, *poptBoth)
                - DrudeTermReal(energies)
imagDRT = DrudeLorentzImag(energies, *poptBoth)
                - DrudeTermImag(energies)

#Do The Plotting
plt.figure("Room Temperature GaAs")
plt.plot(energies,realDRT, label="Real")
plt.plot(energies,imagDRT, label="Imaginary")
#plt.plot(wMazur, yReal, 'ko')
#plt.plot(wMazur, yImag, 'ko')
#plt.plot(energies,
        np.real(DrudeLorentz(energies,2.85, 4.4, 1.7, 5.25)),
        linestyle='dashed')
#plt.plot(energies,
```

```
        np.imag(DrudeLorentz(energies,2.85, 4.4, 1.7, 5.25))*-1,
        linestyle='dashed')
plt.legend()
plt.hlines(0, 0, 6)
plt.hlines(-1, 0, 6, linestyle = 'dashed',
            color='grey', linewidth=0.75)
plt.vlines(1.59, -100,50, linestyle = 'dotted',
            color='red', alpha=0.5)
plt.vlines(3.18, -100,50, linestyle = 'dotted',
            color='blue', alpha=0.5)
plt.xlim(0,6)
plt.ylim(-20, 35)
plt.title("Dielectric Function at 0.018 $J/cm^2$")
plt.xlabel("Energy (eV)")
plt.ylabel("Dielectric Function")
plt.savefig('ExcitedDielecRT', dpi=2000)
plt.show()
```

APPENDIX E

Thin Film Plasmonic Model Code

This code is used to solve the thin film plasmonic model to predict HSFL wavelength. The geometry used has the variables e1 as the excited thin film dielectric function, e2 as the dielectric function of air, and e3 as the dielectric function of the unexcited material. The code solves for the wave vector of the SPP traveling in the thin film, then displays the wavelength of said SPP. The inputs for this are irradiation parameters, the dielectric function of the material of interest, and estimation of the electron density for a given fluence. This latter value can be calculated using the "Excited State Dielectric Function" code.

```
%Constants
hbar = 6.5821 * 10^(-16);
me = 9.109*10^(-31);
ec = -1.602*10^(-19);
e0 = 8.85*10^(-12);



% %Si experiment reproduction
% lambd = 625; %nm$
```

```
% k0 = 2*pi/lambd;
% t = 10;
% mopt = 0.18;
% gamma = 1.1*10^(15);
% w = 1.984; %Photon Energy
% e2 = 1.0; %Air Dielectric Constant
% e3 = complex(3.8885, 0.0017)^2; %Si dielectric function @625nm
% %end



% %GaAs experiment
% lambd = 390; %nm$
% k0 = 2*pi/lambd;
% t = 10;
% mopt = 0.0854;
% %mopt = 0.067
% %mopt = 1.2*mopt
% gamma = 1.1*10^(15);
% w = 3.18 %Photon Energy
% %w = 1.59;
% e2 = 1; %Air Dielectric Constant
% e3 = complex(4.1240, 2.2620)^2; %GaAs dielectric function @390nm
% %end

%Set the Electron Density
Ne = linspace(6*10^21, 5*10^22, 100);
Ne = [8.7e21];
```

```
Ne = Ne * 1e6;


b_solArr = [];


%Thin Film Calculation
for n = 1:length(Ne)
    %Calculate Excited Plasma Frequency
    excwpl = sqrt((Ne(n) * ec^2)/(me*mopt*e0));
    %Convert plasma frequency to energy
    wp = excwpl*hbar;
    %Calculate Drude Terms
    drude = wp^2/(w*(w + 1i*hbar*gamma));
    drudeReal = (wp^2/(w*(w^2 + (hbar*gamma)^2)))* w;
    drudeImag = (wp^2/(w*(w^2 + (hbar*gamma)^2)))* (-1*hbar*gamma);


    %Calculate Excited State Dielectric Function
    e1 = e3 - complex(drudeReal, drudeImag);
%   e3 = 1 + 19.5454i
%   e1 = real(e1)
%   e3 = 11.102
%   e1 = -21.22 + 23.22i
%   k1 = sqrt(b^2 - k0^2 * e1);
%   k2 = sqrt(b^2 - k0^2 * e2);
%   k3 = sqrt(b^2 - k0^2 * e3);
%   expFactor = exp(-2*t*k1);
%   first = (k1/e1 + k2/e2)./(k1/e1 - k2/e2);
%   second = (k1/e1 + k3/e3)./(k1/e1 - k3/e3);
```

```
    %Solve thin film plasmonic dispersion equation for Beta
    fun = @(b) exp(-2*t*sqrt(b^2 - k0^2 * e1)) -
    ((sqrt(b^2 - k0^2 * e1)/e1
    + sqrt(b^2 - k0^2 * e2)/e2)./(sqrt(b^2 - k0^2 * e1)/e1
    - sqrt(b^2 - k0^2 * e2)/e2))*((sqrt(b^2 - k0^2 * e1)/e1
    + sqrt(b^2 - k0^2 * e3)/e3)./(sqrt(b^2 - k0^2 * e1)/e1
    - sqrt(b^2 - k0^2 * e3)/e3));

    options = optimoptions('fsolve', 'Display', 'iter-detailed',
    'Algorithm', 'trust-region-dogleg', 'FunctionTolerance',
    1e-10, 'StepTolerance',
    1e-10, 'OptimalityTolerance', 1e-10, 'FiniteDifferenceType',
    'central', 'MaxFunctionEvaluations', 1000);

    b_sol = fsolve(fun, complex(0.05,0.05), options);
    %b_sol = vpasolve(fun(sym('b')), -0.1);
    b_solArr = [b_solArr, b_sol];
end

2*3.14/real(b_sol)

%Plot contour plot
surfFun = @(br,bi) exp(-2.*t.*sqrt(complex(br,bi).^2 - k0^2 .* e1))
- ((sqrt(complex(br,bi).^2 - k0^2 .* e1)/e1
+ sqrt(complex(br,bi).^2 - k0^2 .* e2)/e2)./(sqrt(complex(br,bi).^2
- k0^2 * e1)/e1 - sqrt(complex(br,bi).^2
```

```
- k0^2 .* e2)/e2)).*((sqrt(complex(br,bi).^2 - k0^2 .* e1)/e1
+ sqrt(complex(br,bi).^2 - k0^2 .* e3)/e3)./(sqrt(complex(br,bi).^2
- k0^2 .* e1)/e1 - sqrt(complex(br,bi).^2 - k0^2 .* e3)/e3));

[x,y] = meshgrid(-0.2:0.005:0.2, -0.2:0.005:0.2);
z = surfFun(x,y);
surf(x,y,abs(z));
surfFun(real(b_sol), imag(b_sol));
```

APPENDIX F

Solid on Solid Model Code

This is is the code that was used in the discrete Monte Carlo simulation in chapter 5. Discussion of how this code functions can be found in chapter 5.3.

```
import numpy as np
import matplotlib.pyplot as plt
from scipy.optimize import curve_fit


'''
Function that determines whether an atom is removed
or not based on a random number generator.
The probability is calculated using e^-Ea/kbT where:
Ea is the activation energy
T is the temperature
kb is the Boltzman constant.
'''
def removalDeterm(brokenBonds):
    #Generate a random number from 1 to 100
randomNumber = np.random.randint(0,100)+1
```

```
if (brokenBonds == 4 and randomNumber <= 20):
return 1
elif (brokenBonds == 3 and randomNumber <= 15):
return 1
elif (brokenBonds == 2 and randomNumber <= 10):
return 1
elif (brokenBonds == 1 and randomNumber <= 5):
return 1
else:
return 0


def linear(x,m,b):
    return m*x + b


'''
Initialize the surface to create a simulation area
given by simCellDim x simCellDim.
Set 0 as the value for the original surface.
Negative numbers are below and positive numbers are above
'''
simCellDim = 100
simCell = np.full((simCellDim,simCellDim), 0)



#Parameters for simulation
atomFlux = 0.001 #atoms/nm2/shot, flux
latticeConst = 0.565 #in nm, lattice constant
```

```
cellWidth = 0.4  #in nm, distance between surface atoms
cellHeight = latticeConst/4 #Half a ML
numShots = 1000



#simCell[5,5] = -100

'''
Calculate total number of atoms arriving at the surface
'''
atomFluxTot = int(atomFlux*(cellWidth*simCellDim)**2)
print(atomFluxTot)

#Initialize matrix that determines whether atom is removed or not
removed = np.full((simCellDim, simCellDim), 0)

#Initialize matrix to track average height change after every shot
depth = np.zeros(numShots)

#Initialize figure for making movie
plt.figure("movie")

levels = np.linspace(-13, 1, 10) #Levels for contour plot
frame = 1 #Initialize Current Frame Counter

#Run simulation
```

```
#First for loop: Repeat calculation per number of irradiation
for k in range(numShots):
    avg = 0 #Initialize and Reset Average Current Height

    #Iterate over every matrix element and remove atoms
    for i in range(1,len(simCell)-1):
        for j in range(1,len(simCell)-1):
            brokenBonds = 0
            if (simCell[i,j] > simCell[i,j+1]):
                brokenBonds = brokenBonds + 1
            if (simCell[i,j] > simCell[i,j-1]):
                brokenBonds = brokenBonds + 1
            if (simCell[i,j] > simCell[i+1,j]):
                brokenBonds = brokenBonds + 1
            if (simCell[i,j] > simCell[i-1,j]):
                brokenBonds = brokenBonds + 1
            randomNum = np.random.randint(0, 5)

            #Sum the height of all the cells
            #Note, avg is a misnaming of the variable
            #The actual average is calculated later
            avg = avg + simCell[i,j]

            #Determine whether atom at [i,j] was removed
            removed[i,j] = removalDeterm(brokenBonds)

    #Remove atoms
```

```
    simCell = simCell-removed
    removed = np.full((simCellDim, simCellDim), 0)

    #Introduce vacancies and interstitials
    for i in range(atomFluxTot):
        randNum1 = np.random.randint(1,simCellDim-1)
        randNum2 = np.random.randint(1,simCellDim-1)
        randNum3 = np.random.randint(1,simCellDim-1)
        randNum4 = np.random.randint(1,simCellDim-1)

        #interstitial surfacing
        simCell[randNum1, randNum2] = simCell[randNum1, randNum2] + 1

        #vacancy surfacing
        simCell[randNum3, randNum4] = simCell[randNum3, randNum4] - 1
    #Save height after every shot to turn into movie
    plt.contourf(simCell*cellHeight, levels=levels)
    plt.savefig("./{}.png".format(frame))
    frame=frame+1
    plt.cla()

    #Calculate average height after every irradiation
    depth[k] = cellHeight*avg/(len(simCell)*len(simCell))

#Fit the change in depth per irradiation linearly.
x = np.linspace(0,numShots, numShots)
popt, pcov = curve_fit(linear, x, depth, maxfev=50000)
```

```
print(popt)


#Plot the results
plt.figure(0)
plt.title("Average Depth of Crater vs Number of Exposures")
plt.xlabel("Number of Exposures")
plt.ylabel("Average Depth")
plt.ylim(-10,1)
plt.plot(x,depth)


fig, ax = plt.subplots()
plot = ax.pcolormesh(simCell*cellHeight, vmin=0, vmax=-10)
cbar = fig.colorbar(plot)


plt.show()
```

BIBLIOGRAPHY

BIBLIOGRAPHY

[1] K. Sokolowski-Tinten and D. von der Linde. Generation of dense electron-hole plasmas in silicon. *Phys. Rev. B*, 61(4):2643–2650, January 2000.

[2] B. Rethfeld, A. Kaiser, M. Vicanek, and G. Simon. Ultrafast dynamics of nonequilibrium electrons in metals under femtosecond laser irradiation. *Phys. Rev. B*, 65(21):214303, May 2002.

[3] E. N. Glezer, Y. Siegal, L. Huang, and E. Mazur. Laser-induced band-gap collapse in GaAs. *Phys. Rev. B*, 51(11):6959–6970, March 1995.

[4] J. K. Chen, D. Y. Tzou, and J. E. Beraun. A semiclassical two-temperature model for ultrafast laser heating. *International Journal of Heat and Mass Transfer*, 49(1):307–316, January 2006.

[5] Michael J. Abere, Ben Torralva, and Steven M. Yalisove. Periodic surface structure bifurcation induced by ultrafast laser generated point defect diffusion in GaAs. *Appl. Phys. Lett.*, 108(15):153110, April 2016.

[6] M. J. Abere, C. Chen, D. R. Rittman, M. Kang, R. S. Goldman, J. D. Phillips, B. Torralva, and S. M. Yalisove. Nanodot formation induced by femtosecond laser irradiation. *Appl. Phys. Lett.*, 105(16):163103, October 2014.

[7] Rico S. Cahyadi, Ben Torralva, and Steven M. Yalisove. High spatial frequency periodic structures formation on silicon using near UV femtosecond laser irradiation. *Appl. Phys. Lett.*, 112(3):032105, January 2018.

[8] Michael J. Abere, Steven M. Yalisove, and Ben Torralva. Alignment of morphology during high spatial frequency periodic structure formation in GaAs. *Journal of Applied Physics*, 126(14):143102, October 2019.

[9] J. Bonse, S. Höhm, S. V. Kirner, A. Rosenfeld, and J. Krüger. Laser-Induced Periodic Surface Structures— A Scientific Evergreen. *IEEE Journal of Selected Topics in Quantum Electronics*, 23(3), May 2017.

[10] D V Lang. Recombination-enhanced reactions in semiconductors. *Annu. Rev. Mater. Sci.*, 12(1):377–398, August 1982.

[11] B. Torralva. To be published.

[12] T. E. Orlowski and D. A. Mantell. Ultraviolet laser-induced oxidation of silicon: The effect of oxygen photodissociation upon oxide growth kinetics. *Journal of Applied Physics*, 64(9):4410–4414, November 1988.

[13] S. A. Schafer and S. A. Lyon. Wavelength dependence of laser-enhanced oxidation of silicon. *Journal of Vacuum Science and Technology*, 21(2):422–425, July 1982.

[14] L. V. Keldysh. Ionization in the field of a strong electromagnetic wave. *Soviet Physics JETP*, 20(5), 1964.

[15] P. C. Becker, H. L. Fragnito, C. H. Brito Cruz, R. L. Fork, J. E. Cunningham, J. E. Henry, and C. V. Shank. Femtosecond Photon Echoes from Band-to-Band Transitions in GaAs. *Phys. Rev. Lett.*, 61(14):1647–1649, October 1988.

[16] C. K. Sun, F. Vallée, L. H. Acioli, E. P. Ippen, and J. G. Fujimoto. Femtosecond-tunable measurement of electron thermalization in gold. *Phys. Rev. B*, 50(20):15337–15348, November 1994.

[17] S. K. Sundaram and E. Mazur. Inducing and probing non-thermal transitions in semiconductors using femtosecond laser pulses. *Nature Materials*, 1(4):217–224, December 2002.

[18] C. V. Shank, R. Yen, and C. Hirlimann. Femtosecond-Time-Resolved Surface Structural Dynamics of Optically Excited Silicon. *Phys. Rev. Lett.*, 51(10):900–902, September 1983.

[19] H. W. K. Tom, G. D. Aumiller, and C. H. Brito-Cruz. Time-resolved study of laser-induced disorder of Si surfaces. *Phys. Rev. Lett.*, 60(14):1438–1441, April 1988.

[20] T. Schröder, W. Rudolph, S. V. Govorkov, and I. L. Shumay. Femtosecond laser-induced melting of GaAs probed by optical second-harmonic generation. *Appl. Phys. A*, 51(1):49–51, July 1990.

[21] P. Saeta, J.-K. Wang, Y. Siegal, N. Bloembergen, and E. Mazur. Ultrafast electronic disordering during femtosecond laser melting of GaAs. *Phys. Rev. Lett.*, 67(8):1023–1026, August 1991.

[22] K. Sokolowski-Tinten, H. Schulz, J. Bialkowski, and D. von der Linde. Two distinct transitions in ultrafast solid-liquid phase transformations of GaAs. *Appl. Phys. A*, 53(3):227–234, September 1991.

[23] A. M. Lindenberg. Atomic-Scale Visualization of Inertial Dynamics. *Science*, 308(5720):392–395, April 2005.

[24] D. M. Fritz, D. A. Reis, B. Adams, R. A. Akre, J. Arthur, C. Blome, P. H. Bucksbaum, A. L. Cavalieri, S. Engemann, S. Fahy, R. W. Falcone, P. H. Fuoss,

K. J. Gaffney, M. J. George, J. Hajdu, M. P. Hertlein, P. B. Hillyard, M. Horn-von Hoegen, M. Kammler, J. Kaspar, R. Kienberger, P. Krejcik, S. H. Lee, A. M. Lindenberg, B. McFarland, D. Meyer, T. Montagne, É. D. Murray, A. J. Nelson, M. Nicoul, R. Pahl, J. Rudati, H. Schlarb, D. P. Siddons, K. Sokolowski-Tinten, Th. Tschentscher, D. von der Linde, and J. B. Hastings. Ultrafast bond softening in bismuth: Mapping a solid's interatomic potential with x-rays. *Science*, 315(5812):633–636, 2007.

[25] Y. Siegal, E. N. Glezer, and E. Mazur. Dielectric constant of GaAs during a subpicosecond laser-induced phase transition. *Phys. Rev. B*, 49(23):16403–16406, June 1994.

[26] Li Huang, J. Paul Callan, Eli N. Glezer, and Eric Mazur. GaAs under Intense Ultrafast Excitation: Response of the Dielectric Function. *Phys. Rev. Lett.*, 80(1):185–188, January 1998.

[27] E. N. Glezer, Y. Siegal, L. Huang, and E. Mazur. Behavior of x (2) during a laser-induced phase transition in GaAs. *Phys. Rev. B*, 51(15):9589–9596, April 1995.

[28] K. Sokolowski-Tinten, J. Bialkowski, and D. von der Linde. Ultrafast laser-induced order-disorder transitions in semiconductors. *Phys. Rev. B*, 51(20):14186–14198, May 1995.

[29] M. E. Povarnitsyn, T. E. Itina, M. Sentis, K. V. Khishchenko, and P. R. Levashov. Material decomposition mechanisms in femtosecond laser interactions with metals. *Phys. Rev. B*, 75(23):235414, June 2007.

[30] Leonid V. Zhigilei, Zhibin Lin, and Dmitriy S. Ivanov. Atomistic Modeling of Short Pulse Laser Ablation of Metals: Connections between Melting, Spallation, and Phase Explosion. *J. Phys. Chem. C*, 113(27):11892–11906, July 2009.

[31] Leonid V. Zhigilei, Dmitriy S. Ivanov, Elodie Leveugle, Babak Sadigh, and Eduardo M. Bringa. Computer modeling of laser melting and spallation of metal targets. In *High-Power Laser Ablation V*, volume 5448, pages 505–519. International Society for Optics and Photonics, September 2004.

[32] D.A. Reis, K.J. Gaffney, G.H. Gilmer, and Ben Torralva. Ultrafast Dynamics of Laser-Excited Solids. *EPJ Web of Conferences*, 31:601–606, 2006.

[33] D. von der Linde and K. Sokolowski-Tinten. The physical mechanisms of short-pulse laser ablation. *Applied Surface Science*, 154-155:1–10, February 2000.

[34] Mikel Sanz, Esther Rebollar, Rashid A. Ganeev, and Marta Castillejo. Nanosecond laser-induced periodic surface structures on wide band-gap semiconductors. *Applied Surface Science*, 278:325–329, August 2013.

[35] Jörn Bonse, Arkadi Rosenfeld, and Jörg Krüger. On the role of surface plasmon polaritons in the formation of laser-induced periodic surface structures upon irradiation of silicon by femtosecond-laser pulses. *Journal of Applied Physics*, 106(10):104910, November 2009.

[36] Arkadi Rosenfeld, Marcus Rohloff, Sandra Höhm, Jörg Krüger, and Jörn Bonse. Formation of laser-induced periodic surface structures on fused silica upon multiple parallel polarized double-femtosecond-laser-pulse irradiation sequences. *Applied Surface Science*, 258(23):9233–9236, September 2012.

[37] Jürgen Reif, Florenta Costache, Matthias Henyk, and Stanislav V. Pandelov. Ripples revisited: non-classical morphology at the bottom of femtosecond laser ablation craters in transparent dielectrics. *Applied Surface Science*, 197-198:891–895, September 2002.

[38] Jeff F. Young, J. S. Preston, H. M. van Driel, and J. E. Sipe. Laser-induced periodic surface structure. II. Experiments on Ge, Si, Al, and brass. *Phys. Rev. B*, 27(2):1155–1172, January 1983.

[39] R. J. Nemanich, D. K. Biegelsen, and W. G. Hawkins. Aligned, coexisting liquid and solid regions in laser-annealed Si. *Phys. Rev. B*, 27(12):7817–7819, June 1983.

[40] S. E. Clark and D. C. Emmony. Ultraviolet-laser-induced periodic surface structures. *Phys. Rev. B*, 40(4):2031–2041, August 1989.

[41] D. Dufft, A. Rosenfeld, S. K. Das, R. Grunwald, and J. Bonse. Femtosecond laser-induced periodic surface structures revisited: A comparative study on ZnO. *Journal of Applied Physics*, 105(3):034908, February 2009.

[42] J. Bonse, S. Baudach, J. Krüger, W. Kautek, and M. Lenzner. Femtosecond laser ablation of silicon–modification thresholds and morphology. *Appl Phys A*, 74(1):19–25, January 2002.

[43] A.Y. Vorobyev and Chunlei Guo. Effects of nanostructure-covered femtosecond laser-induced periodic surface structures on optical absorptance of metals. *Appl. Phys. A*, 86(3):321–324, March 2007.

[44] J. E. Sipe, Jeff F. Young, J. S. Preston, and H. M. van Driel. Laser-induced periodic surface structure. I. Theory. *Phys. Rev. B*, 27(2):1141–1154, January 1983.

[45] Min Huang, Fuli Zhao, Ya Cheng, Ningsheng Xu, and Zhizhan Xu. Origin of Laser-Induced Near-Subwavelength Ripples: Interference between Surface Plasmons and Incident Laser. *ACS Nano*, 3(12):4062–4070, December 2009.

[46] Godai Miyaji and Kenzo Miyazaki. Origin of periodicity in nanostructuring on thin film surfaces ablated with femtosecond laser pulses. *Opt. Express, OE*, 16(20):16265–16271, September 2008.

[47] F. Garrelie, J. P. Colombier, F. Pigeon, S. Tonchev, N. Faure, M. Bounhalli, S. Reynaud, and O. Parriaux. Evidence of surface plasmon resonance in ultrafast laser-induced ripples. *Opt. Express, OE*, 19(10):9035–9043, May 2011.

[48] Klaus Sokolowski-Tinten, Anton Barty, Sebastien Boutet, Uladzimir Shymanovich, Henry Chapman, Mike Bogan, Stefano Marchesini, Stefan Hau-Riege, Nikola Stojanovic, Jörn Bonse, Yudi Rosandi, Herbert M. Urbassek, Ra'anan Tobey, Henri Ehrke, Andrea Cavalleri, Stefan Düsterer, Harald Redlin, Matthias Frank, Sasa Bajt, Joachim Schulz, Marvin Seibert, Janos Hajdu, Rolf Treusch, Christoph Bostedt, M. Hoener, and T. Möller. Short-pulse Laser Induced Transient Structure Formation and Ablation Studied with Time-resolved Coherent XUV-scattering. *AIP Conference Proceedings*, 1278(1):373–379, October 2010.

[49] S. Höhm, A. Rosenfeld, J. Krüger, and J. Bonse. Femtosecond laser-induced periodic surface structures on silica. *Journal of Applied Physics*, 112(1):014901, July 2012.

[50] P. Temple and M. Soileau. Polarization charge model for laser-induced ripple patterns in dielectric materials. *IEEE Journal of Quantum Electronics*, 17(10):2067–2072, October 1981.

[51] M. Soileau. Ripple structures associated with ordered surface defects in dielectrics. *IEEE Journal of Quantum Electronics*, 20(5):464–467, May 1984.

[52] J. E. Sipe, H. M. van Driel, and Jeff F. Young. Surface electrodynamics: radiation fields, surface polaritons, and radiation remnants. *Canadian Journal of Physics*, February 2011.

[53] A. Borowiec and H. K. Haugen. Subwavelength ripple formation on the surfaces of compound semiconductors irradiated with femtosecond laser pulses. *Appl. Phys. Lett.*, 82(25):4462–4464, June 2003.

[54] J. Bonse, J. Krüger, S. Höhm, and A. Rosenfeld. Femtosecond laser-induced periodic surface structures. *Journal of Laser Applications*, 24(4):042006, September 2012.

[55] J. Bonse, M. Munz, and H. Sturm. Structure formation on the surface of indium phosphide irradiated by femtosecond laser pulses. *Journal of Applied Physics*, 97(1):013538, January 2005.

[56] Feng Liang, Réal Vallée, and See Leang Chin. Mechanism of nanograting formation on the surface of fused silica. *Opt. Express*, 20(4):4389, February 2012.

[57] E. M. Hsu, T. H. R. Crawford, C. Maunders, G. A. Botton, and H. K. Haugen. Cross-sectional study of periodic surface structures on gallium phosphide induced by ultrashort laser pulse irradiation. *Appl. Phys. Lett.*, 92(22):221112, June 2008.

[58] Takuro Tomita, Ryota Kumai, Shigeki Matsuo, Shuichi Hashimoto, and Makoto Yamaguchi. Cross-sectional morphological profiles of ripples on Si, SiC, and HOPG. *Appl. Phys. A*, 97(2):271–276, November 2009.

[59] Min Huang, Ya Cheng, Fuli Zhao, and Zhizhan Xu. The significant role of plasmonic effects in femtosecond laser-induced grating fabrication on the nanoscale. *Annalen der Physik*, 525(1-2):74–86, 2013.

[60] V. R. Bhardwaj, P. P. Rajeev, P. B. Corkum, and D. M. Rayner. Strong field ionization inside transparent solids. *J. Phys. B: At. Mol. Opt. Phys.*, 39(13):S397–S407, June 2006.

[61] V. R. Bhardwaj, E. Simova, P. P. Rajeev, C. Hnatovsky, R. S. Taylor, D. M. Rayner, and P. B. Corkum. Optically Produced Arrays of Planar Nanostructures inside Fused Silica. *Phys. Rev. Lett.*, 96(5):057404, February 2006.

[62] R. Taylor, C. Hnatovsky, and E. Simova. Applications of femtosecond laser induced self-organized planar nanocracks inside fused silica glass. *Laser & Photonics Reviews*, 2(1-2):26–46, 2008.

[63] X.C. Wang, G.C. Lim, F.L. Ng, W. Liu, and S.J. Chua. Femtosecond pulsed laser-induced periodic surface structures on GaN/sapphire. *Applied Surface Science*, 252(5):1492–1497, December 2005.

[64] Juergen Reif, Olga Varlamova, Sergej Varlamov, and Michael Bestehorn. The role of asymmetric excitation in self-organized nanostructure formation upon femtosecond laser ablation. *Appl. Phys. A*, 104(3):969–973, September 2011.

[65] J. Bonse, S. Höhm, A. Rosenfeld, and J. Krüger. Sub-100-nm laser-induced periodic surface structures upon irradiation of titanium by Ti:sapphire femtosecond laser pulses in air. *Appl. Phys. A*, 110(3):547–551, March 2013.

[66] Xian-Feng Li, Cheng-Yun Zhang, Hui Li, Qiao-Feng Dai, Sheng Lan, and Shao-Long Tie. Formation of 100-nm periodic structures on a titanium surface by exploiting the oxidation and third harmonic generation induced by femtosecond laser pulses. *Opt. Express, OE*, 22(23):28086–28099, November 2014.

[67] Xxx Sedao, Maxim V. Shugaev, Chengping Wu, Thierry Douillard, Claude Esnouf, Claire Maurice, Stéphanie Reynaud, Florent Pigeon, Florence Garrelie, Leonid V. Zhigilei, and Jean-Philippe Colombier. Growth Twinning and Generation of High-Frequency Surface Nanostructures in Ultrafast Laser-Induced Transient Melting and Resolidification, July 2016.

[68] NuoFu Chen, Yutian Wang, Hongjia He, and Lanying Lin. Effects of point defects on lattice parameters of semiconductors. *Phys. Rev. B*, 54(12):8516–8521, September 1996.

[69] Anatoly V. Zayats, Igor I. Smolyaninov, and Alexei A. Maradudin. Nano-optics of surface plasmon polaritons. *Physics Reports*, 408(3-4):131–314, March 2005.

[70] William L. Barnes, Alain Dereux, and Thomas W. Ebbesen. Surface plasmon subwavelength optics. *Nature*, 424(6950):824–830, August 2003.

[71] W. L. Barnes, T. W. Preist, S. C. Kitson, and J. R. Sambles. Physical origin of photonic energy gaps in the propagation of surface plasmons on gratings. *Phys. Rev. B*, 54(9):6227–6244, September 1996.

[72] R. Hill and J.W. Hutchinson. Bifurcation phenomena in the plane tension test. *Journal of the Mechanics and Physics of Solids*, 23(4-5):239–264, August 1975.

[73] D.J. Srolovitz. On the stability of surfaces of stressed solids. *Acta Metallurgica*, 37(2):621–625, February 1989.

[74] Heinz Raether. *Surface Plasmons on Smooth and Rough Surfaces and on Gratings*. Springer Tracts in Modern Physics. Springer-Verlag, Berlin Heidelberg, 1988.

[75] L. Salomon, G. Bassou, H. Aourag, J. P. Dufour, F. de Fornel, F. Carcenac, and A. V. Zayats. Local excitation of surface plasmon polaritons at discontinuities of a metal film: Theoretical analysis and optical near-field measurements. *Phys. Rev. B*, 65(12):125409, March 2002.

[76] S. C. Kitson, W. L. Barnes, G. W. Bradberry, and J. R. Sambles. Surface profile dependence of surface plasmon band gaps on metallic gratings. *Journal of Applied Physics*, 79(9):7383–7385, May 1996.

[77] T. J.-Y. Derrien, R. Koter, J. Krüger, S. Höhm, A. Rosenfeld, and J. Bonse. Plasmonic formation mechanism of periodic 100-nm-structures upon femtosecond laser irradiation of silicon in water. *J. Appl. Phys.*, 116(7):074902, 2014.

[78] Stefan A. Maier. *Plasmonics: fundamentals and applications*. Springer, New York, 2007.

[79] A. J. SpringThorpe, S. J. Ingrey, B. Emmerstorfer, P. Mandeville, and W. T. Moore. Measurement of GaAs surface oxide desorption temperatures. *Appl. Phys. Lett.*, 50(2):77–79, January 1987.

[80] T.-C. Shen, C. Wang, G. C. Abeln, J. R. Tucker, J. W. Lyding, Ph Avouris, and R. E. Walkup. Atomic-Scale Desorption Through Electronic and Vibrational Excitation Mechanisms. *Science*, 268(5217):1590–1592, June 1995.

[81] Peter Saalfrank, Gisela Boendgen, Cécile Corriol, and Tohru Nakajima. Direct and indirect DIET and DIMET from semiconductor and metal surfaces: What can we learn from 'toy models'? *Faraday Discuss.*, 117(0):65–83, January 2000.

[82] Dietrich Menzel and Robert Gomer. Desorption from Metal Surfaces by Low-Energy Electrons. *J. Chem. Phys.*, 41(11):3311–3328, December 1964.

[83] P A Redhead. Interaction of slow electrons with chemisorbed oxygen. *Canadian Journal of Physics*, 42(5):886–905, 1964.

[84] J. A. Misewich, T. F. Heinz, and D. M. Newns. Desorption induced by multiple electronic transitions. *Phys. Rev. Lett.*, 68(25):3737–3740, June 1992.

[85] Noriaki Itoh and Takeyoshi Nakayama. Mechanism of neutral particle emission from electron-hole plasma near solid surface. *Physics Letters A*, 92(9):471–475, December 1982.

[86] Hitoshi Sumi. Theory on laser sputtering by high-density valence-electron excitation of semiconductor surfaces. *Surface Science*, 248(3):382–410, June 1991.

[87] J. Kanasaki, K. Iwata, and K. Tanimura. Translational Energy Distribution of Si Atoms Desorbed by Laser-Induced Electronic Bond Breaking of Adatoms on Si (111) - (7 × 7). *Phys. Rev. Lett.*, 82(3):644–647, January 1999.

[88] P. W. Anderson. Model for the Electronic Structure of Amorphous Semiconductors. *Phys. Rev. Lett.*, 34(15):953–955, April 1975.

[89] B. Y. Han, Koji Nakayama, and J. H. Weaver. Electron- and photon-stimulated modification of GaAs(110), Si(100), and Si(111). *Phys. Rev. B*, 60(19):13846–13853, November 1999.

[90] Noriaki Itoh, Akiko Okano, Ken Hattori, Jyun'ichi Kanasaki, and Yasuo Nakai. Vacancy-initiated laser sputtering from semiconductor surfaces. *Nuclear Instruments and Methods in Physics Research Section B: Beam Interactions with Materials and Atoms*, 82(2):310–316, July 1993.

[91] Jun' ichi Kanasaki, Akiko Okano, Ken' ichi Ishikawa, Yasuo Nakai, and Noriaki Itoh. Dynamical interaction of surface electron-hole pairs with surface defects: Surface spectroscopy monitored by particle emissions. *Phys. Rev. Lett.*, 70(16):2495–2498, April 1993.

[92] Ken Hattori, Akiko Okano, Yasuo Nakai, and Noriaki Itoh. Laser-induced electronic processes on gap (110) surfaces: Particle emission and ablation initiated by defects. *Phys. Rev. B*, 45:8424–8436, Apr 1992.

[93] B. E. Deal and A. S. Grove. General Relationship for the Thermal Oxidation of Silicon. *Journal of Applied Physics*, 36(12):3770–3778, December 1965.

[94] William A. Tiller. On the Kinetics of the Thermal Oxidation of Silicon: II . Some Theoretical Evaluations. *J. Electrochem. Soc.*, 127(3):625–632, March 1980.

[95] William A. Tiller. On the Kinetics of the Thermal Oxidation of Silicon: I . A Theoretical Perspective. *J. Electrochem. Soc.*, 127(3):619–624, March 1980.

[96] S. A. Schafer and S. A. Lyon. Optically enhanced oxidation of semiconductors. *Journal of Vacuum Science and Technology*, 19(3):494–497, September 1981.

[97] A. Lora-Tamayo, E. Dominguez, E. Lora-Tamayo, and J. Llabres. A new model of the thermal growth of a silicon dioxide layer. *Appl. Phys.*, 17(1):79–84, September 1978.

[98] A. Redondo, W. A. Goddard, C. A. Swarts, and T. C. McGill. Oxidation of silicon surfaces. *Journal of Vacuum Science and Technology*, 19(3):498–501, September 1981.

[99] M.T Schmidt, Z Wu, C.F Yu, and R.M Osgood. Atomic movement during the oxidation of GaAs. *Surface Science*, 226(1-2):199–205, February 1990.

[100] W. G. Petro, I. Hino, S. Eglash, I. Lindau, C. Y. Su, and W. E. Spicer. Effect of low-intensity laser radiation during oxidation of the GaAs(110) surface. *Journal of Vacuum Science and Technology*, 21(2):405–408, July 1982.

[101] Z. Lu, M. T. Schmidt, D. V. Podlesnik, C. F. Yu, and R. M. Osgood. Ultraviolet-light-induced oxide formation on GaAs surfaces. *The Journal of Chemical Physics*, 93(11):7951–7961, December 1990.

[102] D. Shaw. *Atomic Diffusion in Semiconductors*. Springer Science & Business Media, December 2012.

[103] Albert Einstein. Zur theorie der brownschen bewegung. *Annalen der Physik*, 324(2):371–381, 1906.

[104] Jean Perrin. *Brownian Movement and Molecular Reality*. Courier Corporation, 1909.

[105] Howard C. Berg. *Random Walks in Biology*. Princeton University Press, November 2018.

[106] J. F. Wager. Energetics of self-diffusion in GaAs. *Journal of Applied Physics*, 69(5):3022–3031, March 1991.

[107] B. Goldstein. Diffusion in Compound Semiconductors. *Phys. Rev.*, 121(5):1305–1311, March 1961.

[108] H. R. Potts and G. L. Pearson. Annealing and Arsenic Overpressure Experiments on Defects in Gallium Arsenide. *Journal of Applied Physics*, 37(5):2098–2103, April 1966.

[109] S. Y. Chiang and G. L. Pearson. Properties of vacancy defects in GaAs single crystals. *Journal of Applied Physics*, 46(7):2986–2991, July 1975.

[110] T. Y. Tan, S. Yu, and U. Gösele. Determination of vacancy and self-interstitial contributions to gallium self-diffusion in GaAs. *Journal of Applied Physics*, 70(9):4823–4826, November 1991.

[111] Edmund G. Seebauer, Michael Y. L. Jung, Charlotte T. M. Kwok, Ramakrishnan Vaidyanathan, and Yevgeniy V. Kondratenko. Measurement of photostimulated self-diffusion in silicon. *Journal of Applied Physics*, 109(10):103708, May 2011.

[112] T. D. Dzhafarov. Photostimulated Diffusion in Semiconductors. *physica status solidi (a)*, 79(1):11–45, 1983.

[113] John D. Weeks, John C. Tully, and L. C. Kimerling. Theory of recombination-enhanced defect reactions in semiconductors. *Phys. Rev. B*, 12(8):3286–3292, October 1975.

[114] G. D. Watkins and J. R. Troxell. Negative-U Properties for Point Defects in Silicon. *Phys. Rev. Lett.*, 44(9):593–596, March 1980.

[115] D Pons and J C Bourgoin. Irradiation-induced defects in GaAs. *J. Phys. C: Solid State Phys.*, 18(20):3839–3871, July 1985.

[116] J. M. Liu. Simple technique for measurements of pulsed Gaussian-beam spot sizes. *Opt. Lett., OL*, 7(5):196–198, May 1982.

[117] Ryan D. Murphy, Ben Torralva, David P. Adams, and Steven M. Yalisove. Polarization dependent formation of femtosecond laser-induced periodic surface structures near stepped features. *Appl. Phys. Lett.*, 104(23):231117, June 2014.

[118] Go Obara, Hisashi Shimizu, Taira Enami, Eric Mazur, Mitsuhiro Terakawa, and Minoru Obara. Growth of high spatial frequency periodic ripple structures on SiC crystal surfaces irradiated with successive femtosecond laser pulses. *Opt. Express*, 21(22):26323, November 2013.

[119] B. Y. Han and J. H. Weaver. Laser interaction with Br-GaAs(110): Etching and atomic desorption. *Phys. Rev. B*, 58(16):10981, October 1998.

[120] B. Y. Han, Koji Nakayama, and J. H. Weaver. Electron- and photon-stimulated modification of GaAs(110), Si(100), and Si(111). *Phys. Rev. B*, 60(19):13846, November 1999.

[121] V. I. Emel'yanov. Self-organization of ordered nano- and microstructures on the semiconductor surface under the action of laser radiation. *Laser Phys.*, 18(18):682, 2008.

[122] J. Kanasaki, N. Mikasa, and K. Tanimura. Laser-induced electronic desorption from InP surfaces studied by femtosecond nonresonant ionization spectroscopy. *Phys. Rev. B*, 64(3):035414, June 2001.

[123] Godai Miyaji, Kenzo Miyazaki, Kaifeng Zhang, Takakazu Yoshifuji, and Junya Fujita. Mechanism of femtosecond-laser-induced periodic nanostructure formation on crystalline silicon surface immersed in water. *Opt. Express*, 20(14):14848, Jul 2012.

[124] M. Rebien, W. Henrion, M. Hong, J. P. Mannaerts, and M. Fleischer. Optical properties of gallium oxide thin films. *Applied Physics Letters*, 81(2):250–252, 2002.

[125] Chao Lian, S. B. Zhang, and Sheng Meng. Ab initio evidence for nonthermal characteristics in ultrafast laser melting. *Phys. Rev. B*, 94(18):184310, November 2016.

[126] Michael J Abere. *From Point Defects to Ripples: Ultrafast Laser Induced High Spatial Frequency Laser Induced Periodic Surface Structures*. PhD thesis, University of Michigan, 2015.

[127] Sergio Bietti, Claudio Somaschini, Luca Esposito, Alexey Fedorov, and Stefano Sanguinetti. Gallium surface diffusion on GaAs (001) surfaces measured by crystallization dynamics of Ga droplets. *Journal of Applied Physics*, 116(11):114311, September 2014.

[128] U M Gosele. Fast Diffusion in Semiconductors. *Ann. Rev. Mater. Sci.*, 18:257, 1988.

[129] H. D. Palfrey, M. Brown, and A. F. W. Willoughby. Self-Diffusion in gallium arsenide. *JEM*, 12(5):863–877, September 1983.

[130] Martin Schultze, Krupa Ramasesha, C. D. Pemmaraju, S. A. Sato, D. Whitmore, A. Gandman, James S. Prell, L. J. Borja, D. Prendergast, K. Yabana, Daniel M. Neumark, and Stephen R. Leone. Attosecond band-gap dynamics in silicon. *Science*, 346(6215):1348–1352, December 2014.

[131] V. I. Emel'yanov and P. K. Kashkarov. Laser-induced defect formation in semiconductors. *Appl. Phys. A*, 55(2):161–166, August 1992.

[132] Hanh Tran Thi Thu and Vo Van Hoang. Molecular dynamics simulation of diffusion in liquid gallium arsenide. *Computational Materials Science*, 49(4):S221–S224, October 2010.

[133] W. K. Warburton and D. Turnbull. 4 - Fast Diffusion in Metals. In A. S. Nowick and J. J. Burton, editors, *Diffusion in Solids*, pages 171–229. Academic Press, January 1975.

[134] J.R. Arthur. Surface stoichiometry and structure of GaAs. *Surf. Sci.*, 43(2):449, June 1974.

[135] Jun'ichi Kanasaki and Katsumi Tanimura. Laser-induced electronic desorption of Si atoms from Si (111) - (7 $\times$ 7). *Phys. Rev. B*, 66(12):125320, September 2002.

[136] Matthew Pelliccione and T.-M. Lu. *Evolution of thin film morphology: modeling and simulations*. Number v. 108 in Springer series in materials science. Springer, New York ; London, 2008.

[137] D. M. Kazantsev, I. O. Akhundov, N. S. Rudaya, A. S. Kozhukhov, V. L. Alperovich, and A. V. Latyshev. Thermal roughening of GaAs surface by unwinding dislocation-induced spiral atomic steps during sublimation. *Applied Surface Science*, 529:147090, November 2020.

[138] R. H. Doremus. Oxidation of silicon by water and oxygen and diffusion in fused silica, May 2002.

[139] Che-Hsin Lin. Oxidation (of Silicon). In Dongqing Li, editor, *Encyclopedia of Microfluidics and Nanofluidics*, pages 1–11. Springer US, Boston, MA, 2013.

[140] E. M. Young. Electron-active silicon oxidation. *Appl. Phys. A*, 47(3):259–269, November 1988.

[141] E. M. Young and William A. Tiller. Electron population factor in light enhanced oxidation of silicon. *Appl. Phys. Lett.*, 50(1):46–48, January 1987.

[142] D. Mathiot, J. P. Schunck, M. Perego, M. Fanciulli, P. Normand, C. Tsamis, and D. Tsoukalas. Silicon self-diffusivity measurement in thermal SiO2 by 30Si/28Si isotopic exchange. *Journal of Applied Physics*, 94(3):2136–2138, August 2003.

[143] H T Liu' and Z Wu. Energy-resolved study of laser-stimulated Si+ desorption from Si(l0 0). *Nuclear Instruments and Methods in Physics Research Section B: Beam Interactions with Materials and Atoms*, page 5, 1995.

[144] Shigeto Fukatsu, Kohei M. Itoh, Masashi Uematsu, Hiroyuki Kageshima, Yasuo Takahashi, and Kenji Shiraishi. Effect of Si/SiO2 Interface on Silicon and Boron Diffusion in Thermally Grown SiO2. *Jpn. J. Appl. Phys.*, 43(11S):7837, November 2004.

[145] N. F. Mott, S. Rigo, F. Rochet, and A. M. Stoneham. Oxidation of silicon. *Philosophical Magazine B*, 60(2):189–212, August 1989.

[146] K.R. Williams, K. Gupta, and M. Wasilik. Etch rates for micromachining processing-Part II. *Journal of Microelectromechanical Systems*, 12(6):761–778, December 2003.

[147] P. M. Ushasree and B. Bora. Silicon solar cells. In *Solar Energy Capture Materials*, pages 1–55. The Royal Society of Chemistry, 2019.

[148] A. V. Crewe, D. N. Eggenberger, J. Wall, and L. M. Welter. Electron gun using a field emission source. *Review of Scientific Instruments*, 39(4):576–583, 1968.

[149] M. Aeschlimann, E. Hull, J. Cao, C. A. Schmuttenmaer, L. G. Jahn, Y. Gao, H. E. Elsayed-Ali, D. A. Mantell, and M. R. Scheinfein. A picosecond electron gun for surface analysis. *Review of Scientific Instruments*, 66(2):1000–1009, February 1995.

[150] H. Park, Z. Hao, X. Wang, S. Nie, R. Clinite, and J. Cao. Synchronization of femtosecond laser and electron pulses with subpicosecond precision. *Review of Scientific Instruments*, 76(8):083905, August 2005.

[151] J. H. Neave, B. A. Joyce, P. J. Dobson, and N. Norton. Dynamics of film growth of GaAs by MBE from Rheed observations. *Appl. Phys. A*, 31(1):1–8, May 1983.

[152] Bixue Hou, John A. Nees, Wolfgang Theobald, Gérard A. Mourou, L. M. Chen, Jean-Claude Kieffer, Andrzej Krol, and C. C. Chamberlain. Dependence of hard x-ray yield on laser pulse parameters in the wavelength-cubed regime. *Appl. Phys. Lett.*, 84(13):2259–2261, March 2004.

[153] Matthew D. Seaberg, Bosheng Zhang, Dennis F. Gardner, Elisabeth R. Shanblatt, Margaret M. Murnane, Henry C. Kapteyn, and Daniel E. Adams. Tabletop nanometer extreme ultraviolet imaging in an extended reflection mode using coherent Fresnel ptychography. *Optica, OPTICA*, 1(1):39–44, July 2014.

[154] Dhonny Bacuyag, Mary Clare Sison Escaño, Melanie David, and Masahiko Tani. First-principles study of structural, electronic, and optical properties of surface defects in gaas(001) - b2(2x4). *AIP Advances*, 8(6):065012, 2018.